Third Order Time and Frequency Domain and Mutual Information Analyses for Neuronal Spike Trains

Yaoru YANG

Ph.D.

University of York

Electronic Engineering

September 2018

Abstract

Research on the brain has received considerable attention over the last two decades. Non-randomness of the information flow is widely reported in the study of the brain. Statistical Signal Processing methods have been applied to analyse the dependencies between neuronal recordings. From one side, this makes a great contribution towards further understanding of the brain. On the other side, due the the progress of experimental technology, analysing experimental data becomes a more and more difficult task and hence requires advanced approaches to be developed. Evidence of higher order interactions and nonlinear interactions has been reported in recent experimental findings. This project develops two approaches for statistical signal processing to analyse Multielectrode Array (MEA) data. The first one is a Unified framework of Third Order time and frequency domain analysis (UTO) and the second one is a Mutual Information Function (MIF). These two approaches are described and applied to single unit spike trains to interpret the interactions and dependencies between the spiking neurons. The presence of dependencies are successfully estimated by each approach. In simulations where a modelled neuronal network with 100 neurons, UTO is applied to investigate third order dependencies according to a centre-surrounded pattern of connectivities in the network. The correct pattern of excitatory and inhibitory connections are detected using UTO. Significant values of cumulant estimates are present when third order interactions are present. MIF analysis is also conducted on the simulations. The proposed method computes the Mutual Information (MI) as a function of time lags, along with a Monte-Carlo based calibration method using 100 trials of Poisson spike trains. Significant departure of MI value from the baseline are shown when the dependence exists. UTO and MIF are applied to an experimental MEA spike train data collected from a study of connectivity in a model of kainic acid (KA) induced epileptiform activity for mesial temporal lobe epilepsy (mTLE) in rat. UTO and MIF both successfully highlight the short latency and long latency dependencies existing in the dataset. Therefore, UTO and MIF provide complementary tools to capture dependencies between spike train signals.

Contents

List of Figures

List of Tables

Acknowledgements

First I am mostly grateful to my supervisor Dr. David Halliday. He is surely the most important person in my Ph.D program. His dedication and patience influence me. His sense of humour encourages me. His wisdom, knowledge, academic intuition and rigorous logic saved me from straying for many times. His generous and full-hearted support is the key of the progress of this project.

I also would like to thank my parents for giving me constant and unconditional support and love. Nobody can love me in the way they do and nobody would make the sacrifice as they have made for me.

I would also give my thanks to Dr. Yuriy Zakharov for his sharing, guidance and great input to my research. He inspired me in many ways. Also, I would like to thank Dr. Luca Citi for his coming all the way from Essex to be my examiner.

Finally, I must thank all my friends and fellow students who have given so much help and with whom I enjoyed a great time during my study.

Declaration

I, Yaoru YANG, hereby declare that except where specific reference is made to the work of others, the contents of this thesis are original and are the result of my own work and research during the my Ph.D project. Some of the material presented has already been published, or is about to be, in the form of conference papers with myself as first author. None of the contents has been submitted in whole or in part for consideration for any other degree or qualification in this, or any other university.

List of Abbreviations

2D Two Dimensions

CI Confidence Interval

CNS Central Nervous System

COV Coefficient Of Variation

EPSP Excitatory Postsynaptic Potential

IPSP Inhibitory Postsynaptic Potential

ISI Interspike Interval

KA Kainic Acid

LFP Local Field Potential

LIF Leaky Integrated-and-Fire

MEA Multielectrode Array

MIF Mutual Information Function

PNS Peripheral Nervous System

PSP Postsynaptic Potential

TLE Temporal Lobe Epilepsy

UTO Unified framework of Third Order time and frequency domain analysis

Chapter 1. Introduction

Contents

1.1 Motivation

Neurons in the nervous system interact with each other every single moment. Whenever we fold our arms, play a violin, run on the treadmill or think of a complicated mathematical problem, the neurons in different parts of our nervous system transfer and process information (see figure 1.1) (Gazzaniga, 2004; Kandel et al., 1995). Hence, knowledge of how information is transferred, processed and stored in the nervous system is essential for understanding the nervous system. Statistical signal processing and computational neuroscience pave a way for quantitatively studying these problems, trying to uncover the principle of the working theory of nervous system and advance our understanding of the brain. Studies can be focused from different viewpoints, or in the context of different biological levels. Since a series of recording techniques has been invented and improved, studying the nervous system through different kinds of electrical or magnetic activities gives higher reliability. A particular scientific area is the detection of interactions and dependencies between neurons, which is also known as functional connectivity detecting or sychronisation (Rubinov and Sporns, 2010). This project is interested in using statistical signal processing methods to studying the functional connectivity, because of several reasons:

1. There are requirements in this scientific area due to the universality of interactions in the nervous system. Neurons communicate and interact with each other no matter

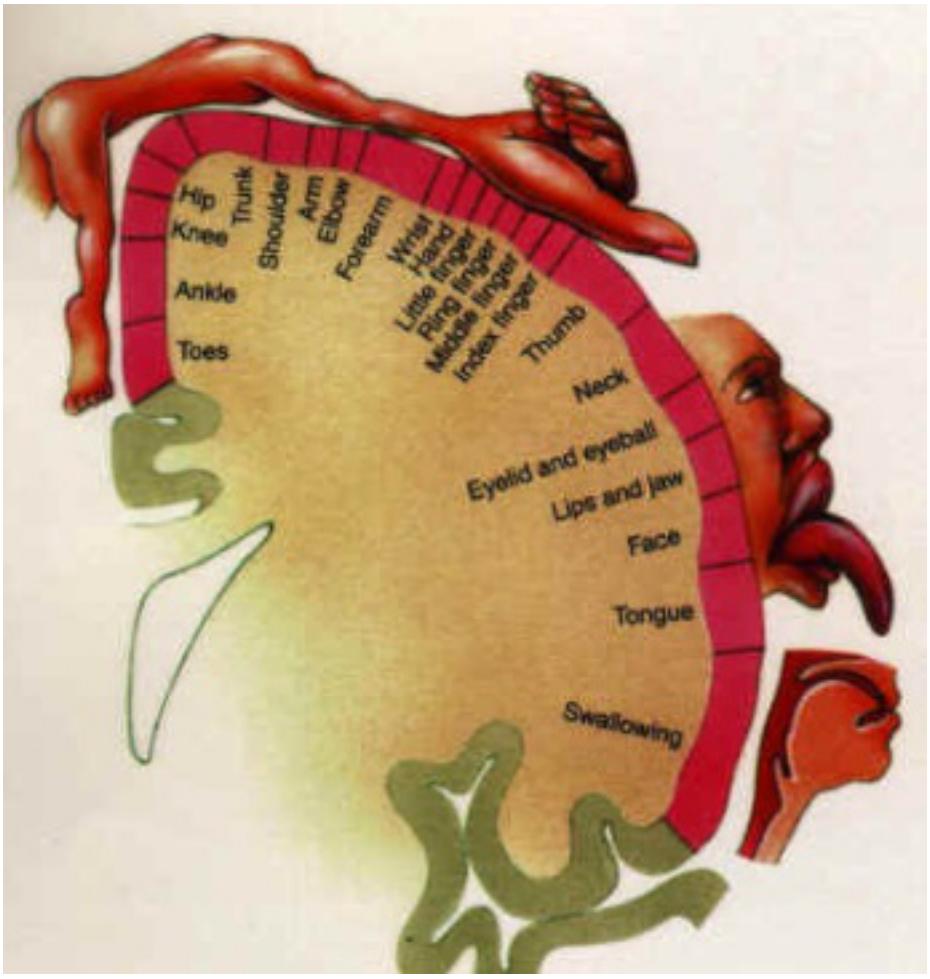

Figure 1.1: This figure illustrate the functions of different parts in motor cortex. This figure indicates that the more complex and more precise the behaviour is, the larger parts of motor cortex are involved (for example, the hand and face). On the other hand, less complex movements, like walking or swallowing, need less area of motor cortex involved. Figure from (Gazzaniga, 2004)

whether we do physical exercise or think about things silently.

2. Although the interaction between neurons involves complicated nonlinear phenomena, many works succeed in reliably detecting interactions between neurons by estimates of linear measures. The classical and widespread techniques are second order, for instance, cross-correlation (Gevins and Schaffer, 1979; Brazier and Casby, 1952; Perkel et al., 1967), coherence (Carter et al., 1973; Brillinger, 1981; Rosenberg et al., 1989) and Granger Causality (Granger, 1969; Geweke, 1982; Sameshima and Baccalá, 1999). Not much work has been done in addressing the detection of nonlinear interactions.

A natural question is what makes the existing methods less applicable to nonlinear problems. The difficulty is primarily because of the nonlinearity and lack of good estimators. The nonlinear problem is familiar to people who carry out research in a wide range of disciplines. In this case, the entire nervous system can be regarded as a dynamic nonlinear system. However, most of the widely applied methods are not capable of revealing information about the nonlinearity. Whenever nonlinear phenomena are present, intuitive thinking is to extend the linear measures. For example, nonlinear Ganger causality has been derived (Freiwald et al., 1999), the correlation coefficients also has its nonlinear version (da Silva et al., 1989; Pijn et al., 1990). However, they are not easily applicable in neuroscience context, the former just suitable for electroencephalogram (often referred as EEG) signals, while the latter depends on selection of statistical model for charactering the dynamic property of the signals (Pereda et al., 2005).

The second issue is lack of good estimators. There are mature techniques such as mutual information (Shannon and Weaver, 1949), which potentially can deal with any nonlinearity. However, reliably estimating the measure from finite size of samples can be difficult. Some well-designed estimators have been developed (Kraskov et al., 2004; Darbellay et al., 1999; Shlens et al., 2007), these solutions solve the problem to some extent, but at the same time, they all have their specific drawbacks. Driven by

these reasons, new techniques which can overcome these drawbacks are studied in this project.

From a computational neuroscience viewpoint, the electrical signals recorded from neurons can be regarded as time series, which is mathematical model depict function value against recording time (Priestley, 1981), or point process, which is a type of random process for which any one realisation consists of a set of isolated points in time (Brillinger, 1975c). Hence, statistical elements and signal processing techniques can be introduced to analyse these neuronal signals. Therefore, functional interaction studies in computational neuroscience can be mathematically modelled using statistical signal processing methods to analyse recorded data, trying to obtain some measurement which can be convincingly inferred in a statistical way to illustrate the interaction between neurons. The methods which are developed in this project should be sensitive to nonlinearity, easily calculated, reliably estimated and firmly tested.

1.2 Hypothesis

The hypothesis of this project is:

Higher order statistics and information theory related methods could provide evidence of dependencies between neurons and should be able to reveal interaction patterns beyond the linear cases.

It should be worthwhile to develop new techniques based on higher order statistics and information theory related methods to reveal the interaction pattern which is difficult to detect using second order analysis. This could potentially be helpful to further our understanding of nonlinear dynamical properties in the nervous system. This could also be a feasible framework for point process data to investigate the associations between them.

One way to achieve a higher order statistical method is to consider a unified framework of time and frequency domain, because from the experience of second order time-frequency domain methods, finding the frequency domian equivalent not only gives a new estimator, but also sometimes can provide a quicker way combining with inverse Fourier transform to calculate estimates in the time domain.

For information theory related methods, a possible way is to develop an approach to reliably estimate the distribution function of point processes from finite size sampled data. The gap between utilisation of information theory related methods and the data type involving in this project is the difficulty to apply density function estimation methods to point processes (spike trains).

1.3 Thesis Structure

This thesis has six chapters. This section will outline the rest of this thesis.

Chapter 2 provides an introduction to background knowledge of the nervous system, human brain and neurons in general, including reviews on some theoretical background concepts and principals related to this project from two viewpoints: biological background perspective and computational neuroscience perspective.

Chapter 3 surveys existing second order statistical signal processing methods in detail. This survey contains descriptions of definitions, algorithms and common applications, including correlation, spectra, coherence, Granger causality. It also provides a review of probability and information theory, including descriptions of concepts, definitions and necessary deriviations.

Chapter 4 presents a Unified framework of Third Order time and frequency domain (UTO) analysis for neural system. Results obtained by applying this framework are presented in this chapter demonstrating the advantages of this unified framework. This

chapter also includes a brief description of the simulated dataset using cortical network model. The UTO analysis is conducted on the simulated dataset by investigating some spike train combinations with gradually increased spatial separation. The results are consistent with centre-surrounded connectivity pattern in the simulated network. The UTO analysis is then applied to the experimental data by investigating the ”CA3 - CA1” triplet combinations. The results highlight that the UTO analysis is capable of capturing the third order interactions.

Chapter 5 proposes a mutual information function (MIF) estimator using kth nearest neighbour statistics. Results obtained by applying this algorithm to datasets are also presented in the same way as chapter 4. The proposed approach is presented along with a description of constructing the baseline indicating independence using a pair of Poisson spike trains. MIF analysis is then conducted on the simulated data discussed in chapter 4. The results imply that the MIF is useful to detect connectivities between neurons. Application of MIF on the experimental data discussed in chapter 4 is conducted by investigating the ”CA3 - CA1” information flow pattern in hippocampus. The results shows that MIF is a useful to evaluate the dependencies between spike trains.

Chapter 6 draws the final conclusions of this thesis and proposes future work. A general summary of the proposed techniques and results is first provided, followed by more detailed summaries chapter by chapter. Future work is discussed at the end of this thesis.

Chapter 2. A brief Review on Neuroscience

Contents

2.1 Introduction

Nervous system provides a wide range of areas to investigate (Shepard, 1988; Gazzaniga, 2000). Different researchers studied range of topics (Ashburner and Friston, 2000; Woolrich et al., 2001; Rubinov and Sporns, 2010; Izhikevich, 2007). In recent

years, increased knowledge about the nervous system and how it works has been accumulated. With all the progress, it was realised that the key issue to improve understanding of the nervous system is to reveal the mechanisms how information is processed, stored and transferred in it. Complex activities can be done only under control of the brain via coordinating different parts of the brain itself and processing different kinds of processes. Taking playing a violin as an example, the brain must integrate regions corresponding to vision, auditory sense and motor control to achieve this task. Visual information on the bow, strings and music score, along with the auditory feedback of the music and movement of fingers, arms and neck have to be handled at the same time to produce a piece of music.

The different parts of the brain consisting of large number of neurons which are specialised in processing particular inputs are known as brain regions (Kandel et al., 2000; Gazzaniga, 2000). Aiming at deepening the understanding of the communication and information processing mechanisms in the nervous system, a systematic review of biological background of anatomical and physiological knowledge is discussed in this chapter.

The elementary and functional cells in the brain are neurons which are significant in information communication procedures (Nicholls et al., 2001). The prototype signals of information communication in the brain is known as action potential, or spike (Dayan and Abbott, 2001). Hence, it is possible to study the information processing between neurons, networks and brain regions by measuring the association between spikes. Modern electrical recording and spike sorting techniques (see section are able to provide signals on which further analyses can be conducted (Karkare et al., 2013; Quiroga et al., 2004).

This chapter discusses background knowledge in three areas. The first part including section 2.2 - 2.6 will provide biological background information, giving a brief introduction to the nervous system, the brain and neurons. Neurons as the basic signalling units, their chemical and electrical properties are discussed in this chapter, fellow by a

detailed discussion of the action potential (spike). The second part is from the viewpoint of Computational neuroscience. Spiking neuron models are presented in detail in section 2.7. The last part (section 2.8) will mention the Multielectrode Array (MEA) recording technique and will briefly describe the spike sorting techniques since spike trains are the signal in which this project is interested.

2.2 Central Nervous System and Brain

The nervous system exists in most multicellular animals but varies in its complexity. It transmits information to and from different parts of body so that both voluntary and involuntary actions of the body are coordinated by the nervous system (Trappenberg, 2010). In vertebrate species, nervous system is subdivided into two major parts: The central nervous system (CNS) and the peripheral nervous system (PNS). The central nervous system is composed of the brain and spinal cord, and it functions to process information, send signals from one cell to others and receive feedbacks. It acts like an integrative and control centre for the whole body (Kandel et al., 1995). The peripheral nervous system acts like communication channels between the central nervous system and the rest of the body (Shepard, 1988).

The central nervous system is divided into several parts, namely spinal cord, medulla, pons, cerebellum, midbrain, diencephalon and cerebral hemispheres. Apart from the spinal cord, these construct the brain. Figure 2.1 shows their approximate position inside the human body. The diencephalon and cerebral hemispheres are worthy of highlighting here because they are involved deeply in information processing. Hence, much attention has been paid to these two parts (Alexander and Crutcher, 1990; Alexander et al., 1986; Freund and Buzsáki, 1996). The diencephalon has two important structures, the thalamus and the hypothalamus, the former processes most of the information arriving at the cerebral cortex from other parts across central nervous system, while the latter regulates autonomic, endocrine and visceral functions. The cerebral hemispheres contain the cerebral cortex, basal ganglia, hippocampus and amygdaloid. The basal ganglia is largely related with motor performance, the hippocampus plays an

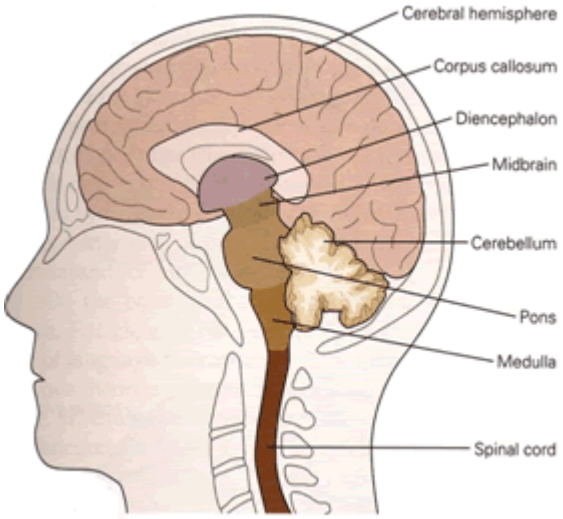

Figure 2.1: The central nervous system consists eight main parts: spinal cord, Medulla, pons, cerebellum, midbrain, diencephalon, Corpus callosum and cerebral hemispheres. Figure from (Kandel et al., 2000)

essential roly in memory storage and the amygdaloid is invloved in emotional states. Overlying both hemispheres is the the heavily wrinkled layer of cerebral cortex subdivided into four lobes: the frontal lobe, parietal lobe, temporal lobe and occipital lobe (Kandel et al., 2000). Information is transferred and processed inside or across these different regions in the brain.

The levels of organisation in nervous system differ hugely in spatial scale, from molecular size level of $10^{-10}\ m$ to the whole nervous system level of $10\ m$. All these levels have their own working theories, which contributes to brain function. Figure 2.2 visualises the organisations at different level in nervous system. This project mainly focused on the neurons level.

A reasonable way to view these levels is looking down though the brain. The brain is believed to be the most complicated organ in animals and is the core part of the central nervous system. The brain consists of two hemispheres. As Figure 2.3 illustrates, Four lobes are divided longitudinally across each hemisphere. Functionally, the frontal lobe is the motor controller, parietal lobe contains the sensory systems, temporal lobe is related to audition, learning and memory, and occipital lobe controls vision. Down-

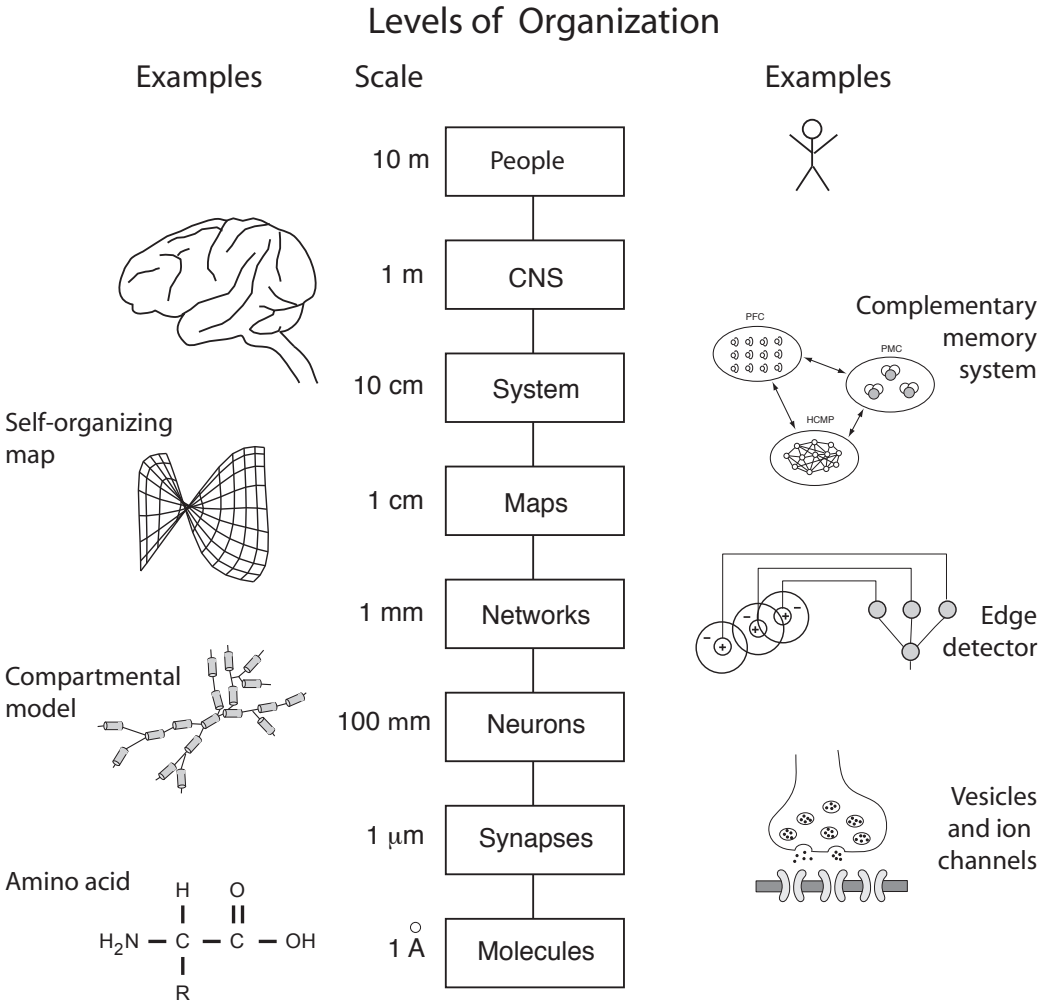

Figure 2.2: Levels of organisations of different spatial scales in central nervous system. Figure from Trappenberg(2010)

wards, the four lobes can be divided into smaller scaled and more specific sub regions called map. One of the famous division is the Brodmann's area consisting of fifty two subregions (Gazzaniga, 2000) (see figure 2.4). Comparing to lobes, these subregions are more functionally and cellular morphologically specialised (Gentner et al., 2001).

Organisation at the level of maps is composed of smaller scale organisation called network, which is a few of interconnected cells (Trappenberg, 2010). A particular organisation at map level called hippocampus is important in this project since the experimental data was recorded from it. Hence, It is worthy of introducing hippocampus in more details.

2.3 Hippocampus

The hippocampus may be the most studied brain structure. It is part of the limbic system (see figure 2.6) and is essential for memory consolidation and spatial navigation(El-Gaby et al., 2015; Suárez et al., 2014; Moser and Moser, 1998; O'keefe and Nadel, 1978). The hippocampus is found to be a major component of brain in vertebrates. It is named due to its resemblance to the marine animal seahorse. There are two hippocampuses found in mammals, located in each side of the brain. As figure 2.5 shows, in human beings, the hippocampus is located in the medial temporal lobe and beneath the cerebral cortex.

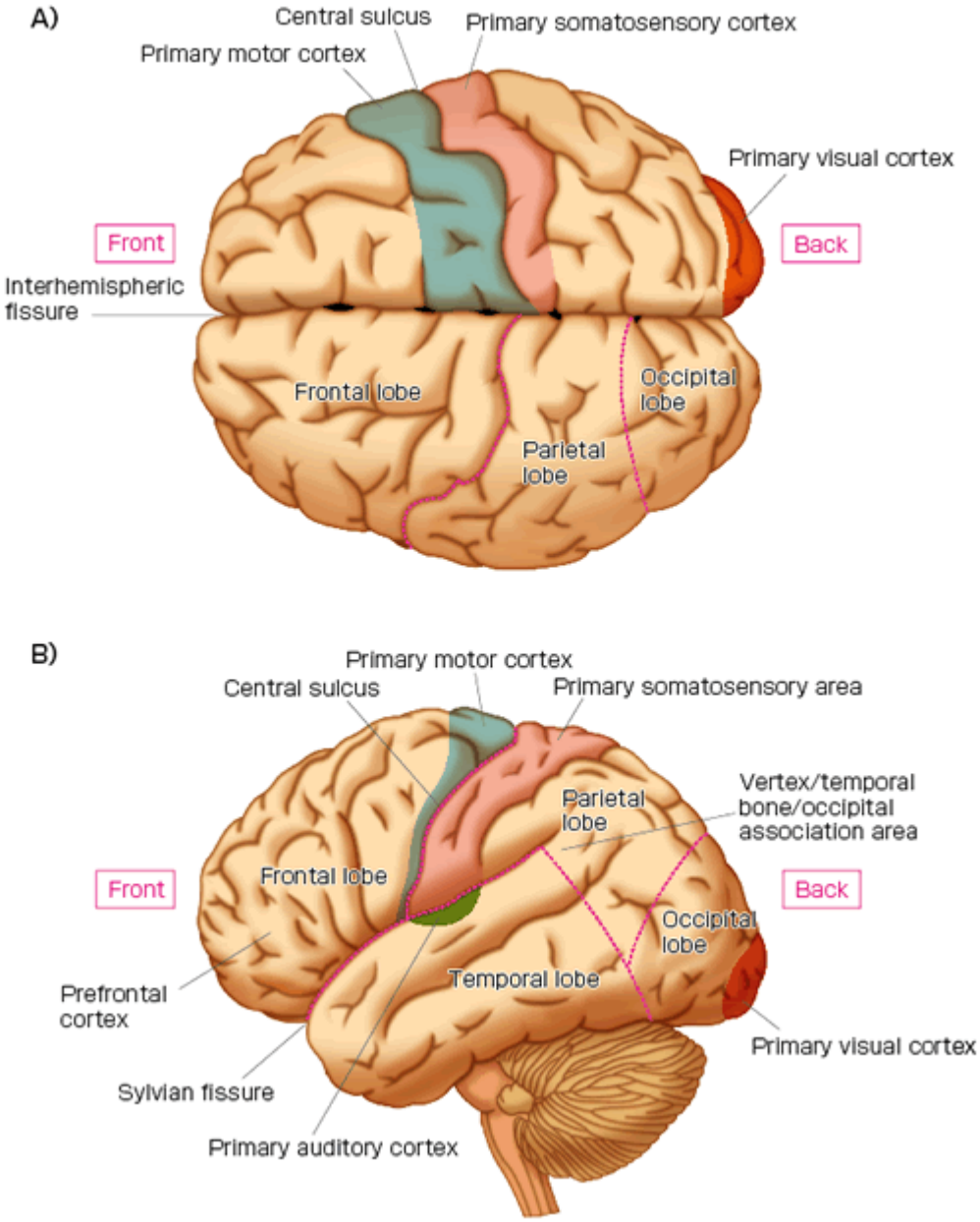

Figure 2.3: Four lobes in two hemispheres of the brain. Figure from http://csls-db.c.u-tokyo.ac.jp/

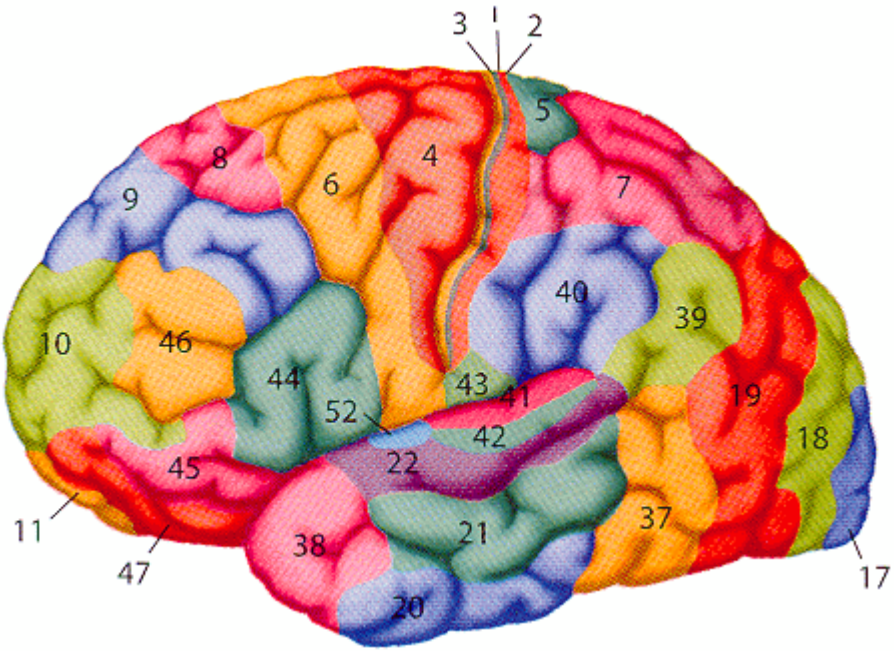

Figure 2.4: Brodmann's areas, a way to divide the brain according celllular morphology and organisation. Figure edited from Gazzaniga et al.(1998)

Figure 2.5: The figure shows the location of hippocampus in human brain. The front view is on the left and the side view is on the right. Figures from https://www.fil.ion.ucl.ac.uk/memo/brain.html

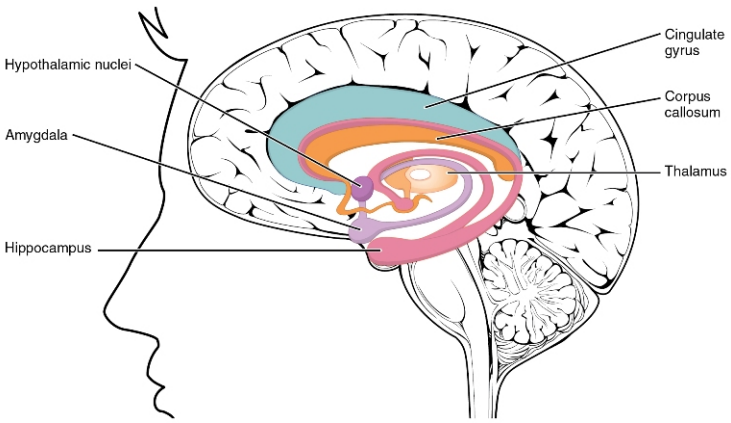

Figure 2.6: The figure shows the hippocampus of human in the limbic system. The frontal lobe is on the left, the occipital lobe at the right, and the temporal and parietal lobes have largely been removed to reveal the hippocampus (the two pink ”U” shaped parts) underneath. Figure from https://commons.wikimedia.org

This section will introduce the basic anatomy and biological background of the hippocampus, followed by the brief description of the information processing mechanisms inside the hippocampus.

2.3.1 Structure of The Mammalian Hippocampus

The hippocampus in mammals mainly consists of one basic cell type and its interneurones. These basic neurons are packed to form a layer. As shown in figure 2.7, the hippocampus itself is divided into two major ”U” shaped interlocking sections: the fascia dentata (area dentata, dentata gyrus) and the hippocampus proper(cornu ammonis). The fascia dentata comprises a buried blade and an exposed blade. The hippocampus proper can be further divided in a regio superior and a regio inferior. The regio supperior has a double row of medium-sized pyramidal neurons whose main apical dendrite gives off only small side branches and does not divide for several hundred microns. The regio inferior is the semi-circle close to the fascia dentata having large-sized pyramidal neurons whose dendrites bifurcate after leaving the soma. This type of large-sized pyramidal neuron contacts with mossy fibres of the dentate granule cells. The hippcampus proper is also divided into four fields, CA1-4, where CA is the shorthand for CornuAmmonis. The CA1 field almost coincides with the regio superior while the CA2 and CA3 can be seen as parts of the regio inferior. The existence of

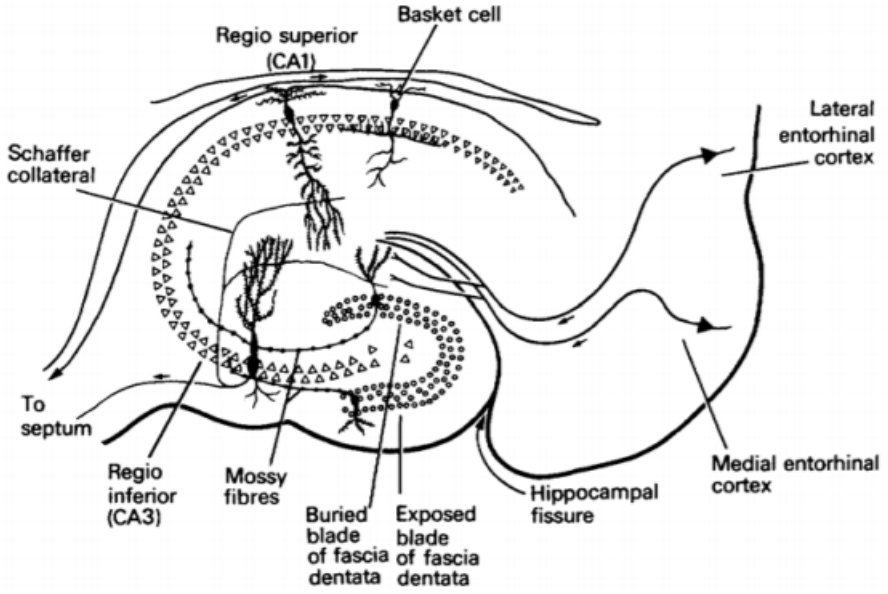

Figure 2.7: The figure shows the schematic diagram of the hippocampus structure in human brain. Its shows the divisions of the hippocampus: fasica dentata and hippocampus proper, regio superior and regio inferior, CA1 and CA3. It also has the schematic drawing of the basic neurons (medium-sized and large-sized pyramidal neurons) and its major interneurones(Basket cell). Figure from (O'keefe and Nadel, 1978)

CA2 field as a separate area has been challenged since there is no difference found in terms of connections or histo-chemical staining properties compared with CA3. CA4 is next to or even blurs into the fascia dentata.(O'keefe and Nadel, 1978)

The basic organisation in the CA1 and CA3 fields is the same: large neurons are ordered like a sheet with their cell bodies being packed together in a layer and their dendrites running away in the same direction. The large neurons in CA3 are giant pyramidal neurons while in CA1 are comparably smaller.

An important type of interneurones is the basket cell. It can be differentiated from the pyramidal neurons in several ways. The basket cells do not have thorn shaped spines on their dendrites and thus do not contact with the mossy fibres. The basket cells just send their axons within the local areas while the pyramidal neurons send theirs out of this area. The cell body of the basket cell is mainly located in the principal cell layer, sometimes slightly below. Its axon goes through the cell layer and reaches a

considerable distance. These layers are important and worth brief description.

2.3.2 Layering in the Hippocampus

The fascia dentata and hippocampus proper differ in cell layers in their structure (see figure 2.8 (b)). The fascia dentata is made of three layers (summarised in table 2.1). The cell bodies of granule cell are densely packet to form the granule layer. Their dendrites and afferents form the molecular layer. The axons of granule cells gathering to form the mossy fibre bundle, together with some non-granule cells, form the third layer, the polymorph layer.

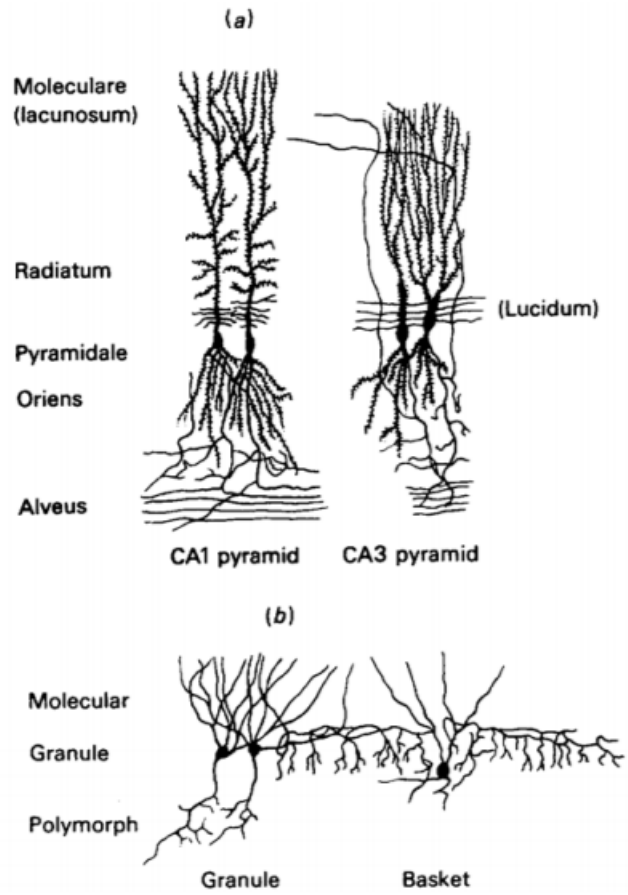

Figure 2.8: The figure shows the detailed schematic diagram of the hippocampal cells. The top panel (a) depicts examples of pyramidal neurons in CA1 and CA3. The bottom panel (b) illustrates the examples of dentate granule cells and a basket cell. Figures from (O'keefe and Nadel, 1978)

The hippocampus proper is further divided into more layers (see figure 2.8 (a), summarised in table 2.2). The alveus layer is formed by the axons of the pyramidal neurons. The stratum oriens layer is between the alveus and the pyramidal cell bodies and is formed mainly by the basal dendrites of the pyramidal cells and some basket cells. The pyramidal layer, as the name indicated itself, is dominated by the cell bodies of pyramidal cells. The radiatum layer and the moleculare(lacunosum) layer are essentially segments of dendritic tree. A particular layer, stratum lucidum. is recognised only in CA3 field, which is interposed between the pyramidal layer and the radiatum layer, contacting with the mossy fibres from the dentate granule cells in dentata area. These layering structures are important in signalling and communication in the hippocampus.

Layer Index	Layer Name	Component(s)
1	Molecular	Dendrites and afferents of the granule cell
2	Granule	Cell bodies of the granule cell
3	Polymorph	Mossy fibre bundle(Axons of the granule cells), Non-granule cells

Table 2.1: Layers in the fascia dentata.

Layer Index	Layer Name	Component(s)
1	Alveus	Axons of the pyramidal neurons
2	Stratum oriens	Basal dendrites of the pyramidal cells, basket cells
3	Pyramidal	Cell bodies of pyramidal cells
4	Stratum radiatum	The proximal segments of the apical dendritic tree
5	Stratum moleculare	The distal segments of the apical dendritic tree
6	Stratum lucidum	Mossy fibre (only in found CA3)

Table 2.2: Layers in the hippocampus proper.

It is these different cells in layers of the hippocampus that enable the hippocampus to play an important role in spatial navigation, memory solidification and so on. According to figure 2.2, at the spatial level of cells, neurons are specialised cells capable of

electrical signalling (Nicholls et al., 2001). They are capable of transmitting information to other neurons. The information processing ability of neuron results from its subcellular mechanism. Hence, neuron, as the basic signalling component in central nervous system, is worthwhile of detailed investigating to assist understanding functional connection in the brain.

2.4 Nerve Cells: Neurons

The central nervous system consists of two categories of cells, neurons and glial cells. Normally, glial cells are thought of mainly providing supporting action (Charles et al., 1991; Parpura et al., 2012). On the other hand, Neurons are highly-specialised cells being able to processing information in central nervous system (Dayan and Abbott, 2001). It is the signalling property of a single neuron that provides the cornerstone of more sophisticated and specific information processing abilities of higher level organisations like network, system and brain. From this essence, Studying the mechanism of electric signalling and biochemical processing in detail is necessary. This section first introduces the structure of neurons briefly. Afterwards, the information-processing mechanism of single neuron and synaptic mechanisms will be outlined.

2.4.1 Neuronal Structure

Neurons have a common cellular structure like other biological cells. As figure 2.9 illustrated, neurons varying morphologically. However, all neurons have typical cellular components. Specifically, a neuron has a nucleus, a cell body named soma, soma root-like extensions. According to the different directions in signal transmission, these extensions are further divided into two categories named axons and dendrites and they both are related to information processing. Synapses are the specialised junctions between neurons (Kandel et al., 1995). Dendrites receive external inputs from presy-

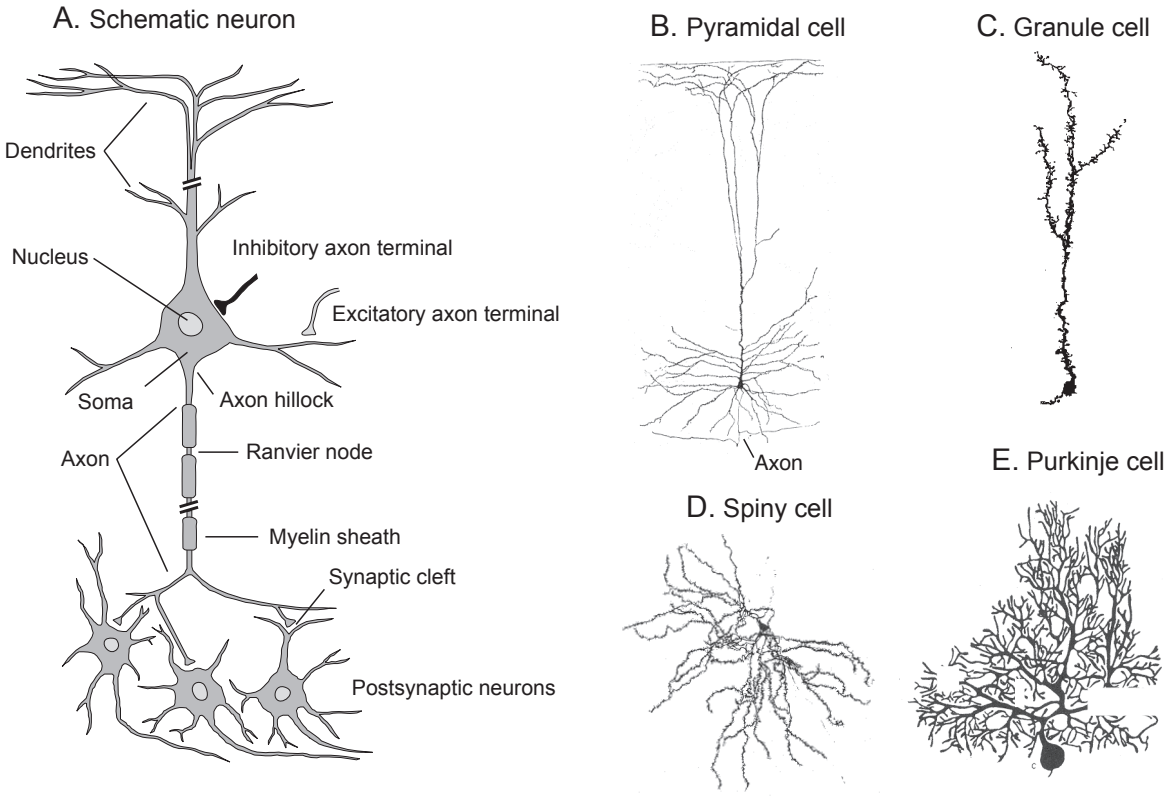

Figure 2.9: (A) Schematic neuron structure with outlined components widely exist in different neuron types.(B)Pyramidal neuron, being found in the motor cortex, (C)Granule cell, being found in the olfactory bulb of a mouse, (D)Spiny neuron, being found in the caudate necleus, (E) Golgi-stained purkinje neuron, being found in the cerebellum. Figure form Trappenberg(2010)

naptic neurons and forward the electric signals to soma to be integrated. Axons send the signals which have been integrated and processed in soma along the axons outward to root-like ends (Trappenberg, 2010).

2.4.2 Signalling within Neurons

The membrane potential is defined as the difference in electric potential between inside and outside the neuron. The difference in potential results from the different concentrations of ions on the two sides of membrane. The variance of ionic concentrations causes movements of ions, which form ionic currents through the membrane. These ionic currents are essential to the neurons' signalling ability. The cellular membrane is permeable to specific ions using a special protein called an ion channel, which is

embedded in the membrane. Ion channels let specific ions flow in or out the cell, for example sodium (Na^+), potassium (K^+), calcium (Ca^{2+}) and chloride (Cl^-). For this project, only leakage channel, voltage-gated channel and ion pump are taken into account. Leakage channels allow Na^+ and K^+ to flow across the membrane from high concentration side to lower concentration side. Voltage-gated channels are a type of transmembrane proteins which form ion channel activated by variations of the electrical membrane potential near the channel (Gazzaniga, 2004; Kandel et al., 2000). As figure 2.10 illustrates, the leakage channel drives the resting potential of neurons and it is treated as always open. The on-or-off state of voltage-gated ion channels relies on the membrane potential while the ion pump functions to balance the efforts of ion channels by pumping the ion against the ionic concentration(Hille et al., 2001; Gouaux and MacKinnon, 2005).

2.5 Synaptic signalling mechanism

Dendrites and axons enable neurons receiving and sending signals from and to other neurons. The specialised site where the sending neuron contacts with the receiving neuron is called a synapse. Information transferring from the presynaptic neurons to the postsynaptic neuron is based on sophisticated electro-chemical mechanisms. Generic features exist in information processing in synapses (see figure 2.11). Thus the signals from the presynaptic neurons have effects on the local membrane potential of the postsynaptic neurons, which contributes to the generation of action potentials (spikes) in the postsynaptic neurons.

Synaptic signalling describes how presynaptic and postsynaptic neurons communicate with each other. Neurotransmitters play important role in synaptic signalling procedure. As figure 2.11 shows, An action potential arriving at the axon terminal opens the voltage-gated ion channel of calcium Ca^{2+}, and then results in the flow of Ca^{2+} inwards to the presynaptic neuron. With the concentration of Ca^{2+} increasing inside the presynaptic axon terminal, the synaptic vesicles in which the neurotransmitters group

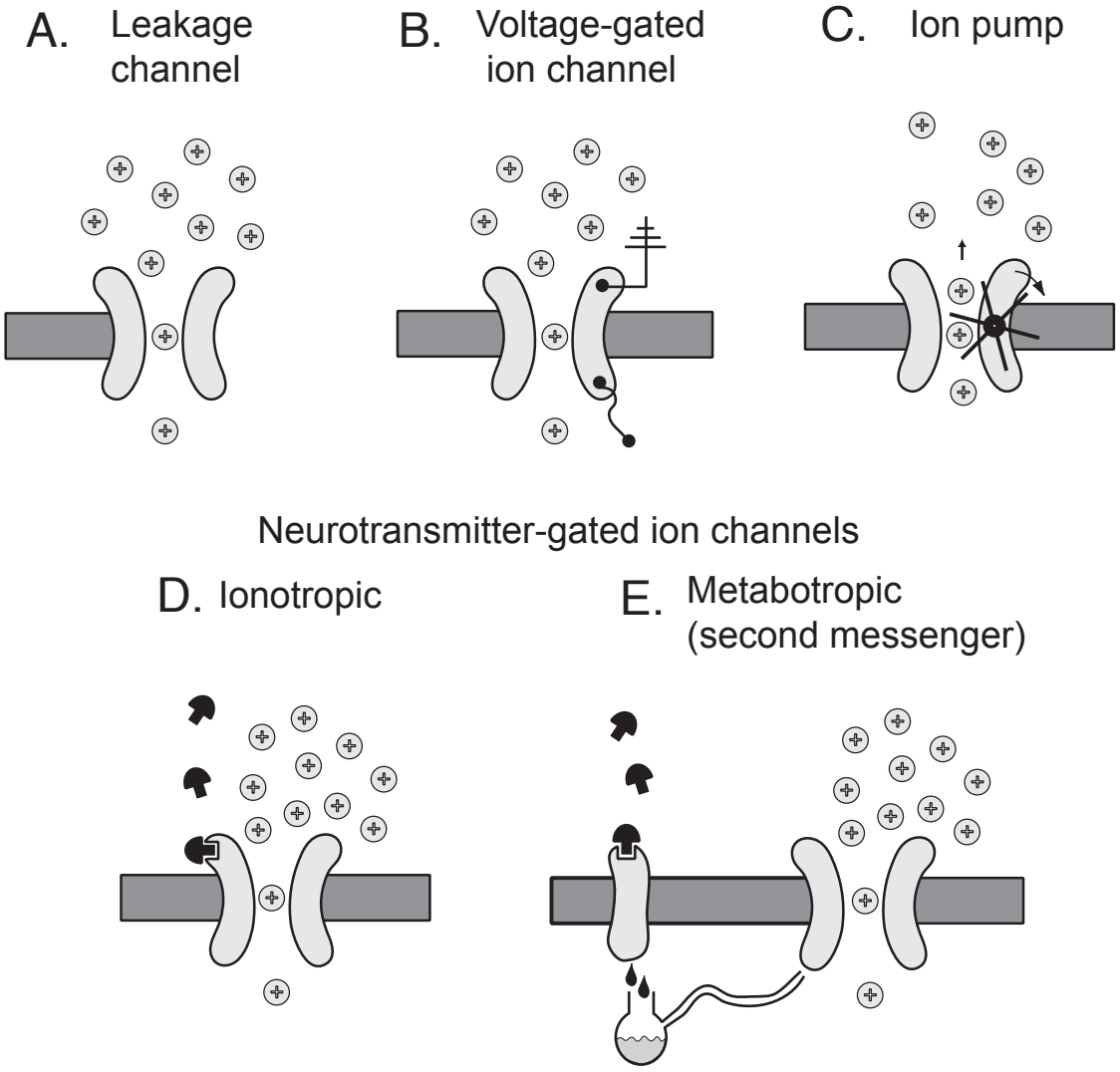

Figure 2.10: Schematic illustrations of different types of ion channels. (A) Leakage channels open all the time. (B) Voltage-gated ion channels open or close based on the membrane potential. (C) Ion pumps transmit ions against the ionic concentrations. (D and E) Details of neurotransmitter-gated ion channels and they are approximately regarded as Voltage-gated ion channels. Figure from (Trappenberg, 2010)

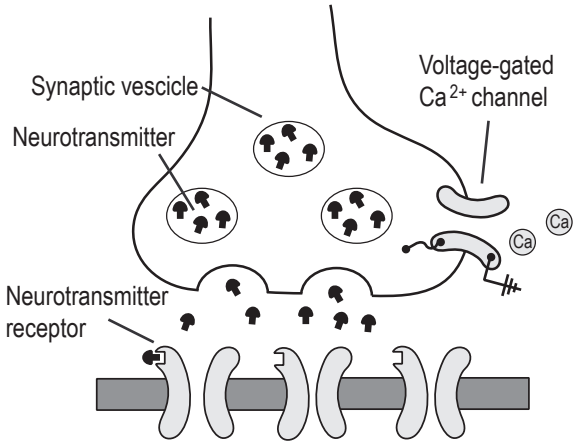

Figure 2.11: Schematic illustration of the synaptic signalling procedure. Figure from (Trappenberg, 2010)

and store bind with receptors and then merge together with the presynaptic membrane to release neurotransmitters. These released neurotransmitters drift across the gap between the axon and postsynaptic dendrites and bind with the corresponding receptors embedded in the postsynaptic membrane to activate or inactivate ion channels (Kandel et al., 2000).

Ion channels open or close after the neurotransmitter binds with receptors. These ions can flow through open channels to charge or discharge the postsynaptic membrane. Therefore, the variation of electric potential of the postsynaptic membrane is generated, which is described as postsynaptic potential (PSP). PSPs can be distinguished into excitatory postsynaptic potentials (EPSPs) and inhibitory postsynaptic potentials (IPSPs). The former increased the probability of neuron firing, while the latter effects reversely to decrease the firing probability. The generation of an action potential in the soma of the postsynaptic neuron is then the integrated effect of EPSPs and IPSPs. (Kandel et al., 1995; Trappenberg, 2010)

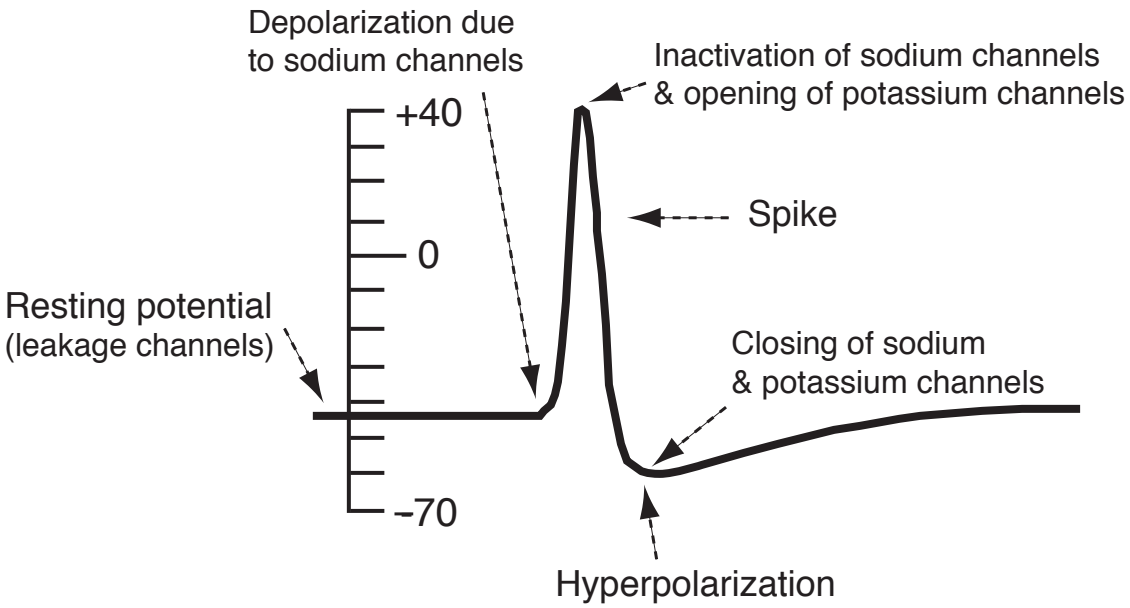

Figure 2.12: A prototypical form of an action potential. It apparently shows the resting potential and two phases: depolarisation and hyperpolarisation. sodium channels opening results in depolarisation. and potassium channels opening causes the voltage going down to a level lower than resting potential. Then both channels closed and the potential goes back to resting level. Figure from (Trappenberg, 2010)

2.6 Action Potentials (Spikes)

Action Potentials, also known as spikes, enable neurons to transmit signals along over long distance because they do not attenuate after moving away from the initial point (Kandel et al., 2000). This property enriches the research value of action potentials.

Figure 2.12 shows a schematic drawing of an action potential. Two voltage-dependent ion channels for potassium K^+ and sodium Na^+ respectively and leakage channel are considered (see figure 2.13). As figure 2.12 shows, the left part is the resting potential which is related to the static leakage channel. Leakage channel is selectively permeable to K^+ and the concentration of K^+ presents higher inside the neuron. Hence, the K^+ diffuse outward the cell and the diffusion of K^+ results in the inside membrane being negatively charged while the outside membrane being positive charged. The different charging on two sides of membrane then form the difference in potential across the membrane and this potential difference effects against the K^+ diffusion. At a certain point, the force due to the potential difference balances chemical force due

to ionic diffusion caused by the ionic concentration gradient. Then the equilibrium potential of K^+ is achieved. The resting potential, which according to figure 2.12 is around $-45mV$, is determined by the potassium equilibrium potential (Kandel et al., 2000; Dayan and Abbott, 2001).

The rapidly rising phase after resting potential is called depolarisation. Neurotransmitters-gated channels depolarises the neuron sufficiently to open the voltage-gated sodium (Na^+) ion channel. Since the concentration of Na^+ outside neuron is higher, Na^+ will flow inwards through the membrane to reduce the intracellular negativity. The inward Na^+ exceeding outward K^+ immediately increases the potential inside the neuron and reaches the firing threshold. Afterwards, within a very shot time, the membrane potential peaks at about $40mV$.

The inactivation of the voltage-gated sodium ion (Na^+) channel happens at the peak voltage moment when the voltage-gated potassium ion (K^+) channel open. The outflow of K^+ through both the leakage channel and voltage-gated K^+ channel drives the membrane potential downward past the resting level and undershooting to the lowest point about $65mV$. Afterwards, the resting potential is recovered at the end of the refractory period. Refractory period is a short duration in which the action potential complete the initial process before initiation of the next action potential (Trappenberg, 2010).

The mechanism of action potential generation described in this section achieves a good balance between the biological details and the simplicity of each stages, which is helpful to build computational spiking neuron models accordingly.

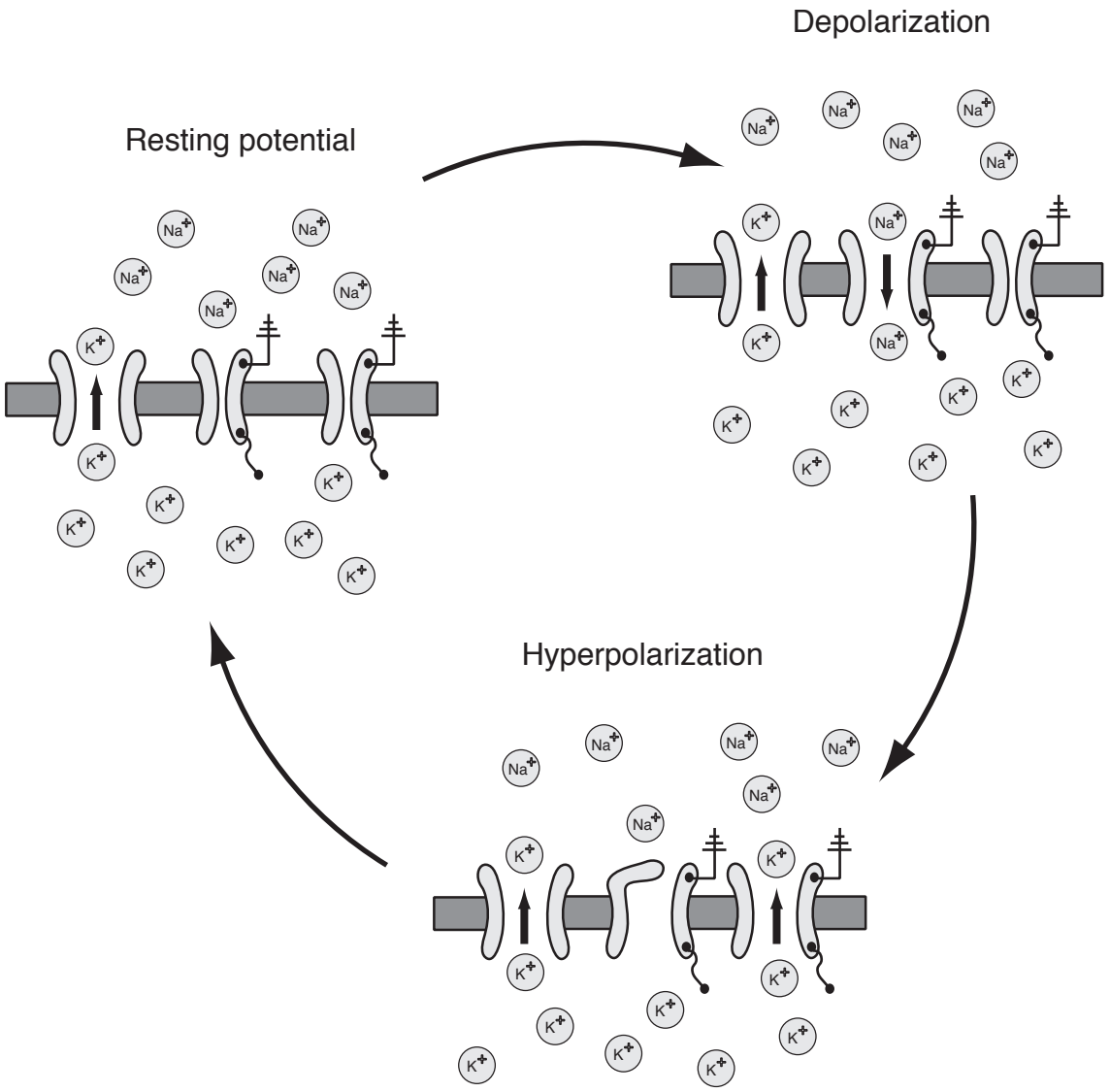

Figure 2.13: Schematic depiction of mechanism to generate spikes. During the resting potential period, only leakage channel opens and efflux of K^+ causes the potassium equilibrium potential. Depolarisation results from the opening of voltage gated sodium channel and inward flow of Na^+. The blocked sodium channel and opened voltage gated potassium channel are the reason of hyperpolarisation. Figure from (Trappenberg, 2010)

2.7 Models of spiking neuron

Multiple mechanisms coexist in the procedure of information transferring between sending end (presynaptic neuron) and the receiving end (postsynaptic neuron). They share the generic information transferring feature of synapses that the signals from a presynaptic neuron can trigger the change of state a postsynaptic neuron to generate an electric pulse on the postsynaptic neuron. Hence, how the change of electric potential invokes generation of the pulse is essential.

During the last a few decades, different computational models has been developed to illustrate the generating process quantitatively. They all played very important roles in improving the understanding of information processing mechanisms in the brain. They are useful tools to generate simulated neural spike train signals on which evaluations of algorithms can be conducted to prove the usefulness of the algorithms. In this section, Four spiking neuron models are briefly discussed. The Hodgkin-Huxley model focuses mainly on quantifying the ion channel dynamics to depict the properties of voltage-dependent meambrane conductances in action potential generation (Hodgkin and Huxley, 1952b). The Leaky Integrate-and-fire model mimics the dynamic responses to the integration of presynaptic inputs (Dayan and Abbott, 2001; Burkitt, 2006). The Izhikevich model is computationally efficient, which is convenient to generate large population of spike train signals (Izhikevich, 2007). The point cortical neuron model is useful to simulate neuronal network which serve as the surrogate data to evaluate the proposed the approaches (Troyer and Miller, 1997)

2.7.1 Hodgkin-Huxley Model

The three phase procedure described in section 2.6 is mathematically described by Hodgkin-Huxley model using a four-equations set (Hodgkin and Huxley, 1952b; Dayan and Abbott, 2001). Hodgkin-Huxley model represents the membrane potential as an

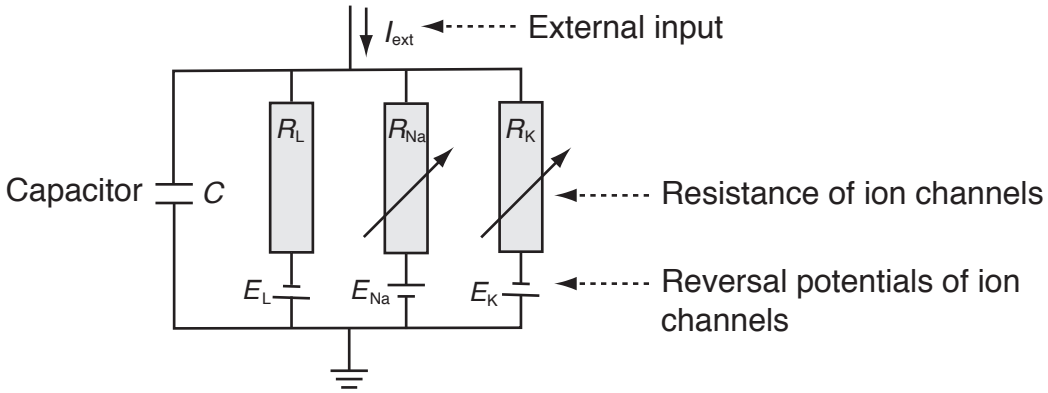

Figure 2.14: Representation of an equivalent circuit for Hodgkin-Huxley model including a capacitor, two variable resistors and a static resistor. The two variable resistors approximate voltage-dependent conductances. The static resistor represents small leakage current. Each resistor has a corresponding battery. Figure from (Trappenberg, 2010)

electric circuit model. As figure 2.14 shows, This circuit is constructed by a capacitor, two variable resistors and one static resistor in parallel. The three resistors with their corresponding batteries model the ion channels while the capacitor maintains the electric potential difference across the ion channels on which the membrane potential can be measured. Such a circuit model is capable of directly inspiring the mathematical description of a generation of action potential by considering the potential-current ($V - I$) relationship on a capacitor (capacity C):

$$C\frac{dV(t)}{dt} = I(t) \tag{2.1}$$

where C denotes the capacity of the capacitor. Specifically under the context of Hodgkin-Huxley model, the first step is to split the membrane current into two parts, namely capacitive current and ionic currents. Thus based on Kirchhoff's law:

$$I(t) = C\frac{dV}{dt} + I_i \tag{2.2}$$

where I is the membrane current density (inward current positive), I_i is the ionic current density (inward current positive); V is the displacement of the membrane potential from its resting value (depolarisation negative), C is the membrane capacity and t is time.

The ionic current can be further subdivided into three different components repre-

senting the movement of different ions. The components carried by sodium ions, potassium ions and other ions through leakage channel are denoted as I_{Na}, I_K and I_l respectively. The ionic current is the sum of these three currents:

$$I_i = I_{Na} + I_K + I_l \tag{2.3}$$

Since the permeability of the membrane can be measured in terms of conductance (Hodgkin and Huxley, 1952a; Hille et al., 2001), a variable conductance g_i can be used to model the ion channel dynamics. Using Ohm's law, the relationship between the electric potential, the current and the conductance is formed as:

$$I_i = g_i(E - E_i) \tag{2.4}$$

where E_i is the equilibrium potential for the ion channel which results from the concentrations within and outside the neuron. Each individual ionic current with their corresponding ionic conductances g_{Na}, g_K, g_l are:

$$I_{Na} = g_{Na}(E - E_{Na}) \tag{2.5}$$

$$I_K = g_K(E - E_K) \tag{2.6}$$

$$I_l = g_l(E - E_l) \tag{2.7}$$

where E_{Na} and E_K are the equilibrium potential for the sodium and potassium ions, and E_l is equilibrium potential for leakage channel. In order to express the electric potential directly in terms of the displacements from resting potential, denoted as V, V_{Na}, V_K and V_l, an absolute value of resting potential, denoted as E_r, should be removed from every potential terms in equations (2.4) to (2.7), thus:

$$V = E - E_r \tag{2.8}$$

$$V_{Na} = E_{Na} - E_r \tag{2.9}$$

$$V_K = E_k - E_r \tag{2.10}$$

$$V_l = E_l - E_r \tag{2.11}$$

Then the equations for the individual ionic currents can be written in the form:

$$I_{Na} = g_{Na}(V - V_{Na}) \tag{2.12}$$

$$I_K = g_K(V - V_K) \tag{2.13}$$

$$I_l = g_l(V - V_l) \tag{2.14}$$

In the theory of action potential generating, the sodium and potassium channels are voltage and time dependent. This fact is reflected in the dynamical property of the membrane conductance in Hodgkin-Huxley model. Three dynamical variables have been introduced: the variable n indicates the activation of the potassium channels, and the variables m and h indicate the activation and inactivation of sodium channels, respectively (Hodgkin and Huxley, 1952a). The dynamics of the conductances are represented by a product of constant conductance, denoted by a subscript 0, with a set of time and voltage dependent variables $n(V,t)$, $m(V,t)$ and $h(V,t)$. For the potassium channel, the conductance is represented as:

$$g_K(V,t) = g_{K0}n(V,t)^4 \tag{2.15}$$

It has been pointed out that the biological principle of this equation is that the potassium ion can flow across the membrane only when four similar particles occupy a certain region of the membrane (Hodgkin and Huxley, 1952b). This has been modelled as four independent events n.

Similarly, the equation expressing the dynamics of sodium channels can be constructed as:

$$g_{Na}(V,t) = g_{Na0}m(V,t)^3h(V,t) \tag{2.16}$$

This equation is based on the principle that the sodium conductance is activated when three activating molecules synchronously occupy sites inside the membrane while another site is not occupied by an inactivating molecule. They are represented by in-

dependent events m and h where m infers that the one activating molecule is on the correct site, while h indicates that one inactivating molecule is not blocking the site(Hodgkin and Huxley, 1952b).

The conductance modelling the leakage channel is static, so the conductance value can be regarded as a constant:

$$g_l = g_{l0} \tag{2.17}$$

These three dynamical variables are modelled using first order differential equations:

$$\frac{dn}{dt} = \alpha_n(1-n) - \beta_n n \tag{2.18}$$

$$\frac{dm}{dt} = \alpha_m(1-m) - \beta_m m \tag{2.19}$$

$$\frac{dh}{dt} = \alpha_h(1-h) - \beta_h h \tag{2.20}$$

where the parameters α with specific subscripts are transfer rates from outside to inside while the parameters β with specific subscripts are transfer rate in the opposite direction.

An alternative form to describe the time voltage dependence of these three variables are:

$$\frac{dn}{dt} = -\frac{1}{\tau_n(V)}[n - n_0(V)] \tag{2.21}$$

$$\frac{dm}{dt} = -\frac{1}{\tau_m(V)}[m - m_0(V)] \tag{2.22}$$

$$\frac{dh}{dt} = -\frac{1}{\tau_h(V)}[h - h_0(V)] \tag{2.23}$$

Figure 2.15(A) shows the voltage-dependent property of these variables. The resting potential is set as 0 here and the X_0 value quantifies the probabilities of occurrence of the events described by the specific variables. At the resting potential level, the variable n_0 (potassium channel) has activation probability 0.4, while the other two variables representing sodium channel vary significantly. with m_0 close to zero value

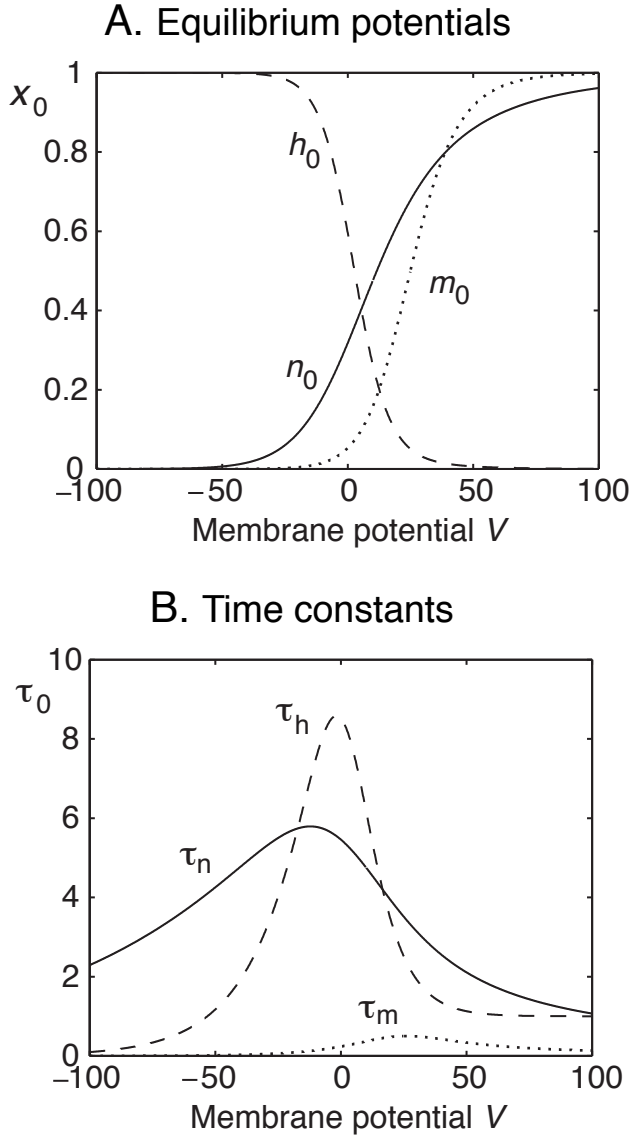

Figure 2.15: (A):The equilibrium functions (B) time constants for dynamical variables n, m and h in Hodgkin-Huxley model. The 0 value in the middle of horizontal axis represents the resting value. Figure from Trappenberg (2010)

indicating a small activation chance and the variable h_0 higher at probability 0.6. As the depolarisation begins, n_0 and m_0 increase. In contrast, h_0, the variable for inactivation of sodium channel, approaches zero.

Figure 2.15(B) plots the time constants of the three variables (in msec) against the membrane potential (in mV). Time constants imply the duration for these variables, n, m and h to approach their equilibrium values n_0, m_0 and h_0 at a voltage value.

According to equation (2.3), the entire ionic current then can be expressed as:

$$I_i = g_{K0}n^4(V - V_K) + g_{Na0}m^3h(V - V_{Na}) + g_{l0}(V - V_l) \tag{2.24}$$

The standard four differential equation form is constituted by substituting equation (2.24) into equation (2.17) along with the first order differential equations of the three dynamical variables:

$$C_M\frac{dV}{dt} = I(t) - g_{K0}n^4(V - V_K) - g_{Na0}m^3h(V - V_{Na}) - g_{l0}(V - V_l) \tag{2.25}$$

$$\tau_n(V)\frac{dn}{dt} = -[n - n_0(V)] \tag{2.26}$$

$$\tau_m(V)\frac{dm}{dt} = -[m - m_0(V)] \tag{2.27}$$

$$\tau_h(V)\frac{dh}{dt} = -[h - h_0(V)] \tag{2.28}$$

2.7.2 The Leaky Integrate-and-Fire Neuron Model

The Hodgkin-Huxley model provides a detailed description of the basic principle of action potential generation. However, its four differential equation form is computationally consuming when investigating a large scale population behaviours or networked neurons. Hence, simpler spiking neuron models are also used. The Leaky Integrate-and-Fire model makes effort on ignoring the sophisticated detail of ion chan-

nel dynamics and focusing on the dynamic integration of synaptic input, spike timing (Trappenberg, 2010).

Figure 2.16 gives a schematic description of the Leaky Integrate-and Fire (LIF) model. The equivalent circuit is in the dashed circle on the right hand side consisting of a capacitance C in parallel with a resistor R. The input current can be divided into two components:

$$I(t) = I_C(t) + I_R(t) \tag{2.29}$$

where $I(t)$ is the total input current. Since they are connected in parallel, the voltage across the resistor and capacitance are the same, denoted as $V(t)$. The input current can be expressed as:

$$I(t) = \frac{V(t)}{R} + C\frac{dV(t)}{dt} \tag{2.30}$$

In order to introduce the time constant $\tau_m = RC$, Equation (2.30) can be multiplied by the resistance value R and the product RC can be substituted as time constant τ_m:

$$\tau_m \frac{dV(t)}{dt} = -V(t) + RI(t) \tag{2.31}$$

This equation shows that non-linear voltage dependent dynamics are neglected. Instead, the subthreshold dynamical feature of the membrane potential is described using a first order linear differential equation.

A typical way to approximate the input current $I(t)$ is to treat it as the sum of synaptic currents from firings of presynaptic neurons. This sum is a linear combination with different weight values representing synaptic efficiency. under the assumption that these presynaptic neurons do not interact with each other, the total input current to the postsynaptic neuron is quantified as:

$$I(t) = \sum_{j=1}^{n} \sum_{t_j^f = t_1^f}^{t_n^f} w_j \alpha(t - t_j^f) \tag{2.32}$$

where the variable t_j^f indicates the firing time of presynaptic neuron j with the su-

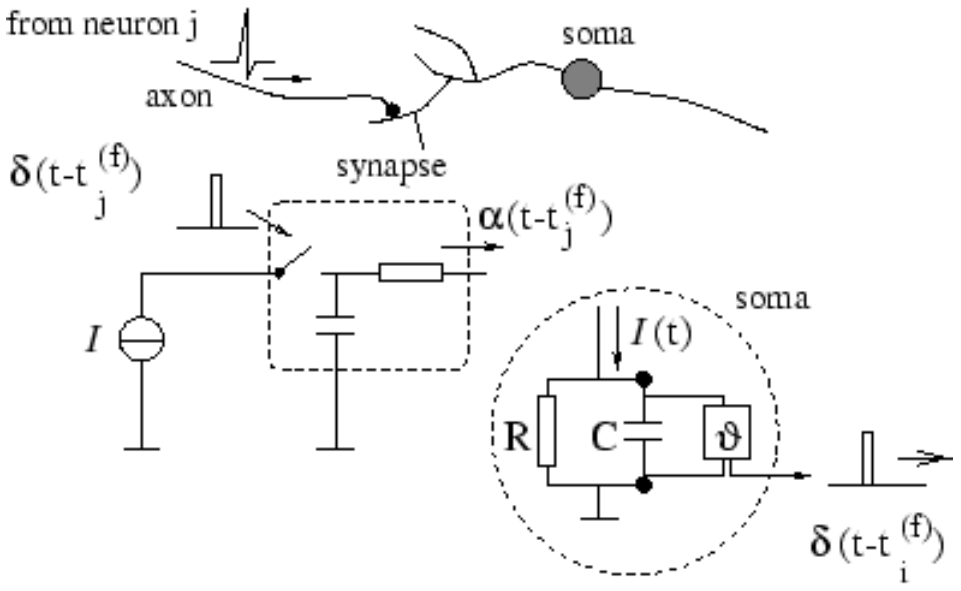

Figure 2.16: The basic circuit of Leaky Integrate-and-Fire model. The left part inside the dash square represents generation of an input current. The right part inside the dash circle is the main part of LIF model: the voltage across the capacitance C is compared with a threshold voltage V to decide whether generates a output pulse or not. Figure from (Dayan and Abbott, 2001)

perscript f meaning it firing, n indicates the number of the presynaptic neurons, and the α-function represents the time course of postsynaptic current. The choice of α-function varies. The simplest one is a Dirac δ function $\alpha(t) = \delta(t)$. More realistic choices may involve a finite duration of postsynaptic current, for example, an exponential decay (Gerstner and Kistler, 2002).

Since the capacitance C is charged by the input current $I(t)$, the electric potential $V(t)$ across it increases. When $V(t)$ reaches a threshold voltage, V_{thr}, an output action potential is generated. The output action potential is parameterised by its timing. In contrast to the firing time variable representing the presynaptic neuron's firing time, the firing time of the postsynaptic neuron in LIF model is denoted as t^f without subscript. An output spike occurs when the membrane potential $V(t)$ satisfies the relation:

$$V(t^f) \geq V_{thr} \tag{2.33}$$

A short duration δ after a spike at t^f, the potential is reset to the resting potential V_{res}

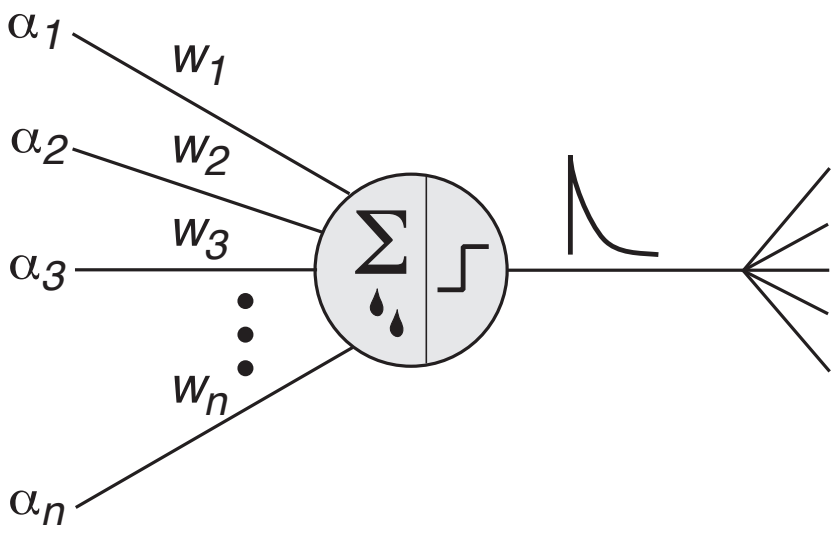

Figure 2.17: A schematic description of a leak Integrate-and-Fire model, which is often used in networked neurons simulation. This neuron integrates external inputs to yield a input current $I(t)$ weighted summation of different postsynaptic currents with corresponding weight values w_j. This input current drives the membrane potential to reach a threshold resulting in a output spike. Figure from Trappenberg (2010)

where $V_{res} < V_{thr}$:

$$\lim_{\delta \to 0} V(t^f + \delta) = V_{res} \tag{2.34}$$

LIF is simpler compared with Hodgkin-Huxley model. It captures the spiking dynamics by depicting the integration of presynaptic inputs and comparing the integration to a threshold. It is computationally efficiency, but some subthreshold dynamics are neglected, which is not suitable to model sophisticated firing patterns.

2.7.3 Izhikevich Model

Computational Modelling is always inevitably a trade off between abstraction and reality, or computational efficiency and detail-richness. The Hodgkin-Huxley model provides accurate insight to analyse the dynamical properties of ion channels in individual neurons. However, it is too computationally demanding to be applied on analysis of large scale networked neurons (Hodgkin and Huxley, 1952b). On the other hand, the LIF model is computationally efficient because of the linearity in membrane potential $V(t)$, but it is not detailed enough to catch a wide range of subthreshold dynamics in

individual neurons, so it is not capable of modelling any sophisticated firing patterns (Gerstner and Kistler, 2002). As both the scale of a network and the firing patterns of neurons inside the network are becoming more sophisticated, a model which is able to replicate different firing patterns while consuming reasonable calculation resources is required. The Izhikevich Model proposes a way using two coupled differential equations to achieve a balance between computational efficiency and the ability of capturing variety of firing pattern in neurons (Izhikevich et al., 2003).

A recovery variable, $u(t)$ has been introduced in Izhikevich model to indicate the inactivation of sodium channel and hyperpolarising potassium channels. This enable the two coupled differential equations to model typical spike patterns of real neurons. Another feature of this model is that, like Hodgkin-Huxley, the Izhikevich model does not have a constant threshold. The model is:

$$\frac{dV(t)}{dt} = 0.04V^2(t) + 5V(t) + 140 - u(t) + I(t) \tag{2.35}$$

$$\frac{du(t)}{dt} = a(bV(t) - u(t)) \tag{2.36}$$

with the reset conditions when $V(t) = 30$, then:

$$V(t) = c \tag{2.37}$$

$$u(t) = u(t) - d \tag{2.38}$$

where $V(t)$ is membrane potential, and four parameters a, b, c and d function differently to generate diverse firing patterns. The parameter a controls the time scale of the recovery variable $u(t)$ with higher values indicating quicker recovery. The parameter b controls the sensitivity of $u(t)$ to the fluctuation of the membrane potential $V(t)$. The reset value of membrane potential $V(t)$ after spiking is described by parameter c, which is typically set as $c = -65\ mV$. The reset value of the recovery variable $u(t)$ is described by parameter d. As shown in figure 2.18 , the combination of different a, b, c and d values simulates different firing behaviours.

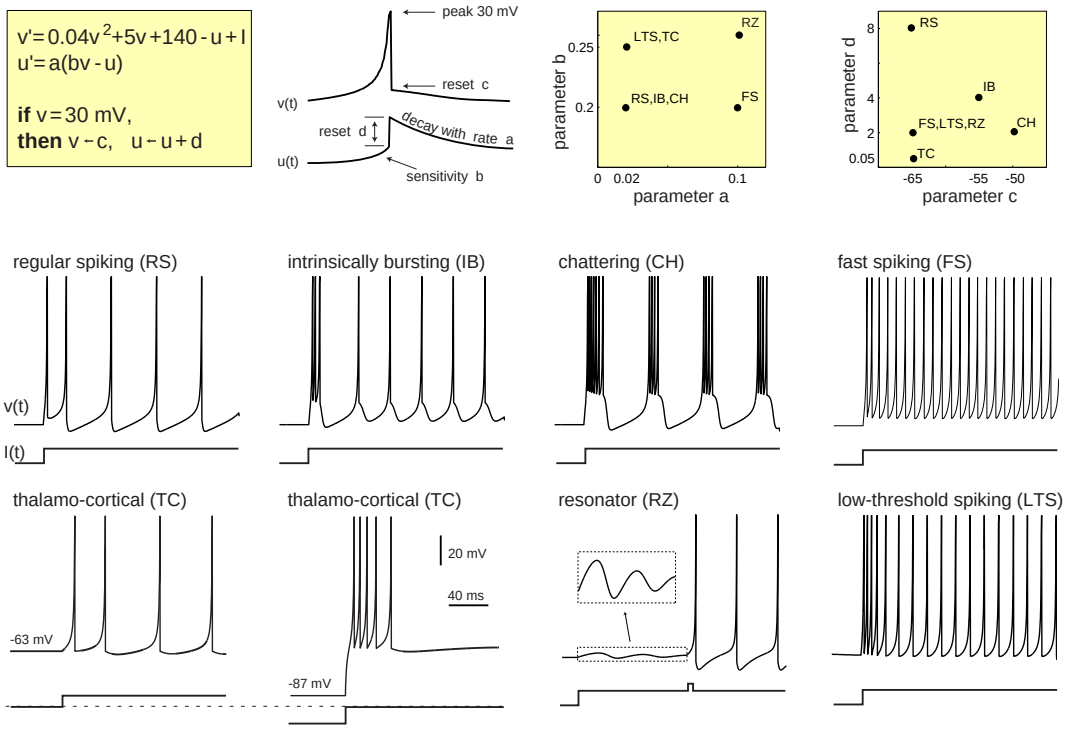

Figure 2.18: Different types neuron firing pattern are modelled by different combinations of parameters a, b, c and d. The values of each parameters used to generate these firing pattern can be found in the third and fourth subfigures in the first row. At the bottoms of insets, a Direct current $I(t) = 10$ is displayed. Figure from (Izhikevich et al., 2003)

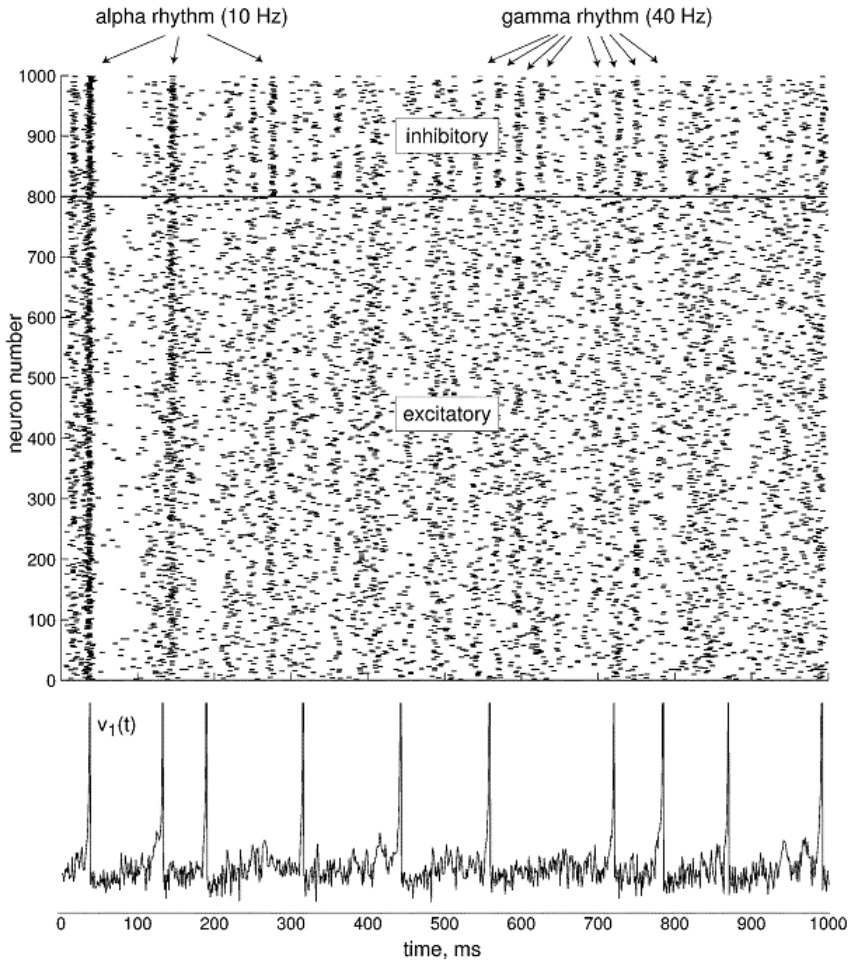

Figure 2.19: Simulation of a network of 1000 randomly coupled spiking neurons. Top: spike raster shows episodes of alpha and gamma band rhythms (vertical lines). Bottom: typical spiking activity of an excitatory neuron. All spikes were equalized at +30mV by resetting v1 first to +30mV and then to c. Figure from (Izhikevich et al., 2003)

The lower computational demands makes the Izhikevich model capable of simulating networked neurons. Figure 2.19 illustrates where the model was tested to run a simulation of 10000 spiking cortical neurons with 1000000 synaptic connections using only a 1GHz desktop PC and C++. The model is able to replicate known types of cortical states like alpha and gamma oscillations. Other known oscillations of the cortex, like sleep oscillations or spindle waves can be produced by changing the synaptic strength and the thalamic drive of the model (Izhikevich et al., 2003; Izhikevich and Edelman, 2008).

Izhikevich model uses only two differential equations with its reset conditions to sim-

ulate spiking neurons. Four parameters are used to generate different firing patterns. Despite a nonlinear term $V^2(t)$ in equtaion (2.35), the computational efficiency is not demanding, which makes it a valuable model to replicate the large scale of neurons' behaviour to exhibit the oscillations and rhythms of neuronal population.

2.7.4 Cortical network model

A simulated spike train dataset used in this project was generated using a network of simulated cortical neurons based on the point-neuron model taking into account a conductance formulation used in neural model descriptions (Troyer and Miller, 1997). The cortical neuronal network model is a reduced Hodgkin-Huxley model which includes simplified conductance based synaptic inputs instead of the dynamical ionic currents. It is also can be seen as a conductance-based LIF model since the synaptic inputs are related with variation of the conductance.

In the point cortical neuron model, the intracellular membrane potential for each cell is given as (Halliday, 2005):

$$C_m \frac{dV_m}{dt} = -I_{leak}(V_m) - \sum_{j=1}^{n} I_{syn}^{j}(V_m, t) \tag{2.39}$$

in conjunction with a partial reset mechanism, where V_m denotes the membrane potential at time t and C_m denotes the cell capacitance.

I_{leak} represents the passive leakage current and $I_{syn}^{j}(V_m, t)$ the synaptic inputs due to the jth presynaptic spike. n. The summation is conducted over the total number of presynaptic spike, n. The leakage current I_{leak} is given as:

$$I_{leak}(V_m) = (V_m - V_r)/R_m \tag{2.40}$$

where V_r is the cell resting potential and R_m is the cell input resistance. According to (Troyer and Miller, 1997), The values of these parameters are set as: $R_m = 40M\Omega$, $C = 0.5pF$, and $V_r = -74mV$ (Halliday, 2005).

The partial reset mechanism associated with point cortical neuron model is governed by two parameters, namely V_{thresh} and V_{reset}, with V_{thresh} denoting a fixed firing threshold and V_{reset} denoting a fixed reset value. The partial reset mechanism suggests that the cell will fire a output spike when V_m exceeds V_{thresh}, after which the membrane potential V_m will reset to V_{reset} immediately. The values of these parameters are $V_{thresh} = -54mV$ and $V_{reset} = -60mV$ (Halliday, 2005).

Time-dependent conductance, $g_{syn}(t)$ and the equilibrium potential for the ionic current, V_{syn} are the two parameters used to specify the synaptic current $Isyn(V_m, t)$. The conductance $g_{syn}(t)$ is related to the opening of ionic channels follow neurotransmitter release, modelled as:

$$g_{syn}(t) = G_{syn}/\tau_{syn} exp(-t/\tau_{syn}) \tag{2.41}$$

.

where G_{syn} is the conductance scaling factor and τ_{syn} is the time constant. For excitatory inputs and inhibitory inputs, the corresponding G_{syn} and τ_{syn} are usually different.

The synaptic current due to a single presynaptic spike at $t = 0$ is given as:

$$I_{syn}(V_m, t) = g_{syn}(t)(V_m - V_{syn}) \tag{2.42}$$

.

with each presynaptic input contributes one term in the summation $\sum_{j=1}^{n} I_{syn}^{j}(V_m, t)$ of equation (2.39), which lasts for the duration of the $g_{syn}(t)$ for that input.

2.8 Multielectrode Array Signal and Spike Sorting

Multielectrode array (MEA) is a device with multiple electrodes serving as an interface connecting neurons to electronic circuity. It allows neuronal signals of multiple neurons being recorded simultaneously. It measures the electric potentials around each electrodes and signalises them.

Raw MEA signals consist of action potentials (spikes) and local field potential (LFP) signals. LFP is mainly due to synaptic mechanisms and has slower time course (Buzsáki et al., 2012). Spikes are a sharp peak significantly deviating from the mean waveform and therefore have a faster time course. Hence, LFPs have lower frequency components compared to spikes. They can thus be separated by lowpass filter and highpass filter. LFP signals are usually composed of frequency components lower than 1kHz while the frequency of spiking signals vary upto around 10 kHz (Quiroga et al., 2004).

The filtered spiking sequences may contain spikes generated by different neurons. Therefore, assigning spikes to the correct firing neurons is a concern. Spikes may differ in their temporal patterns. For example, Figure 2.20 shows three different types of spiking pattern: fast spiking, regular spiking and bursting. These temporal patterns may be the characteristics on which different spike trains can be distinguished.

Spike sorting refers to the grouping of spikes based on the similarity of their shapes given that each neuron generates spikes in an exclusive shape(Quiroga et al., 2004). Recent progress in unsupervised learning and clustering has led to development of higher performance spike sorting algorithms (Karkare et al., 2013; Kamboh and Mason, 2013). Figure 2.21 illustrates the typical steps in a spike sorting procedure (Rey et al., 2015). The raw signals are filtered to remove interference of LFPs prior to spike detection based on some amplitude threshold. After the spikes are detected, feature extraction procedures are conducted to reduce the dimensionality in the feature space. This step can improve the computational efficiency of the following steps and get rid

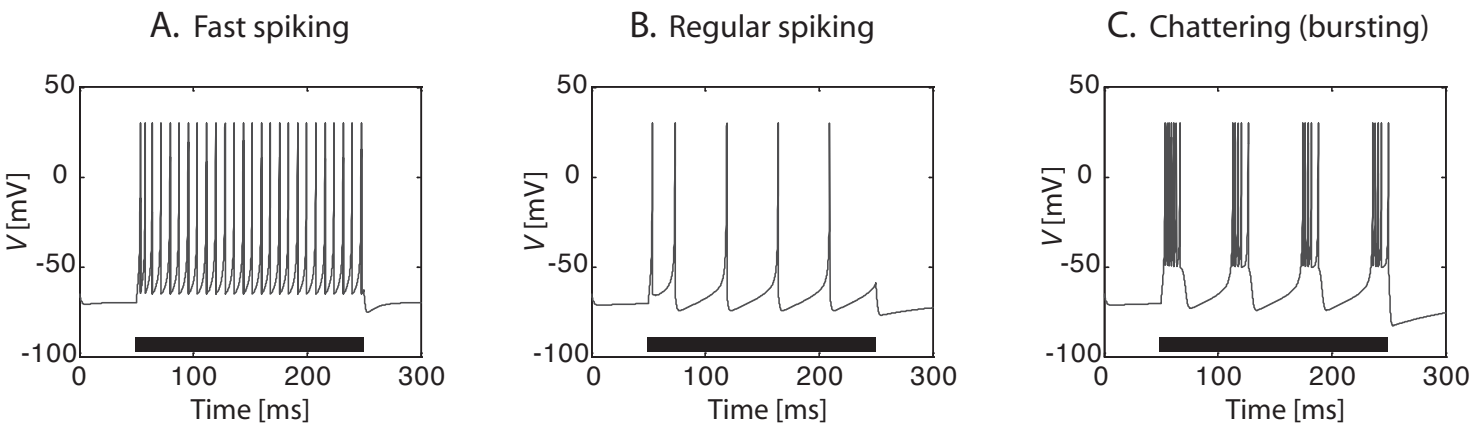

Figure 2.20: Different temporal patterns found in spiking sequences. Left panel: fast spiking; middle panel: regular spiking; right panel: bursting. Figure from (Trappenberg, 2010)

of dimensions which are dominated by noise. The next step is clustering which determines which spikes belong to which neuron. The spike sorting processing is essential to provide high quality spike train signals on which reliable analysis can be conducted.

2.9 Summary

Neurons in the central nervous system communicate with each other by receiving, generating and sending signals. This chapter briefly reviewed physiological and biological background of the central nervous system, especially at the levels of organisation and single cell. The signalling mechanism of neurons and between neurons have been described in detail. Spiking neuron models play an important role in understanding the dynamics of spike generating. They also provide tools to simulate the activities of real neurons and to generate simulated signals. Spiking neuron models have been reviewed in detail, including the Hodgkin-Huxley model, LIF model, Izhikevich model and point cortical model. The importance and the typical process of spike sorting have been discussed. Since the spike is the prototypic way in which neurons interact with each other, computational measurements to detect these interactions are important. The next chapter will discuss several techniques which can be applied to analyse neuronal interactions.

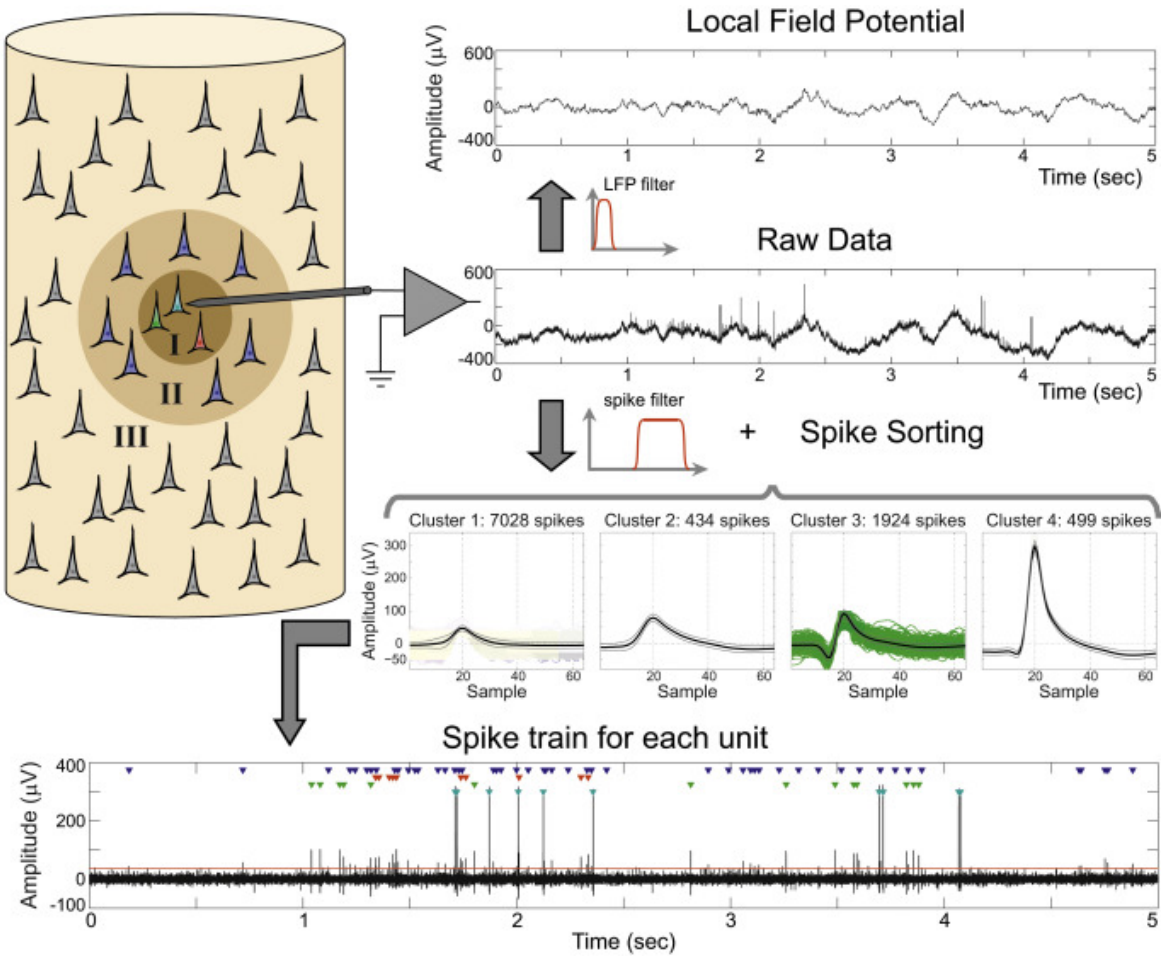

Figure 2.21: Step by step illustration of a typical spike sorting process. Figure from (Rey et al., 2015)

Chapter 3. A Survey of Some Statistical Signal Processing Methods

Contents

3.1 Introduction

The statistical dependencies carry important information on interactions between neurons. Hence, detecting the dependent pattern plays an essential role in understanding the functional connectivity in nervous system (Rubinov and Sporns, 2010; Biswal et al., 1995; Greicius et al., 2003). The solution to detect the dependencies requires a reliable measure to quantify the interaction between these neurons and ability to distinguish the moment when an interaction occurs. In neurophysiology, a wide range of experiments are carried out recording two or more signals simultaneously (Carracedo et al., 2013; Senik et al., 2013; Halliday et al., 1995). These records form continuous time series or point processes to which analysis techniques then can be applied to assess interdependence between signals.

This chapter first reviews techniques for the linear analysis between signals and discusses their advantages and disadvantages in sections 3.2 and 3.3. Afterwards, two

candidates, higher-order statistical methods and mutual information, which are potentially capable of revealing nonlinear interactions between signals will be explained in detail in sections 3.4 and 3.5.

3.2 The Correlation Function and Related Time Domain Techniques

The correlation function is one of the most classical methods of detecting interdependencies between two signals. This is a method relying on linear features. It measures the statistical dependency between two signals as a function of time.

General correlation is defined in classical statistical text (Wasserman, 2013; Neter et al., 1996; Metcalfe and Cowpertwait, 2009; Shumway and Stoffer, 2011). If X and Y are two random variables, how strong the linear relationship is can be measured by covariance and correlation between X and Y. The covariance is defined as a second order product moment, denoted as $Cov(X, Y)$:

$$Cov(X, Y) = E\{(X - \mu_X)(Y - \mu_Y)\} \tag{3.1}$$

where X and Y are two random variables with means μ_X and μ_Y and standard deviations σ_X and σ_Y. The correlation coefficient, denoted as $r(X, Y)$, is defined as the covariance of the two random variables divided by the product of their standard deviations:

$$r(X, Y) = \frac{Cov(X, Y)}{\delta_X \delta_Y} = \frac{E\{(X - \mu_X)(Y - \mu_Y)\}}{\delta_X \delta_Y} \tag{3.2}$$

so that the value of $r(X, Y)$ lies in the interval $[-1, 1]$.

Equation (3.1) can be expanded in a form:

$$Cov(X,Y) = E\{XY\} - E\{X\}E\{Y\} \tag{3.3}$$

and equation (3.3) shows that the covariance is quantified by the difference between the expectation of the product of these two random variables, $E\{XY\}$, and the product of expectations of these two random variables, $E\{X\}E\{Y\}$. If two random variables X and Y are not linearly related, $E\{XY\} = E\{X\}E\{Y\}$ holds, and the covariance $Cov(X,Y)$ is zero.

A time series can be treated as a collection of random variables indexed regarding the order they occurred. Therefore the correlation can be naturally introduced to operate on time series. If time series X_{t_k} and Y_{s_j} have means μ_{X_t} and μ_{Y_s}, the covariance function of these two time series can be defined as:

$$Cov(X_t, Y_s) = E\{(X_{t_k} - \mu_{X_t})(Y_{s_j} - \mu_{Y_s})\} \tag{3.4}$$

where set t_k is a representation of the orderly recorded time points with $k = 1, 2, ...$ and the definition of set s_j is similar.

Under the assumption that time series are wide-sense stationary, the means, μ_{X_t} and μ_{Y_s} are constants, denoted as μ_X and μ_Y respectively, and the the covariance depends only on the time difference between t and s rather than t and s themselves:

$$Cov_{XY}(\tau) = E\{(X_{t+\tau} - \mu_X)(Y_t - \mu_Y)\} \tag{3.5}$$

where τ is the time difference between the two time series. This measure can be estimated by:

$$\hat{Cov}_{XY}(\tau) = \frac{1}{N-\tau} \sum_{k=1}^{N-\tau} X(k+\tau)Y(k) \tag{3.6}$$

where N is the size of the observation dataset.

Since the cross correlation function is just the covariance normalised over the product of the standard deviations:

$$r_{XY}(\tau) = \frac{E\{(X_{t+\tau} - \mu_X)(Y_t - \mu_Y)\}}{\sigma_X \sigma_Y} \tag{3.7}$$

and given that the auto-covariance, $Cov_{XX}(\tau)$ or $Cov_{YY}(\tau)$, which is covariance in time series itself, will be simplified down to the variance of the time series when the time delay $\tau = 0$. Thus:

$$\sigma_X = \sqrt{Cov_{XX}(0)} \tag{3.8}$$

and

$$\sigma_Y = \sqrt{Cov_{YY}(0)} \tag{3.9}$$

Hence, the cross correlation function can be estimated by taking equations (3.6), (3.7), (3.8) and (3.9) into account:

$$\hat{r}_{XY}(\tau) = \frac{\hat{Cov}_{XY}(\tau)}{\sqrt{\hat{Cov}_{XX}(0)\hat{Cov}_{YY}(0)}} \tag{3.10}$$

The cross correlation function shows zero value if the two time series under consideration are not linearly correlated. On the other hand, if the absolute value of cross correlation function is 1, the two signals are entirely linearly related for the given time lag τ. The significant values of cross correlation function can be examined with the corresponding confidence interval. It suggests that the two signals taken into account have linear interaction when the significant values of cross correlation function are be-

yond the corresponding statistical confidence.

The spike train can be regarded as a realisation of stochastic point process, denoted by N. For this process N, the counts of events occurring within time interval $(0, t]$ is represented as $N(t)$. The differential increment is defined as $dN(t) = N(t, t + dt]$, which is the counts of events in a duration $(t, t + dt]$. In case of spike train, the value of each time point is either 1 or 0 depending on the occurrence of a spike or not. In the following text, different spike trains are represented by different subscripts, for instance, N_1 and N_2.

For spike train data, a suitable time domain measure similar to cross correlation function is the second order cumulant density (Bartlett, 1963; Conway et al., 1993), denoted as $q_{12}(u)$. In the case of point process N_n, its mean intensity, P_n, is defined as:

$$P_n = \lim_{dt \to 0} Prob\{An\ event\ in\ N_n\ in\ (t, t + dt]\}/dt \tag{3.11}$$

and could be interpreted in the form:

$$E\{dN_n(t)\} = P_n dt \tag{3.12}$$

due to its orderliness, where $E\{\}$ denotes the expectation operator.

In the case that two point processes, N_1 and N_2, are recorded simultaneously, the second order cross product density is defined at a specific temporal delay μ as:

$$\begin{aligned} P_{12}(u) = \lim_{du, dt \to 0} Prob(&An\ event\ in\ N_1\ in\ (t + u, t + u + du] \\ &and\ an\ event\ in\ N_2\ in\ (t, t + dt]/dudt \end{aligned} \tag{3.13}$$

and like the individual process case, the expectation form expresses the equation (3.13) in a way as:

$$E\{dN_1(t+\mu)dN_2(t)\} = P_{12}(u)dudt. \tag{3.14}$$

The second order cumulant density, $q_{12}(u)$, is then defined as:

$$q_{12}(u) = P_{12}(u) - P_1P_2 \tag{3.15}$$

Equation (3.15) infers that the second order cumulant density of pairwise point processes can be calculated as two independent processes's contribution being subtracted from the cross product density of these two processes.

3.3 Correlation in Frequency Domain: Coherence

Cross correlation function reveals linear correlation between two signals as a function of temporal lag in time domain. After the development of fast Fourier transform algorithm (Cooley and Tukey, 1965), it sheds light on the calculation of frequency domain measures for linear dependency detection. Coherence, as the frequency domain equivalent method of cross correlation, is also a widely used measure on dependency analysis (Benignus et al., 1969; Carter et al., 1973; Carter, 1987; Womelsdorf et al., 2007). In order to perform the coherence analysis, the spectral estimate techniques should be taken into account. This subsection will review the spectral and coherence estimation techniques.

Estimating the coherence requires spectral estimates being done in first place. From a statistical signal processing viewpoint, spectra can be treated as frequency parameters which have been systematically discussed in cases of time series data (Brillinger, 1981), point process data (Rosenberg et al., 1989; Bartlett, 1963) and hybrid data (Hal-

liday et al., 1995). In this subsection, the context of point process data will be highlighted.

Stationarity of point processes is assumed and both processes satisfy the mixing condition (Brillinger, 1981). A disjoint section method for the point processes can be found in some literatures. This method simplifies the expressions of confidence intervals for parameter estimates (Rosenberg et al., 1989; Halliday et al., 1995). The whole record, denoted by R, is subdivided into L non-overlapping disjoint epochs of equal length T, $R = LT$. Then finite Fourier transform can be applied to each segments. The finite Fourier transform of the l^{th} section $l = 1, 2, ..., L$ is defined as (Brillinger, 1972):

$$d_N^T(\lambda, l) = \int_{(l-1)T}^{lT} e^{-i\lambda t} dN(t) \approx \sum_{(l-1)T \leq \tau_j < lT} e^{-i\lambda \tau_j} \tag{3.16}$$

The approximately equal relationship in equation (3.16) is based on the spike train model, whose value is either 1 when a spike occurs or 0 when it is silent.

In the frequency domain, not only an informative measure is the cross spectrum itself, but it also is an essential intermediary parameter to coherence analysis. Cross spectrum is the Fourier transform of the second order cumulant density $q_{12}(u)$ (see section 3.2). Successively, the cross spectrum, denoted as $f_{12}(\lambda)$, between pairwise processes at frequency λ is the Fourier transform of its corresponding second order cumulant density, $q_{12}(u)$ (Bartlett, 1963):

$$f_{12}(\lambda) = \frac{1}{2\pi} \int_{-\infty}^{+\infty} q_{12}(u) e^{-i\lambda u} du \tag{3.17}$$

An alternative definition of cross spectrum uses empirical Fourier transform:

$$f_{12}(\lambda) = \lim_{T \to \infty} E\{d_{N_1}^T(\lambda) \overline{d_{N_2}^T(\lambda)}\} \tag{3.18}$$

whereas the auto spectrum of a individual point process can be defined by using the same subscript:

$$f_{11}(\lambda) = \lim_{T\to\infty} E\{d^T_{N_1}(\lambda)\overline{d^T_{N_1}(\lambda)}\} \tag{3.19}$$

where $d^T_{N_i}(\lambda)$ is the empirical Fourier transform of point process N_i and the overline represents complex conjugate. Equations (3.18) and (3.19) can be combined with the disjoint section method. The estimates of cross spectrum and auto spectrum straightforwardly approximate the limits of expectation by averaging over L subsection as:

$$\hat{f}_{12}(\lambda) = \frac{1}{2\pi LT}\sum_{l=1}^{L} d^T_{N_1}(\lambda)\overline{d^T_{N_2}(\lambda)} \tag{3.20}$$

$$\hat{f}_{11}(\lambda) = \frac{1}{2\pi LT}\sum_{l=1}^{L} d^T_{N_1}(\lambda)\overline{d^T_{N_1}(\lambda)} \tag{3.21}$$

The coherence, a frequency domain measure of linear dependency between two point process N_1 and N_2, is then defined as:

$$|R_{12}(\lambda)|^2 = \lim_{T\to\infty} |r_{12}\{d^T_{N_1}(\lambda), d^T_{N_2}(\lambda)\}|^2 \tag{3.22}$$

where r_{12} denotes the cross correlation (see section 3.2) between N_1 and N_2. This definition shows that coherence is the magnitude squared of cross correlation between finite Fourier transforms of N_1 and N_2. The cross correlation is scaled covariance, which means that the covariance is divided by the product of standard deviations of each point process:

$$r_{12}\{d^T_{N_1}(\lambda), d^T_{N_2}(\lambda)\} = \frac{Cov\{d^T_{N_1}(\lambda), d^T_{N_2}(\lambda)\}}{\sigma_{N_1}\sigma_{N_2}} \tag{3.23}$$

This leads to the definition of coherence as:

$$|R_{12}(\lambda)|^2 = \frac{|f_{12}(\lambda)|^2}{f_{11}(\lambda)f_{22}(\lambda)} \tag{3.24}$$

which can be estimated by directly substituting the corresponding spectra estimators as:

$$|\hat{R}_{12}(\lambda)|^2 = \frac{|\hat{f}_{12}(\lambda)|^2}{\hat{f}_{11}(\lambda)\hat{f}_{22}(\lambda)} \tag{3.25}$$

Because it is magnitude squared of cross correlation, coherence provide a quantity range within $[0, 1]$ to indicate the linear relationship, with 0 showing independence and 1 inferring entirely linear interaction (Rosenberg et al., 1989).

With the null hypothesis that the two point processes under examination are independent from each other, a upper boundary of significant interval of desired level α is given as (Brillinger, 1981; Rosenberg et al., 1989; Halliday et al., 1995):

$$CI_{upper} = 1 - (1 - \alpha)^{1/(L-1)} \tag{3.26}$$

For example, the 95% confidence interval is computed by substituting $\alpha = 0.95$ into the calculation. If two point processes taken into account have coherence within the range $[0, CI_{upper}]$, the null hypothesis is not rejected, they would be considered as linearly uncorrelated.

3.4 Higher Order Statistics

Although second order techniques reviewed in sections 3.2 and 3.3 are widely used, they may not be able to reveal dependencies and interactions beyond linearity.

Cross-correlation (and its variant, cross-correlation histogram (Perkel et al., 1967)) provides useful tools to detect the linear interactions and temporal delay between signals, however, they assume that both signals are Gaussian and they are not sensitive to nonlinear relationship. Additionally, they maybe loose information when applied to some small EPSPs with gently rise time (Searsl and Stagg, 1976). That is to say monosynaptic connections are not necessarily showed as a clear peak in cross-correlation because of the underestimation.

In order to deal with the potential non-linearity and increase the sensitivity of the weak synaptic interactions, a series of high order measurements have been developed in the past several decades. For example, joint peristimulus time scatter diagram (Gerstein and Perkel, 1972), normalised version of joint peristimulus time scatter diagram (Aertsen et al., 1989) and third order product density (Rosenberg et al., 1982).

Among these materials associated with different high order methods, a number of them introduced cumulants and discussed its properties (Brillinger, 1965).

For k random variables $(x_1, x_2, ..., x_k)$, the k-th order cumulant is defined in terms of its joint moments of order up to k. For the general purpose, it is denoted as $cum(x_1, x_2, ..., x_k)$ in this section, and is defined as (Brillinger, 1981; Mendel, 1991):

$$cum(x_1, x_2, ..., x_k) = \sum(-1)^{p-1}(p-1)!(E(\prod_{j\in I_1} x_j))...(E(\prod_{j\in I_p} x_j)) \qquad (3.27)$$

where the summation is done over all partitions $(I_1, I_2, ..., I_p)$, $p = 1, 2..., k$ and $E(\ )$ denotes the expectation operator (mean).

Take $k = 3$ as an example. For three random variables x_1, x_2 and x_3, table 3.1 illustrates the calculation of each moment term involved in the summation on the right-hand side of equation (3.27).

I_1	I_2	I_3	p	Moments Term
1	2	3	3	$(-1)^{(3-1)}(3-1)!E(x_1)E(x_2)E(x_3)$
1, 2	3		2	$(-1)^{(2-1)}(2-1)!E(x_1x_2)E(x_3)$
1, 3	2		2	$(-1)^{(2-1)}(2-1)!E(x_1x_3)E(x_2)$
2, 3	1		2	$(-1)^{(2-1)}(2-1)!E(x_1)E(x_2x_3)$
1, 2, 3			1	$(-1)^{(1-1)}(1-1)!E(x_1x_2x_3)$

Table 3.1: Moments terms of the cumulant when $k = 3$.

Hence, the third order cumulant of random variable x_1, x_2 and x_3 is simplified as:

$$\begin{aligned} cum(x_1, x_2, x_3) =& E(x_1x_2x_3) - E(x_1x_2)E(x_3) - E(x_1x_3)E(x_2) \\ & - E(x_2x_3)E(x_1) + 2E(x_1)E(x_2)E(x_3) \end{aligned} \tag{3.28}$$

Other order of cumulant can be calculated likewise.

Let $x_1(t)$, $x_2(t)$,..., $x_k(t)$ denote k stationary random processes, the cumulant of k-th order of the k processes,$C_k(\mu_1, \mu_2, ..., \mu_{k-1})$, is defined as the joint k-th order cumulant of the random variables $x_1(t)$, $x_2(t + \mu_1)$,...,$x_k(t + \mu_{k-1})$:

$$C_k(\mu_1, \mu_2, ..., \mu_{k-1}) = cum(x_1(t), x_2(t + \mu_1), ..., x_k(t + \mu_{k-1})) \tag{3.29}$$

Due to the stationariness of the random processes, the k-th order cumulant of the processes is a function of k-1 lags: μ_1, μ_2,..., μ_{k-1}. For the case $k = 3$, the third order cumulant $C_3(\mu_1, \mu_2)$ is given as:

$$\begin{aligned} C_3(\mu_1, \mu_2) =& E(x_1(t)x_2(t + \mu_1)x_3(t + \mu_2)) - E(x_1(t)x_2(t + \mu_1))E(x_3(t + \mu_2)) \\ & - E(x_1(t)x_3(t + \mu_2))E(x_2(t + \mu_1)) - E(x_2(t + \mu_1)x_3(t + \mu_2))E(x_1(t)) \\ & + 2E(x_1(t))E(x_2(t + \mu_1))E(x_3(t + \mu_2)) \end{aligned} \tag{3.30}$$

The cumulants have been applied on the case of ordinary time series and, especially, point process (Brillinger, 1972, 1975c, 1978). Some articles collected and reviewed several higher order statistics which are discussed in different papers associated with different topics. They highlighted the cumulant based methods' practical advantages comparing with moments statistics, and the enhancement of signal-to-noise ratio (Nikias and Raghuveer, 1987). The ability of coping with nonlinear processes was mentioned in these materials as well (Mendel, 1991).

3.5 Information Theory and Its Related Methods

The concept of information theory was introduced at the end of the 1940s (Shannon and Weaver, 1949). The concept of entropy, which has been originally seen in the literatures and materials about thermodynamics, was proposed in communication system by Claude Shannon, aiming at quantifying the amount of information in sources and channels. The synchronisation or interaction detecting between neurons can be regarded as a problem that needs a solution to establish the existence of common information between signals which are simultaneously recorded from neurons. Therefore, the inspiration of using information theory based methods is straightforwardly reasonable. Apart from that, neurons are nonlinear and adaptive, so the interactions between neurons intrinsically contain nonlinear components. Information theory based method is capable of detecting nonlinear interactions since it does not draw any assumptions of linearity on the signals and systems involved. Therefore, it has a promising potential coping with nonlinear correlations between signals comparing to coherence function of cross-spectral analysis. This subsection will discuss the information theory related measurements.

Information theory is closely related to the probability measure. Hence, it is of worth to review some concepts in probability theory. A discrete probability space $\Omega : (\Omega, (p_\omega)_{\omega\in\Omega})$ is an countable set Ω whose elements $\omega \in \Omega$ will be referred to as outcomes, associated with a non-negative real number p_ω assigned to each outcome ω such that $\sum_{\omega\in\Omega} p_\omega = 1$. p_ω is referred as the probability of the outcome ω. Then event

x is modelled by subsets x_Ω of the sample space Ω. The probability $p(x)$ of an event x is defined to be the quantity in the interval $[0, 1]$:

$$p(x) = \sum_{\omega \in x_\Omega} p_\omega \tag{3.31}$$

The joint probability $p(x, y)$ of x and y considers a joint event ensemble, xy, in which each outcome is an ordered pair x, y with $x \in x_\Omega$ and $y \in y_\Omega$. The marginal probability $p(x)$ from the joint probability $p(x, y)$ is obtained by summation:

$$p(x) = \sum_{y \in y_\Omega} p(x, y) \tag{3.32}$$

Similarly, the marginal probability of y is:

$$p(y) = \sum_{x \in x_\Omega} p(x, y) \tag{3.33}$$

The entropy is defined as a measurement of uncertainty. It is an average length of code in need to encode a random variable X whose sample space has M possible outcomes X_i, where $i = 1, 2, ..M$, and the probability of corresponding outcome is p_i. Based on this set of notation, the Shannon entropy of this random variable X is calculated as:

$$H(X) = -\sum_{i=1}^{M} p_i \log p_i \tag{3.34}$$

The unit of $H(X)$ depends on the base of logarithm, for example, if the base is 2, the unit of the entropy is bit (Shannon and Weaver, 1949). In the case of the continuous random variable, the concept is the same other than slight differences in format, integration over all possible X instead of sum up and probability density function, denoted as $\mu(x)$, instead of probability:

$$H(X) = -\int_{x \in X} dx \mu(x) \log \mu(x) \tag{3.35}$$

According to the equations (3.34) and (3.35), a straightforward attempt is to estimate the probability of each possible value, p_i or the probability density function, $\mu(x)$. A direct estimate of the probability is based on the normalised counts of each X_i (Strong et al., 1998; Kennel et al., 2005). The estimation begins by setting a window of length W. For the spike data whose resolution (or bin size) is $\Delta\tau$, a "word" has $W/\Delta\tau$ symbols. Let the count of ith "word" is denoted by c_i, so the normalised count of this "word", by the notation $\hat{p}_i$ is the count divided by the number of "words" the spike train contains, denoted by M. Then the estimator of the entropy, $\hat{H}(X)$, is:

$$\hat{H}(X) = -\sum_{i=1}^{M} \hat{p}_i \log \hat{p}_i \tag{3.36}$$

The concept of mutual information is defined as an extension of Shannon entropy by considering a pair of random variables X and Y. The mutual information quantifies how much information about one random variable is obtained by knowing the outcome of the other random variable. Therefore, in some materials, mutual information is also referred as "transinformation" (Eckhorn and Pöpel, 1974) or as "redundancy" (Panzeri et al., 1999). The mutual information between the two discrete random variables is calculated as:

$$I(X,Y) = \sum_{i=1}^{M_X} \sum_{j=1}^{M_Y} p_{ij} \log \frac{p_{ij}}{p_i p_j} \tag{3.37}$$

where p_{ij} is the joint probability of $X = X_i$ and $Y = Y_j$ and p_i is the probability of $X = X_i$ where $i = 1, 2, ..., M_X$ and, likewise, p_j is the probability of $Y = Y_j$ where $j = 1, 2, ..., M_Y$.

For two continuous variables X and Y, the mutual information between them is a quantity as:

$$I(X,Y) = \int \int_{x \in X, y \in Y} dxdy\mu(x,y) \log \frac{\mu(x,y)}{\mu(x)\mu(y)} \tag{3.38}$$

where $\mu(x, y)$ is the joint probability density of X and Y. The marginal densities of X and Y are respectively:

$$\mu_x(x) = \int_{y \in Y} dy \mu(x, y) \tag{3.39}$$

and

$$\mu_y(y) = \int_{x \in X} dx \mu(x, y) \tag{3.40}$$

An alternative to define mutual information usually can be found in references talking about detecting interaction between a input (stimulus) and output (response) (Borst and Theunissen, 1999; London et al., 2002; Kennel et al., 2005; Shlens et al., 2007). If X is regarded as the input (stimulus) and Y is regarded as response, Y's information entropy would be $H(Y)$, whereas $H(Y|X)$ would be the conditional entropy of Y given X. The mutual information would then be the reduced part of the uncertainty of the output because of the information of the input, which is literally in coincidence of its name "redundancy":

$$I(X, Y) = H(Y) - H(Y|X) \tag{3.41}$$

Mutual information shows value zero when the two random variables are independent, which can be easily derived from equation (3.37) or (3.38) because $p_{ij} = p_i p_j$ or $\mu(x, y) = \mu(x)\mu(y)$ makes the logarithm in these equations equal to zero. If there is a dependence between the two random variables, the mutual information will be a positive value. In an extreme case, this measure will achieve its maximum value, $H(X)(= H(Y))$, if the two signals are identical. Apart from that property, mutual information is a symmetric measurement (see figure 3.1), so it also can be achieved as:

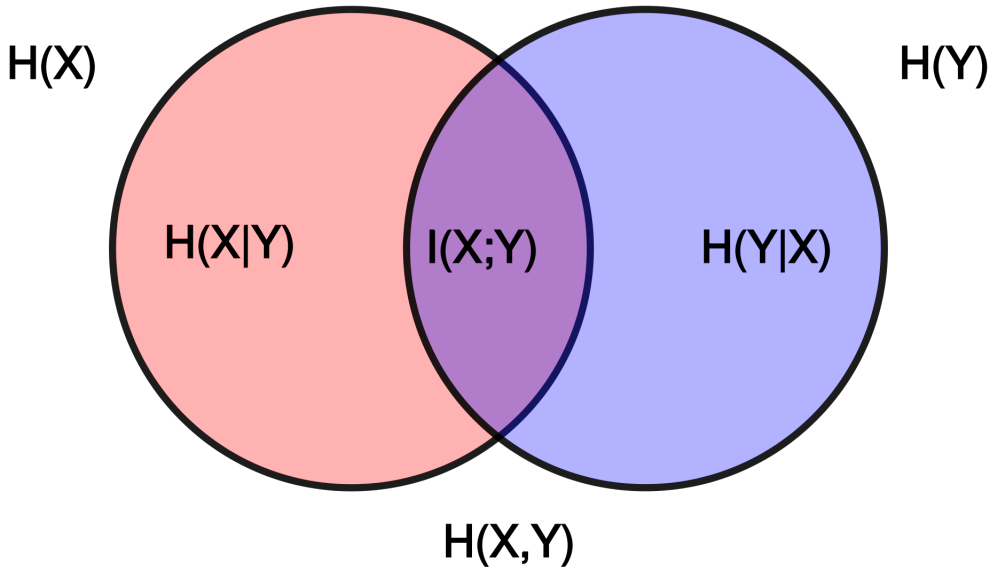

Figure 3.1: A Venn diagram shows various information measures associated with correlated variables X and Y. The area contained by both circles is the joint entropy $H(X,Y)$. The circle on the left (red and violet) is the individual entropy $H(X)$, with the red being the conditional entropy $H(X|Y)$. The circle on the right (blue and violet) is $H(Y)$, with the blue being $H(Y|X)$. The violet is the mutual information $I(X,Y)$. (figure from $https://en.wikipedia.org/wiki/Mutual\_information$)

$$I(Y,X) = H(X) - H(X|Y) = I(X,Y) = H(Y) - H(Y|X) \tag{3.42}$$

Hence it provide no information about the direction.

The mutual information is a straightforward measure. However, the estimation of it can be a difficult problem. Similar to the case of estimation Shannon entropy, a direct estimator of the probability is the histogram-based method, thus, every probability can be obtained by a partition of the corresponding variable, and a finite sum is used to approximate equations (3.37) and (3.38).

$$\hat{I}(X,Y) = \sum_{ij} \hat{p}_{ij} \log \frac{\hat{p}_{ij}}{\hat{p}_i \hat{p}_j} \tag{3.43}$$

where

$$\hat{p}_i = \int_i dx \mu_x(x) \tag{3.44}$$

$$\hat{p}_j = \int_j dy \mu_y(y) \tag{3.45}$$

and

$$\hat{p}_{ij} = \int_i \int_j dx dy \mu(x,y) \tag{3.46}$$

and $\int_i$ means the integral over bin i. If $n_x(i)$ is the count of points falling into the ith bin of X, similarly $n_y(j)$ is the count of points falling into the jth bin of Y, and $n(i,j)$ is the number of points in their intersection, the integrals (3.44), (3.45) and (3.46) can be respectively estimated by $\hat{p}_i \approx n_x(i)/N$, $\hat{p}_j \approx n_y(j)/N$, and $\hat{p}_{ij} \approx n(i,j)/N$ with N indicating the number of all the samples.

This method suffers from the requirement of large number of samples and suitably

chosen size of bin width (Strong et al., 1998; Quiroga et al., 2002; Reinagel and Reid, 2000). Furthermore, sometimes under a chosen bin size, none of sample points would fall into the square unit of $X = X_i$ and $Y = Y_j$. However, some sample points might fall into the rest part of stripe of $X = X_i$ and $Y = Y_j$, which makes the joint probability p_{ij} happen to be value 0, while the marginal probability of p_i and p_j are not, which results in an underestimate of mutual information (Kraskov et al., 2004).

In order to overcome the problem of null joint probability, some modified estimator improved by introducing adaptive bin size (Darbellay et al., 1999). However, this sort of method is not capable of reducing the system error caused by approximating probability via finite frequency ratio, even introducing the correction terms (Grassberger, 1988; Steuer et al., 2002). Another measure is inspired by the k-th nearest neighbour distance estimator (Silverman, 1986; Kraskov et al., 2004) (see section 3.5). This measure vastly reduces the systematic error compared with previous estimator. It also provides a more accurate result when the dataset is small. Apart from those measures above, the kernel density method is also applied to estimate mutual information. In contrast of histogram based methods, it has advantages in a better mean square error of convergence to the real underlying density, in addition to that, the kernel shapes are not only rectangular (Moon et al., 1995a; Schraudolph, 2004).

Some other literatures shed light on a way using Bayesian method to estimate the information entropy of spike trains (Wolpert and Wolf, 1995; Kennel et al., 2005). A remarkable virtue of this estimator is that it avoids model selection problem, thus, it needs no heuristic decisions and free parameters. Sequentially, this estimator is used to estimate mutual information. Moreover, it provides a Bayesian confidence interval about this estimate using a numerical Monte Carlo method (Shlens et al., 2007) (Gamerman and Lopes, 2006).

3.5.1 Mutual Information based on k-th nearest neighbour statistics.

Suppose that there are two random variables X, Y and each one has n observations, denoted as $x_i,\ i = 1, 2, ..., n$ and $y_i,\ i = 1, 2, ..., n$. Let $Z = (X, Y)$ and hence $z_i = (x_i, y_i)$. Let the distance between x_i and x_j be defined as the norm: $d_{x_{i,j}} = ||x_i - x_j||$. In this thesis, the second order norm, which is Euclidean distance, is used:

$$d_{x_{i,j}} = \sqrt[2]{(x_i - x_j)^2} = |x_i - x_j| \tag{3.47}$$

and similar definition can be drawn on Y:

$$d_{y_{i,j}} = \sqrt[2]{(y_i^2 - y_j)^2} = |y_i - y_j| \tag{3.48}$$

and $z_{i,j}$ is defined as the bigger one of these two distances:

$$d_{z_{i,j}} = max\{d_{x_{i,j}}, d_{y_{i,j}}\} \tag{3.49}$$

where max{ } means the biggest value in the curly bracket.

For each point $z_i = (x_i, y_i)$, the distances from it to other points could be sorted ascendantly: $d_{z_{i,j1}} \leq d_{z_{i,j2}} \leq ... \leq d_{z_{i,jn}}$. Similar sorting can be conducted to $d_{x_{i,j}}$ and $d_{y_{i,j}}$. Let $\frac{\epsilon(i)}{2}$ denote the distance from z_i to its kth neighbour, $\frac{\epsilon_x(i)}{2}$ and $\frac{\epsilon_y(i)}{2}$ denote the distances $\frac{\epsilon(i)}{2}$ projected onto X and Y axes. According to the definition of $d_{z_{i,j}}$ (see equation (3.49)), $\epsilon(i) = \max\{\epsilon_x(i), \epsilon_y(i)\}$ (see the illustration in figure 3.2).

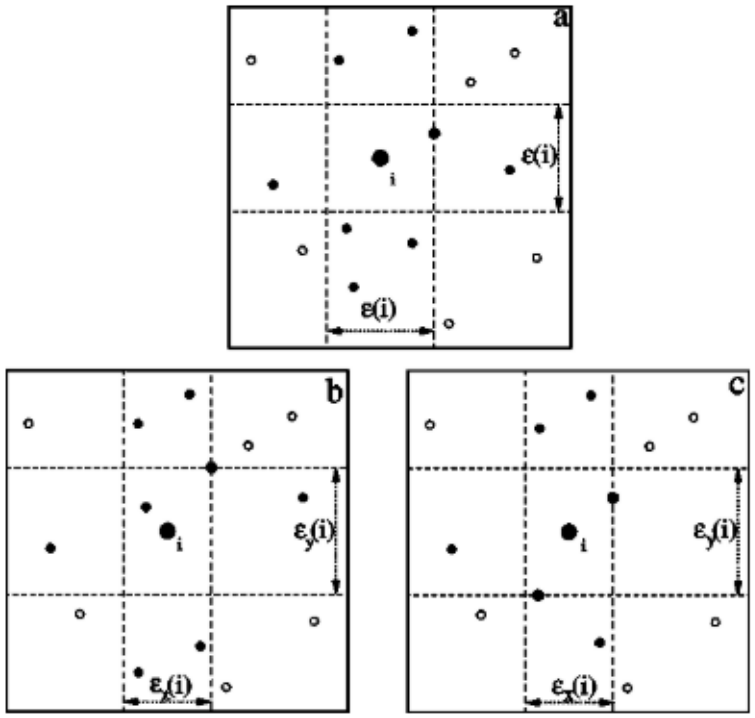

Figure 3.2: Representations of $\epsilon(i)$, $\epsilon_x(i)$ and $\epsilon_y(i)$, and the way to count the numbers $n_x(i)$ and $n_y(i)$. Plot (a) shows the determination of $\epsilon(i)$ when $k = 1$. Plots (b) and (c) show the determination of $\epsilon_x(i)$, $\epsilon_y(i)$, $n_x(i)$ and $n_y(i)$ when $k = 2$. The difference is that in case (b), $\epsilon_x(i)$ and $\epsilon_y(i)$ is determined by the same point, while in case (c), they are determined by different points. In both cases, $n_x(i) = 5$, and $n_y(i) = 3$. Figure from (Kraskov et al., 2004).

$n_x(i)$ denotes the number of points which have distances from the point x_i less than or equal to $\frac{\epsilon_x(i)}{2}$ (see figure 3.2 for the illustration):

$$n_x(i) = \text{counts}\{d_{x_{i,j}} \leq \frac{\epsilon_x(i)}{2}\} \tag{3.50}$$

and similarly for $n_y(i)$:

$$n_y(i) = \text{counts}\{d_{y_{i,j}} \leq \frac{\epsilon_y(i)}{2}\} \tag{3.51}$$

Then the estimator of MI is (Kraskov et al., 2004):

$$\hat{I}(X,Y) = \psi(k) - \frac{1}{k} - \frac{1}{n}\sum_{i=1}^{n}(\psi(n_x(i)) + \psi(n_y(i))) + \psi(n) \tag{3.52}$$

where $\psi(x)$ is the digamma function that satisfies the recursion (Abramowitz and Stegun, 1965):

$$\psi(x+1) = \psi(x) + \frac{1}{x} \tag{3.53}$$

with the initial condition $\psi(1) = -C$, where $C = 0.57721...$ is the Euler-Mascheroni constant.

To sum up, information theory based method is a suitable candidate for detecting interactions between neural spike trains. The problem to be solve for practical usage is finding a reliable estimator.

3.6 Summary

This chapter reviews several widely used statistical signal processing methods. The review starts with the most classical correlation coefficient and correlation function in time domain, followed by a description of the disjoint Fourier Transform, the estimation of spectra and the computation of coherence. The higher order statistics are also briefly discussed in this chapter, especially the calculation of higher order cumulants. The final part of this chapter covers Information theory and mutual information used in signal processing area. A mutual information estimation algorithm using k-th nearest neighbour statistics is discussed in detail. The techniques reviewed in this chapter lays the foundation of the development and implementation of the novel techniques proposed in future chapters.

Chapter 4. Third Order Time-Frequency Domain Analysis Framework

Contents

4.1 Introduction

This chapter aims at proposing a combined time and frequency domain framework and applying it to surrogate and experimental signals. It is important that measurements in both domains could be estimated independently and the transform from one domain to the other could be conducted.

An experimental dataset is used in this project. Hence, a brief description of the experiment which produces the data will be introduced in section 4.2. Then the Unified

framework of Third Order time and frequency domain analysis (UTO) for spike trains will be presented in section 4.3. Some results for artificial data and spike trains from a simulated neuronal network using point-cortical spiking model will be reported in section 4.4, along with a brief description of the configuration of this simulated network. Results for the analyses of experimental spike train signals will be discussed afterwards in section 4.5.

4.2 An Experimental Dataset of Spike Trains from Hippocampal recordings

An important dataset to which the techniques developed in this thesis will be applied is experimental hippocampal recordings from rat. The experiment studies the connectivity in a model of kainic acid (KA) induced epileptiform activity for mesial temporal lobe epilepsy (mTLE) in rat (Coomber et al., 2008; Senik et al., 2013). A multielectrode array (MEA) recording has been generated, following which the recording has been filtered and spike-sorted to form single unit spike trains signals. It is helpful to briefly review the experiment and provide an overview of the spike train dataset before undertaking detailed analyses.

4.2.1 A Brief Description of the Experiment

The time line of the experiment is divided into 3 phases. At the beginning, there was a period of 10 mins of basal recording which served as the baseline. Then Saline was injected intravenously in phase 2 10 mins after the basal recording. The third phase involved injection of 1mMol of KA after 30 min. Data of all three phases was recorded in a single recording with overall duration of 210 mins (Senik et al., 2013).

Phase	Experimental Protocol	Time t (min)
1	Basal Recording (Baseline)	$[0,\ 10)$
2	Saline Injection	$[20,\ 30)$
3	KA Injection and KA Effect	$[30,\ 210]$ (KA injected at 30 min)

Table 4.1: The procedure of the experiment protocol.

The single unit signals were recorded using 50 μm diameter stainless-steel electrodes as described in (Coomber et al., 2008). The recorded signals were then fed to Multichannel Acquisition Processor (MAP) system (Obeid et al., 2003) which is an integrated system with programmable signal amplification, filtering and real-time spike sorting of multichannel signals.

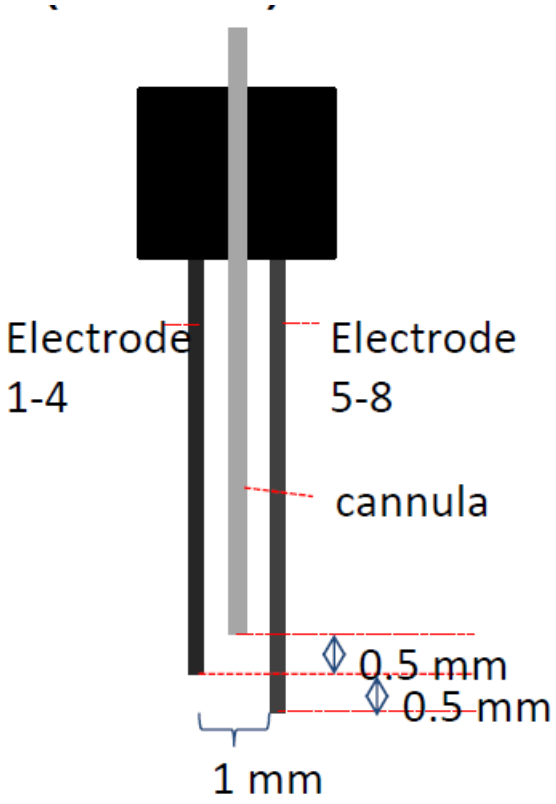

Figure 4.1: Schematic diagram of the electrode attached with cannula. There are 8 electrodes in two bundles of 4 to record from different regions. Figure from (Senik et al., 2013)

All procedures in this experiment were conducted in accordance with the animals (Sci-

entific Procedures) Act 1986, UK. In the experiment, isoflurane anaesthetised Lister-hooded rats (weight: $300 - 400\ g$; $n = 24$, where n is the number of experimental subjects) had MEA electrodes (see figure 4.1) positioned in the left and right hippocampus to simultaneous record multiple single-units and local field potentials. The electrode array used in the left hippocampus was attached by a cannula for the local injection of saline or kainic acid (see figure 4.2). Figure 4.3 shows an example of histological verification. Histological verification on the hippocampus revealed the electrodes positions via the Prussian Blue reaction generating blue dye marks (Taxidis et al., 2010). It is important to validate that recordings were made from the intended brain region (Senik et al., 2013).

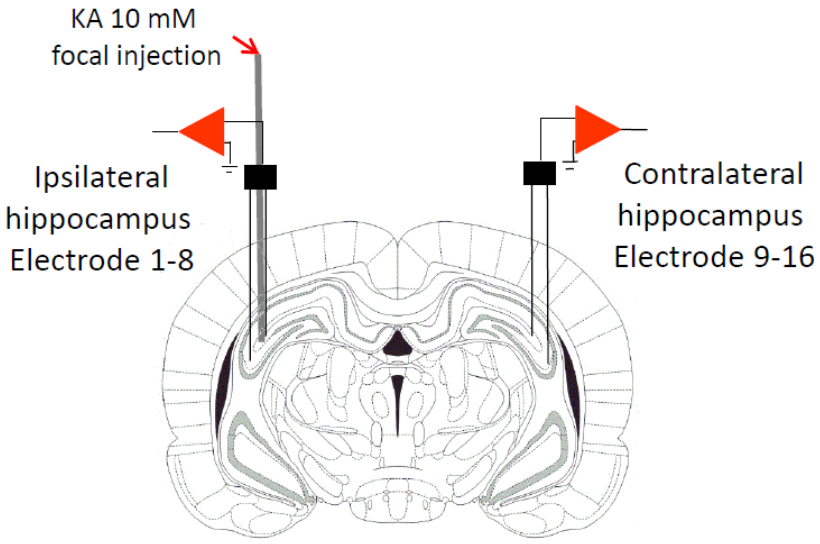

Figure 4.2: Schematic drawing of the electrode set-up position in the left and right hippocampus region. Figure from (Senik et al., 2013)

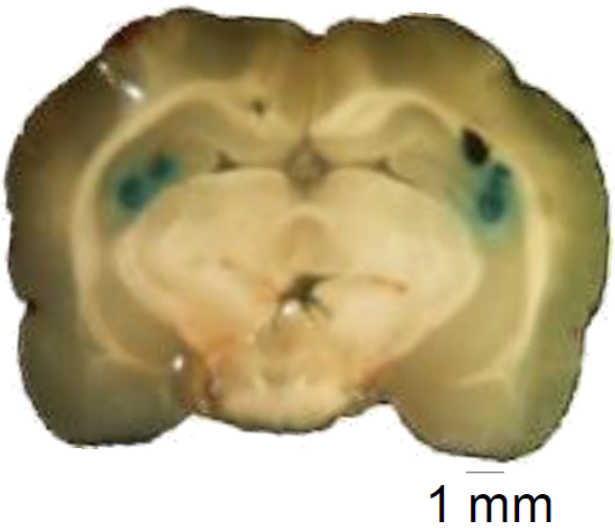

Figure 4.3: An example of histological verification revealing the electrodes positions by the visible blue dye marks. Figure from (Senik et al., 2013)

After the $210\ mins$ analogue multichannel signals were filtered to separate the spiking signals from the local field potentials, spikes sorting based on the similar neuronal spiking patterns was conducted off-line using off-line Sorter v3.23; Plexon Inc. The sorted signals consist of spike trains which are the recordings of the firing moments of each neuron. In the next subsection, the dataset used in this project will be briefly investigated through some basic statistics.

4.2.2 The Dataset

The experimental procedure is presented in section 4.2.1. Spike sorting generated the spike train signals. The signals used in this project are the first 5 minutes of the 210 minutes from the baseline phase of the experiment.

The data is record from four subregions in hippocampus of both hemisphere, namely left CA3, left CA1, right CA3 and right CA1. There are 18 channels of spike trains. The sample rate is $1\ ms$. Each spike train is of duration 300 seconds with different numbers of spikes. The information of subregions, recording nodes, signal indices,

signal names and Number of spikes are summarised in Tables 4.2 and 4.3.

The Interspike Intervals (ISI) is the time between subsequent spikes (Dayan and Abbott, 2001). Let the spike times of a spike train be denoted as $t(n), n = 1, 2, ..., N$ where N is the total number of spikes in this spike train. Hence, ISI, denoted as $\Delta t(n)$ is:

$$\Delta t(n) = t(n+1) - t(n) \tag{4.1}$$

where $n = 1, 2, ..., N-1$. The distributions of the ISI of each spike train are illustrated by non-normalised histogram in figure 4.4, 4.5 and 4.6. Almost all the 18 spike trains exhibit exponentially decaying interspike interval distributions, which means there tends to be more short waiting time between two spiking pulses (see section 4.4.1). These plots provide insights of intervals present in spike trains. The interspike interval distribution also plays an important role when artificial Poisson spike trains (see sections 4.4.1 and 5.2) are used as the example of independence between spike trains.

Subregion	Electrode	Signal Index	Signal Name	Number of Spikes
Left CA3	1	sig001a	sp1	5240
Left CA3	1	sig001b	sp2	1799
Left CA3	3	sig003a	sp3	1297
Left CA3	3	sig003b	sp4	521
Left CA3	4	sig004a	sp5	3333
Left CA3	5	sig005a	sp6	6900
Left CA3	5	sig005b	sp7	4626
Left CA1	6	sig006a	sp8	1898
Left CA1	7	sig007a	sp9	846
Left CA1	8	sig008a	sp10	6324
Left CA1	8	sig008b	sp11	1023
Left CA1	9	sig009a	sp12	658
Left CA1	10	sig010a	sp13	757
Right CA3	11	sig011a	sp14	2830
Right CA3	14	sig014a	sp15	138
Right CA3	14	sig014b	sp16	2279
Right CA1	15	sig015a	sp17	2689
Right CA1	16	sig016a	sp18	95

Table 4.2: Four different subregions of hippocampus with the corresponding nodes identification, signal indices, signal names and numbers of spikes being captured during the 5 minutes duration. (Simple statistical analysis in Table 4.3)

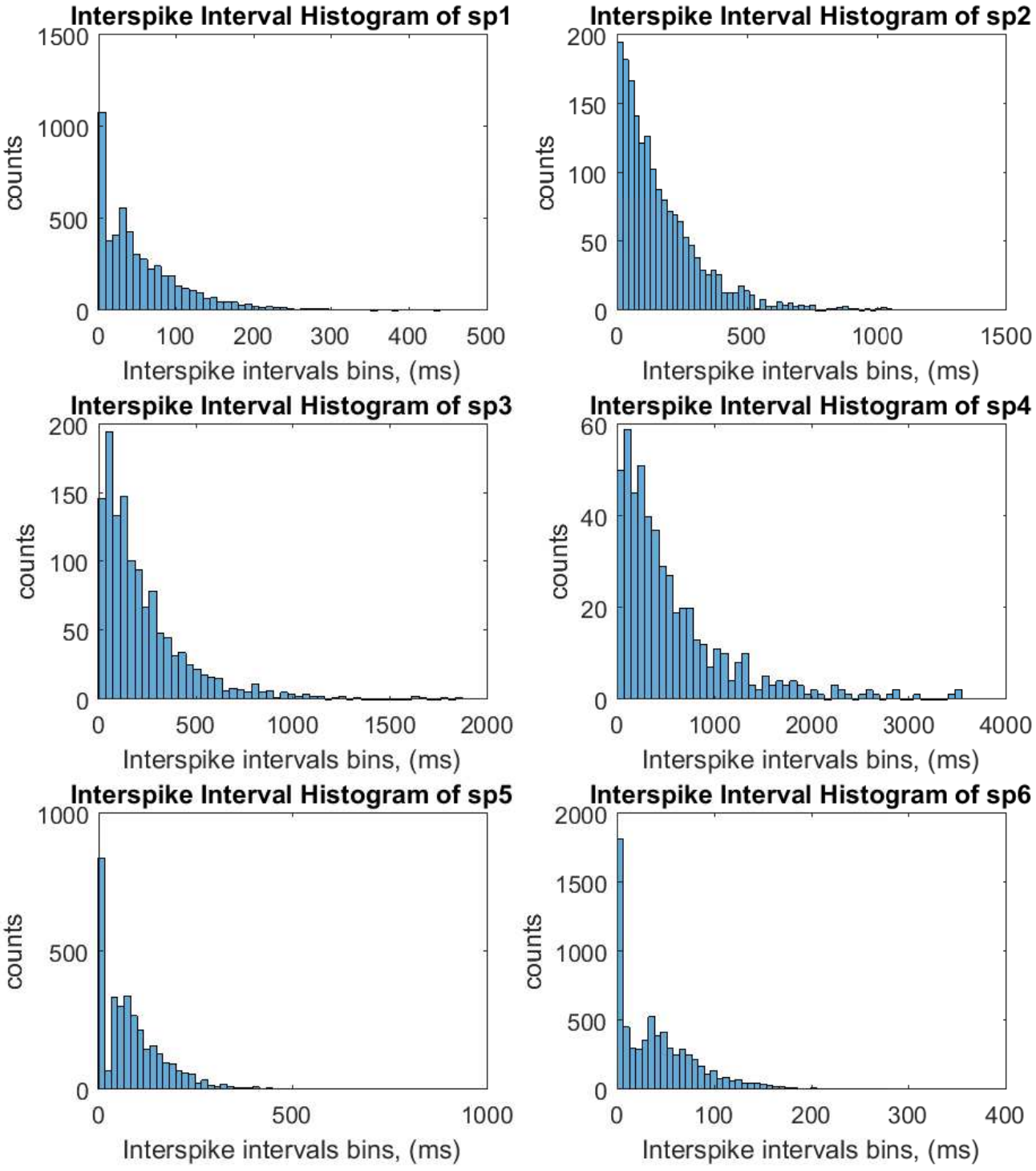

Figure 4.4: The Interspike Interval distributions of all spike trains in the hippocampal dataset. This figure illustrates the Interspike Interval distributions of sp1 $-$ 6 by the non-normalised histograms (counts in each bin) for each spike trains.

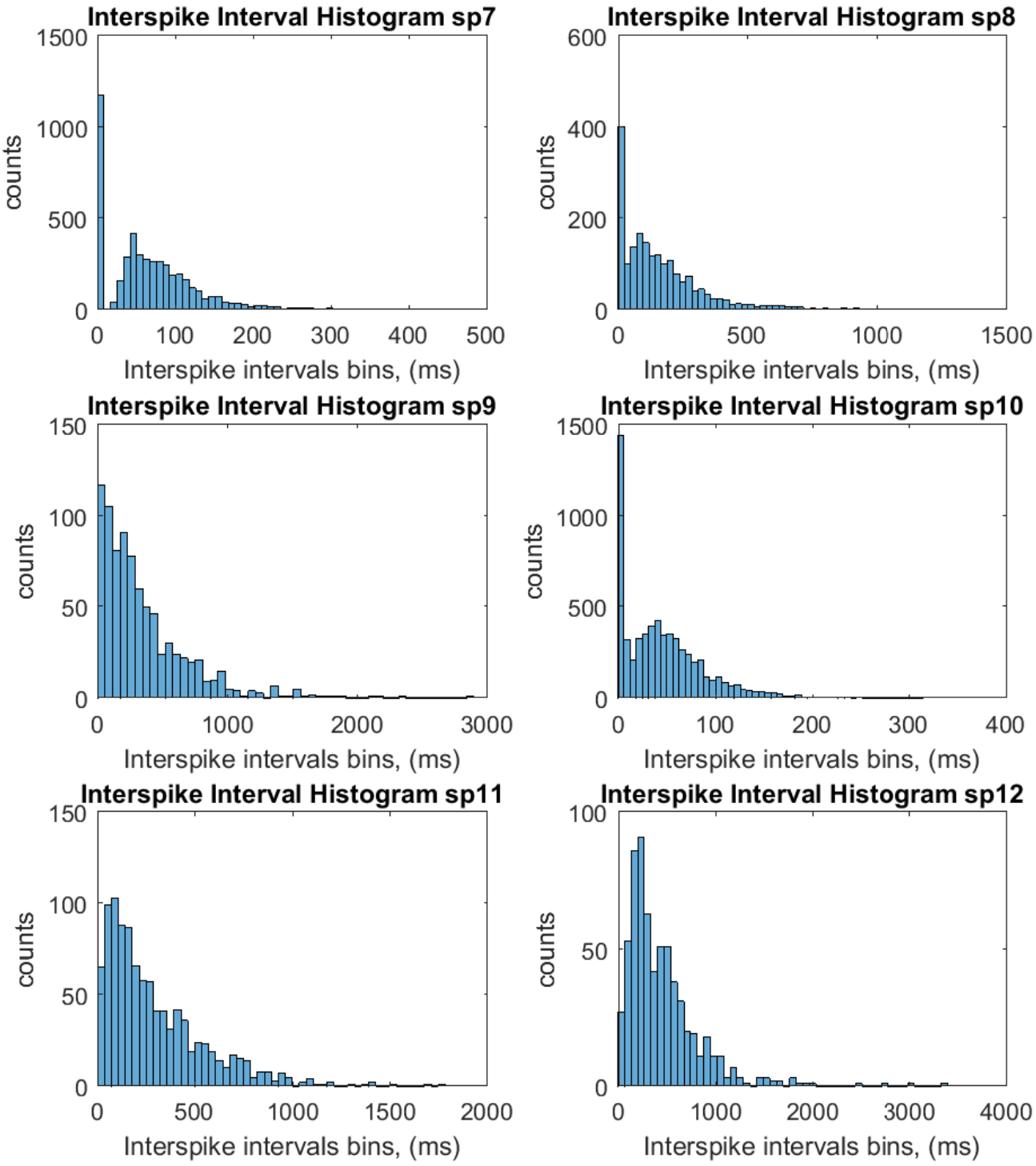

Figure 4.5: The Interspike Interval distributions of all spike trains in the hippocampal dataset. This figure illustrates the Interspike Interval distributions of sp7 $-$ 12 by the non-normalised histograms (counts in each bin) for each spike trains.

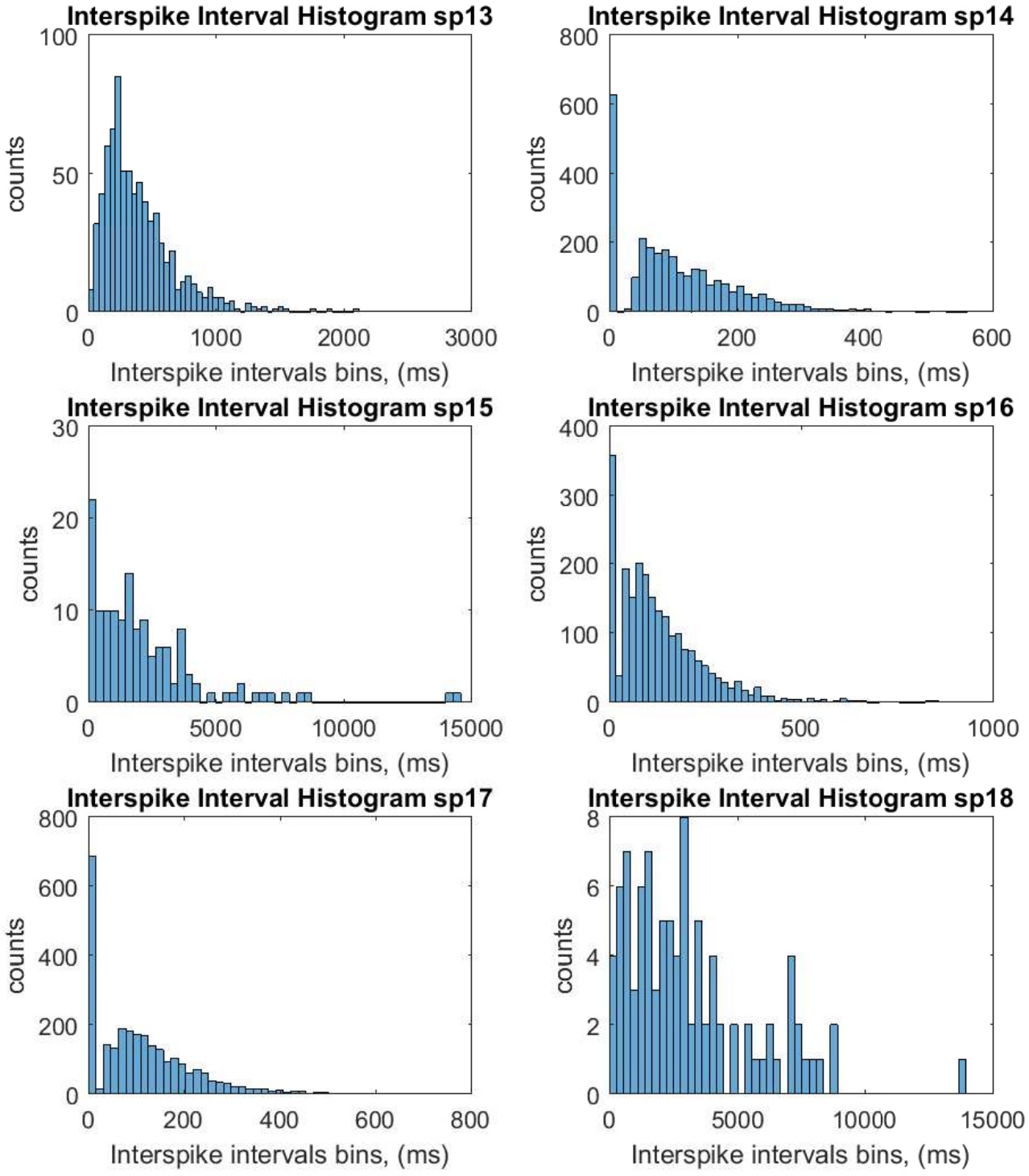

Figure 4.6: The Interspike Interval distributions of all spike trains in the hippocampal dataset. This figure illustrates the Interspike Interval distributions of sp$13 - 18$ by the non-normalised histograms (counts in each bin) for each spike trains.

Subregion	Signal	Firing Rate ($spikes/s$)	Mean ISI (ms)	STD ISI	COV
Left CA3	sp1	17.47	57.21	58.44	0.98
Left CA3	sp2	6.00	166.40	158.79	1.05
Left CA3	sp3	4.32	231.46	237.57	0.97
Left CA3	sp4	1.74	575.37	596.88	0.96
Left CA3	sp5	11.11	90.01	86.36	1.04
Left CA3	sp6	23.00	43.48	42.59	1.02
Left CA3	sp7	15.42	64.84	55.94	1.16
Left CA1	sp8	6.33	158.13	157.90	1.00
Left CA1	sp9	2.82	354.37	355.53	1.00
Left CA1	sp10	21.08	47.43	43.45	1.09
Left CA1	sp11	3.41	293.44	259.05	1.13
Left CA1	sp12	2.19	456.38	389.44	1.17
Left CA1	sp13	2.52	396.47	283.40	1.40
Right CA3	sp14	9.43	106.01	88.64	1.20
Right CA3	sp15	0.46	2170.06	2345.52	0.93
Right CA3	sp16	7.60	131.69	118.01	1.12
Right CA1	sp17	8.96	111.57	102.85	1.08
Right CA1	sp18	0.32	3154.85	2551.17	1.24

Table 4.3: Basic statistics of spike trains in hippocampal dataset, the columns represent the estimated firing rates, the ISI mean, the standard deviations of ISI and COV values.

The expectations and the standard deviations of the ISI are the first and second order statistics of the ISI: the ISI expectation (mean, μ_{ISI}) is the average of the time between two neighbour pulses in each spike trains and the ISI deviation (σ_{ISI}) is the extent to which the intervals fluctuates from its mean value:

$$\mu_{ISI} = \frac{1}{N-1}\sum_{n=1}^{N-1}\Delta t(n) = \frac{R}{N-1} \tag{4.2}$$

$$\sigma_{ISI} = \frac{1}{N-1}\sum_{n=1}^{N-1}(\Delta t(n) - \mu_{ISI})^2 \tag{4.3}$$

where R is the duration of the spike train.

The Coefficient Of Variation (COV) of a spike train is defined as the ratio of the ISI standard deviation to ISI mean:

$$COV = \frac{\sigma_{ISI}}{\mu_{ISI}} \tag{4.4}$$

The firing rate of a spike train, r_T, is estimated by averaging the total number of spikes N over the entire duration R:

$$r_T = \frac{N}{R} \tag{4.5}$$

Table 4.3 summarises the firing rate and basic statistics of the ISI of each spike trains. The firing rates of spike trains varies from less than $1\ spikes/s$ to above $20\ spikes/s$, as a consequence of the variation in the mean ISI from about $50\ ms$ to over $3000\ ms$. Each spike train has a standard deviation of ISI to its mean, thus, all the signals in this dataset have COV close to 1. This characteristic is approximately consistent with Poisson spike trains whose ISI have an exponential distribution (detailed discussion of Poisson spike trains seeing section 4.4.1). Some signals with few spikes have COV values different from 1, for example, sp13 and sp18. This feature provides the possibility that the artificially generated Poisson spike trains (see section 4.4.1) with the identical firing rates to the experimental spiking signals could potentially be used as the baseline when we calibrate the proposed methods.

4.3 The Unified Framework of Third Order Time and Frequency Domain Analysis

The cross-bispectrum, $f_{012}(\lambda, \mu)$ among three different spike trains N_0, N_1 and N_2 is defined as Brillinger (1975a):

$$f_{012}(\lambda,\mu) = \lim_{T\to\infty} \frac{1}{(2\pi)^2 T} E\{d^T_{N_0}(\lambda) d^T_{N_1}(\mu) \overline{d^T_{N_2}(\lambda+\mu)}\} \tag{4.6}$$

Where $d^T_{N_n}(\lambda),\ n = 0, 1, 2$ is the finite Fourier transform. This definition considers averaging the product of triplets of finite Fourier transforms at each frequency. Based on this consideration, the disjoint section method can be taken into account using an average over all segments. Hence, an estimate of cross bispectrum is calculated as:

$$\hat{f}_{012}(\lambda,\mu) = \frac{1}{(2\pi)^2 LT} \sum_{l=1}^{L} d^T_{N_0}(\lambda,l) d^T_{N_1}(\mu,l) \overline{d^T_{N_2}(\lambda+\mu,l)} \tag{4.7}$$

where T denotes the length of each disjoint segment, L denotes the number of segments, l indicates the index of segment, overbar represents complex conjugate and $d^T_N(\lambda,l)$ represents the finite Fourier transform of the disjoint segment l.

The equation (4.7) gives a direct way to interpret the sense of bispectrum. The third order cross spectrum quantifies the dependency among spike train N_0 at λ frequency, spike train N_1 at μ frequency and spike train N_2 at $(\lambda+\mu)$ frequency, since these three frequencies are required to sum up 0 (mod 2π) (Brillinger, 1975a).

As being presented in section 3.2, a spike train is essentially a recording of spikes' occurrence time in order. Under common circumstance, to form this kind of recording, it requires an appropriately small enough resolution (sample interval) to make sure that only one single spike can occur within a certain interval's length. That is to say, if the differential notation is introduced and let $N_1(t)$ indicate events existing over duration $(0,t]$ from spike train N_1, either 1 or 0 would be the value of $dN_1(t)$, where $dN_1(t) = N_1(t+dt) - N_1(t)$, according to the occurrence or not of a single spike.

In order to apply the third order cumulant density to the spike train datasets, there are two necessary assumptions which must be made. Firstly, the processes taken into account should be of second-order stationary. Apart from that, the mixing condition must hold (Brillinger, 1981). Furthermore, the orderliness discussed above ensure that the

expectation operation and probabilities interpretation can be applied to the calculation.

Suppose random processes N_0, N_1 and N_2 have mean rates P_0, P_1 and P_2 respectively. The third-order cumulant density is analytically defined as (Conway et al., 1993):

$$q_{012}(u,v)dudvdt = E\{(dN_0(t+u) - P_0du)(dN_1(t+v) - P_1dv)(dN_2(t) - P_2dt)\} \tag{4.8}$$

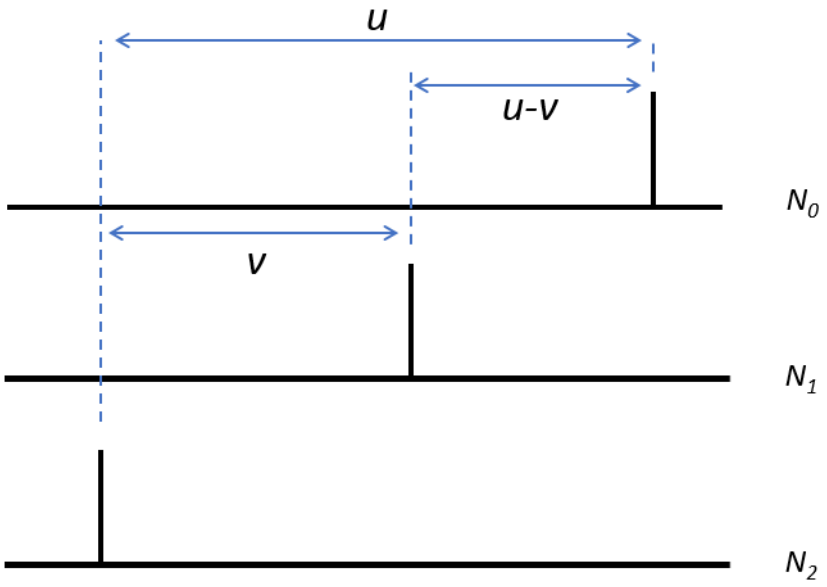

Figure 4.7: Schematic representation of the time convention used to represent the time intervals (lags) between spike trains.

This equation (4.8) can be expanded according to the expectation operator. Based on the definitions of product densities (Rosenberg et al., 1989), the third order product density of three spike trains is defined as:

$$\begin{aligned} P_{012}(u,v) =& Prob(An\ event\ in\ N_0\ in\ (t+u, t+u+du] \\ & and\ an\ event\ in\ N_1\ in\ (t+v, t+v+dv] \\ & and\ an\ event\ in\ N_2\ in\ (t, t+dt])/dudvdt \end{aligned} \tag{4.9}$$

The expectation version of this measure is:

$$P_{012}(u,v)dudvdt = E\{dN_0(t+u)dN_1(t+v)dN_2(t)\} \tag{4.10}$$

Similarly, the second order product densities alike is defined as:

$$\begin{aligned} P_{ab}(\alpha) =& Prob(An\ event\ in\ N_a\ in\ (t+\alpha, t+\alpha+d\alpha] \\ & and\ an\ event\ in\ N_b\ in\ (t, t+dt])/dtd\alpha \end{aligned} \tag{4.11}$$

where α is the distance between the two spikes investigated.

Expanding the terms in the expectation operator in equation (4.8) and applying the second- and third- order product densities defined above gives:

$$q_{012}(u,v) = P_{012}(u,v) - P_{01}(u-v)P_2 - P_{02}(u)P_1 - P_{12}(v)P_0 + 2P_0P_1P_2 \tag{4.12}$$

.

The form of equation (4.12) indicates a way to interpret the third order cumulant density measurement. Specifically, under a situation of specific distances u and v between three spikes, the first term on the right side of equation (4.12) is the third order product density. Then the contributions provided by pairwise linear interaction between two spike trains and a third independent one, which are represented by the second, third and forth terms on the right side, are subtracted. Afterwards, among these abandoned contributions, there is one scenario that this contribution could possibly result from three independent spike trains. From the equation (4.12), this sort of contribution has been redundantly removed two more times, so two times of this contribution, which is exactly the last term on the right, should be compensated back to the third order cumulant density measurement (Conway et al., 1993).

Since the expression of third order cumulant density has been achieved, the estimation can be obtained based on equation (4.12). The product density can be estimated by taking cross-correlation histogram as an intermediary (Brillinger, 1976; Brillinger et al., 1976; Melssen and Epping, 1987). Let a set $\{r_i\}$ represent the spike times of spike train N_0, where $i = 1, 2, ..., N_0(R)$. Similarly, sets $\{s_j\}$ and $\{t_k\}$ are defined for spike trains N_1 and N_2, for $j = 1, 2, ..., N_1(R)$ and $k = 1, 2, ..., N_2(R)$, respectively. R is the duration of the spike train signal.

The cross-correlation histogram of pairwise spike trains, for example, N_1 and N_2 may be expressed as:

$$J_{12}^{R}(v) = \text{counts}\{(s_j, t_k),\ v - \frac{b}{2} < s_j - t_k < v + \frac{b}{2}\ \ holds\} \tag{4.13}$$

where counts$\{S\}$ suggests the number of events in set S and b is the width of a bin centralised at lag v.

The second order product estimation is built upon the cross-correlation estimate (Brillinger, 1975b) as:

$$\hat{P}_{12}(v) = \frac{J_{12}^{R}(v)}{bR} \tag{4.14}$$

where b is the bin width.

This procedure can also be extended to the third order scenario. The third order correlation histogram is obtained as:

$$\begin{aligned} J_{012}^{R}(u, u-v) =& \text{counts}\{(r_i, s_j, t_k),\ u - \frac{b}{2} < r_i - t_k < u + \frac{b}{2}\ and \\ & u - v - \frac{b}{2} < r_i - s_j < u - v + \frac{b}{2}\ \ hold\} \end{aligned} \tag{4.15}$$

Successively, the unbiased third order product density estimate is as:

$$\hat{P}_{012}(u, u-v) = \frac{J^R_{012}(u, u-v)}{b^2 R} \tag{4.16}$$

where b is defined as the same as the second order case.

Finally, the mean rate of a spike train, for example, for N_0 can be estimated straightforwardly as:

$$\hat{P}_0 = N_0(R)/R \tag{4.17}$$

Throughout this procedure, all the terms on the right side of equation (4.12) are estimated, then the third order cumulant density estimator can be computed by substituting these terms into equation (4.12).

A reasonable 95% confidence interval has been derived as:

$$\hat{Var}[\hat{q}_{012}] = \hat{P}_0 \hat{P}_1 \hat{P}_2 / R b^2 \tag{4.18}$$

Then under the null hypothesis of independence, the 95% confident interval can be constructed as:

$$[0 - 1.96(\hat{P}_0 \hat{P}_1 \hat{P}_2 / R b^2)^{1/2}, 0 + 1.96(\hat{P}_0 \hat{P}_1 \hat{P}_2 / R b^2)^{1/2}] \tag{4.19}$$

(Rigas, 1983; Halliday, 2005).

The term forward transform refers to transform from temporal cumulant density q_{012} to cross-bispectrum f_{012} and the term backward transform refers to transform from cross-bispectrum f_{012} to temporal cumulant density q_{012}. These transforms need two dimensional Fourier transform and Inverse Fourier transform. The Forward-Backward

transform is summarised here (Yang and Halliday, 2018):

$$2\pi^2 f_{012}(\lambda,\mu) = \int_{-\infty}^{+\infty}\int_{-\infty}^{+\infty} e^{-i(\lambda u+\mu v)} q_{012}(u,v)dudv \tag{4.20}$$

$$q_{012}(u,v) = \int_{0}^{2\pi}\int_{0}^{2\pi} e^{i(u\lambda+v\mu)} f_{012}(\lambda,\mu)d\lambda d\mu \tag{4.21}$$

Equations (4.20) and (4.21) can be combined with frequency and time domain estimates described by equations (4.7) and (4.12), respectively, to construct the whole framework proposed together.

By contrasting equation (4.21) to equation (4.12) and all equations associated to (4.12), e.g. equations (4.13) - (4.17), the simplicity and conciseness of this combined framework have been achieved, which is the novelty we highlighted in this project. All calculation requirement of the lower order terms can be avoided due to the flexibility provided by this framework.

4.4 Third Order Analyses on Surrogate Data

The UTO analysis framework has been presented in section 4.3. The estimation methods proposed with the framework provide us tools to investigate associations and dependencies between spike train signals in third order, which is able to offer new insights into the relationships between spike trains.

The UTO analysis framework will be applied to surrogate data in this section: It will be applied to artificially generated spike trains in section 4.4.1. In section 4.4.2, it will be further used to analyse a simulated neural network using the point cortical model.

4.4.1 Third Order Analysis of Artificial Data

The data in this subsection were generated using different InterSpike Interval (ISI) distributions. The first case is three Poisson spike train. When the distribution of ISI has an exponentially decayed tail, this feature can be captured by the exponential distribution with the probability density function $p(x;\lambda)$ with a parameter λ:

$$p(x;\lambda) = \lambda e^{-\lambda x} \tag{4.22}$$

.

where the parameter $\lambda = \frac{1}{\mu_{Poi}} = \frac{1}{\sigma_{Poi}}$, with μ_{Poi} and σ_{Poi} denoting the mean and standard deviation of the exponentially distributed random variable. With the time between spikes exponentially distributed, the number of events n in time increment is given by the Poisson distribution with the probability density function $p(n;\lambda)$ (Trappenberg, 2010):

$$p(n = i;\lambda) = \lambda^i \frac{e^{-\lambda}}{i!} \tag{4.23}$$

and hence the spike trains are generated by using Poisson process (see figure 4.8).

In numerical computation, random numbers with an exponential distribution can be generated by taking the negative logarithm of uniformly distributed random numbers and then multiplying by a factor (the firing rate is used as this factor here) (Press et al., 1989). The firing rate used here is $22.46\ spikes/s$, which is randomly generated from the range of firing rates in the experimental dataset (see table 4.3). The three spike trains are generated in two configurations. The first configuration is three independent spike trains and the second configuration is three dependent spike trains with fixed delays between them.

The result of UTO analysis for the three independent Poisson spike trains are shown in figure 4.9. The estimates are obtained using the unified third order time-frequency do-

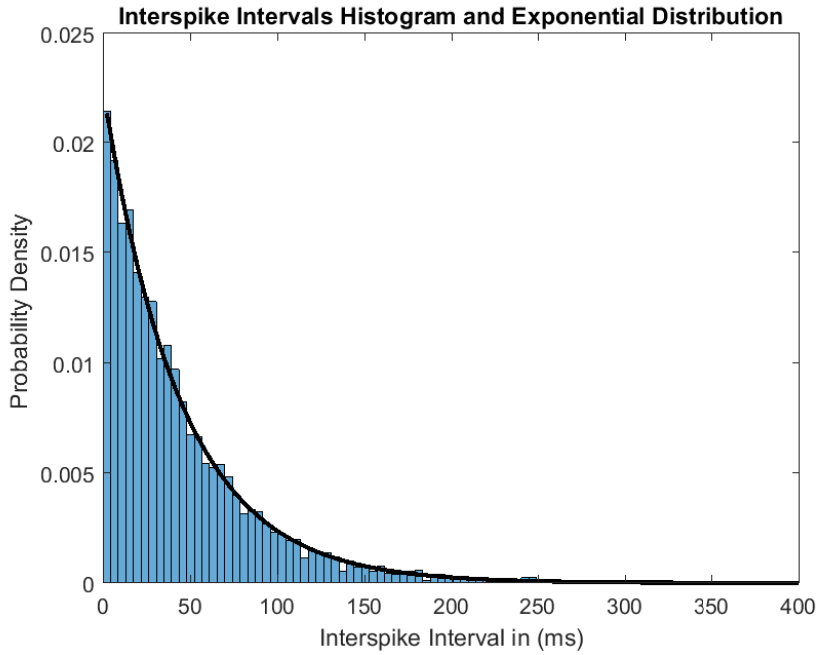

Normalised histogram and exponential distribution

Figure 4.8: The distribution of interspike intervals. The firing rate is 22.46 spikes/s. The figure shows the normalised histogram along with the probability density function of the exponential distribution (solid black curve) using the firing rate as the parameter λ , see equation (4.22).

main analysis framework (equations (4.7), (4.12), (4.18) - (4.21)). All the estimates illustrated as measures in frequency domain have been constructed using segment length $T = 1024$ and number of segments $L = 292$, and all the estimates illustrated as measures in time domain with the range of time lags $[0, 50]$ ms since the information transmission between neurons is usually with short latency.

In figure 4.9, logarithm auto spectra estimates are illustrated as a function of frequency in Hz, $log_{10}\hat{f}_{00}(\lambda)$, $log_{10}\hat{f}_{11}(\lambda)$ and $log_{10}\hat{f}_{22}(\lambda)$ respectively. All three auto spectra are bounded within the confidence intervals and oscillate randomly. There are no dominant features and all the values beyond the confidence limits are at single frequency components, which indicates that these outlying values are most likely beyond the confidence interval by chance. Due to the high COV value ($COV = 1$) of Poisson distributed interspike intervals, the auto spectra of all the three spike trains are lack of harmonic components in figure 4.9 (a), (b) and (c).

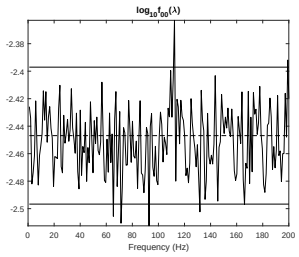

(a) Log spectrum of N_0

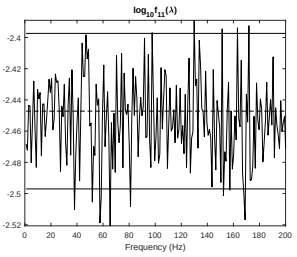

(b) Log spectrum of N_1

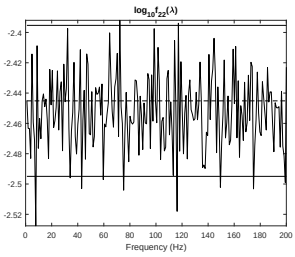

(c) Log spectrum of N_2

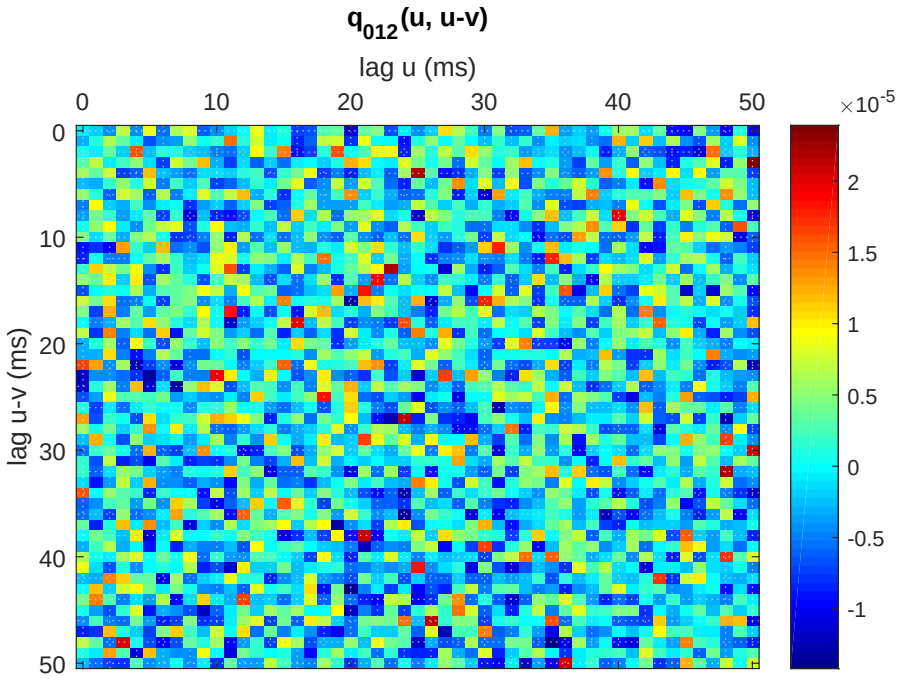

(d) Third order cumulant density

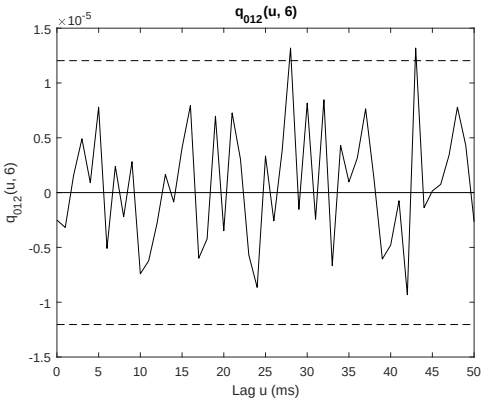

(e) A section of third order cumulant density

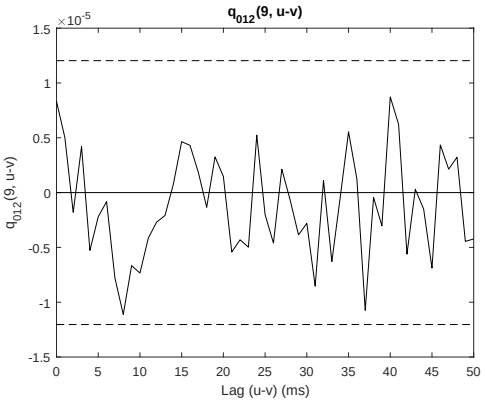

(f) A section of third order cumulant density

Figure 4.9: The top panel is the estimated log_{10} auto-spectrum of spike trains N_0, N_1 and N_2, respectively, (a) $log_{10}\hat{f}_{00}(\lambda)$, (b) $log_{10}\hat{f}_{11}(\lambda)$ and (c) $log_{10}\hat{f}_{22}(\lambda)$. The two solid lines represent upper and lower 95% confidence limits and the dashed line represents the mean. The middle panel (d) is the pixel image of estimated third order cumulant density, $q_{012}(u, u-v)$ with the colour bar on its right indicating the strengths of different colour. The bottom panel is plots of third order cumulant density at fixed time lags $u - v = 6\ ms$: $q_{012}(u, 6)$ and $u = 9\ ms$: $q_{012}(9, u - v)$ with the confidence limits.

In figure 4.9 (d), (e) and (f) are shown third order cumulant density estimates using UTO analysis, plotted over time lag range for 0 to $50ms$. The colour-coded graph (d) shows that the cumulants over all the lag pairs behave randomly. There are no areas of high cumulant values. Only scattered single pixels at the corresponding time lag pairs, which are formed by chance rather than indicating any dependence. This suggests the three spike trains under inspection are highly likely independent. The two sections of third order cumulant density at fixed time lags $u - v = 6\ ms$ (see figure 4.9 (e)) and $u = 9\ ms$ (see figure 4.9 (f)) further indicate the independence. Plot (e) is the third order cumulant density section through the lag $u - v = 6\ ms$ along u axis: $q_{012}(u, 6)$ and plot (f) is the third order cumulant density section through the lag $u = 9\ ms$ along $u - v$ axis: $q_{012}(9, u - v)$. These two plots are with confidence limits bounding almost all the estimated cumulant values within, which indicates the independence of the three Poisson spike trains. The confidence limits are constructed using the equations (4.18) and (4.19) based on the assumption that three Possion spike trains are independent.

The result for three delayed Poisson spike trains are shown in fig 4.10. The N_2 is generated as Poisson spike train with the firing rate $22.46\ spikes/second$. N_1 is generated by delaying N_2 by $18\ ms$. N_0 is generated by delaying N_2 by $40\ ms$. According to the time convention between spikes shown in figure 4.7, in this case, a single sharp peak is expected at the $(u, u - v) = (40, 40 - 18) = (40, 22)\ ms$.

In figure 4.10, logarithm auto spectra estimates of the three spike trains are illustrated on the top panel (see figure 4.10 (a), (b) and (c)). All these three spectral estimates fluctuates randomly without dominant features. Since N_0 and N_1 are obtained by just delay N_2, the shape of the three logarithm auto spectra are similar. In figure 4.10 (d), (e) and (f) are shown third order cumulant density estimates plotted over time lag range from 0 to $50\ ms$. The colour-coded graph (d) shows a significant pixel at the coordinate pair $(u, u-v) = (40, 22)\ ms$, which is consistent with the delaying configuration. The two sections of third order cumulants density at fixed time lags $u - v = 22\ ms$ (e) and $u = 40\ ms$ (f) illustrate a large sharp peak at $(40, 22)\ ms$, which successfully detects the dependencies and the delays.

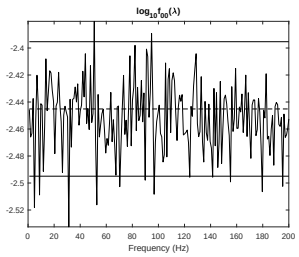

(a) Log spectrum of N_0

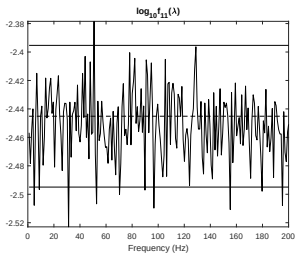

(b) Log spectrum of N_1

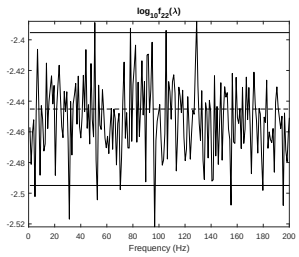

(c) Log spectrum of N_2

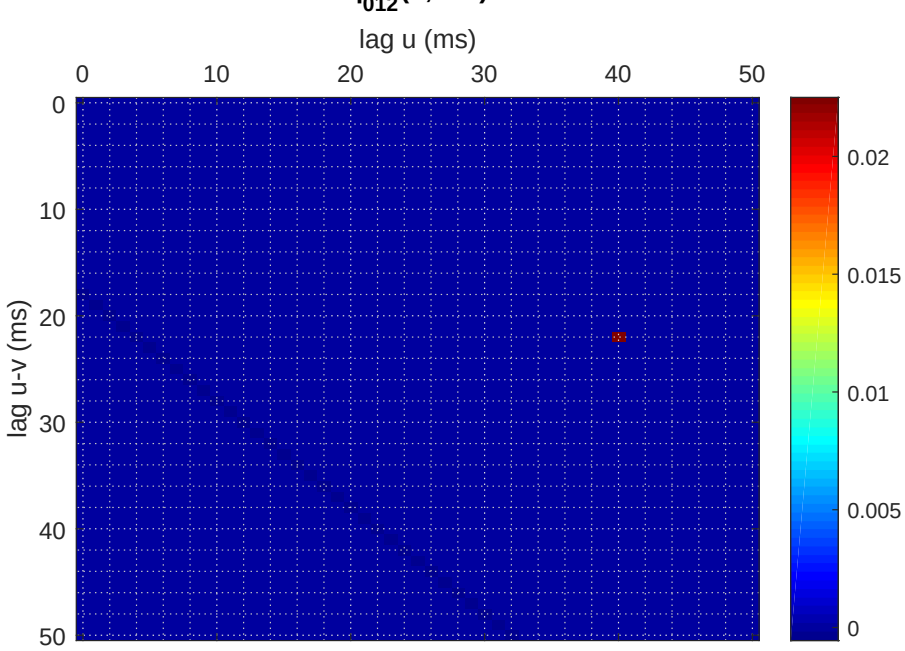

(d) Third order cumulant density

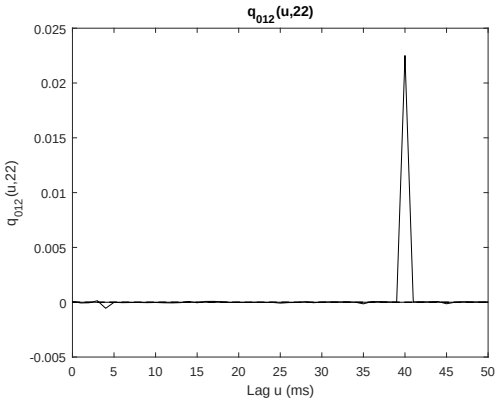

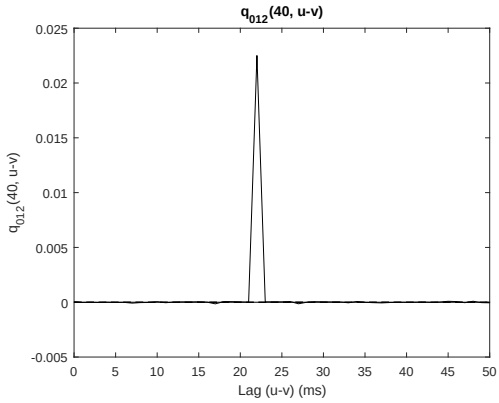

(e) A section of third order cumulant density(f) A section of third order cumulant density

Figure 4.10: The top panel is plots of estimated log_{10} auto-spectrum of spike trains N_0, N_1 and N_2, respectively, (a) $log_{10}\hat{f}_{00}(\lambda)$, (b) $log_{10}\hat{f}_{11}(\lambda)$ and (c) $log_{10}\hat{f}_{22}(\lambda)$. The two solid lines represent upper and lower 95% confidence limits, dash line represents the mean. The middle panel (d) is the pixel image of estimated third order cumulant density, $q_{012}(u, u-v)$ with the colour bar on its right indicating the strengths of different colour. The bottom panel is plots of third order cumulant density at fixed time lags $u - v = 22\ ms$: $q_{012}(u, 22)$ and $u = 40\ ms$: $q_{012}(40, u - v)$.

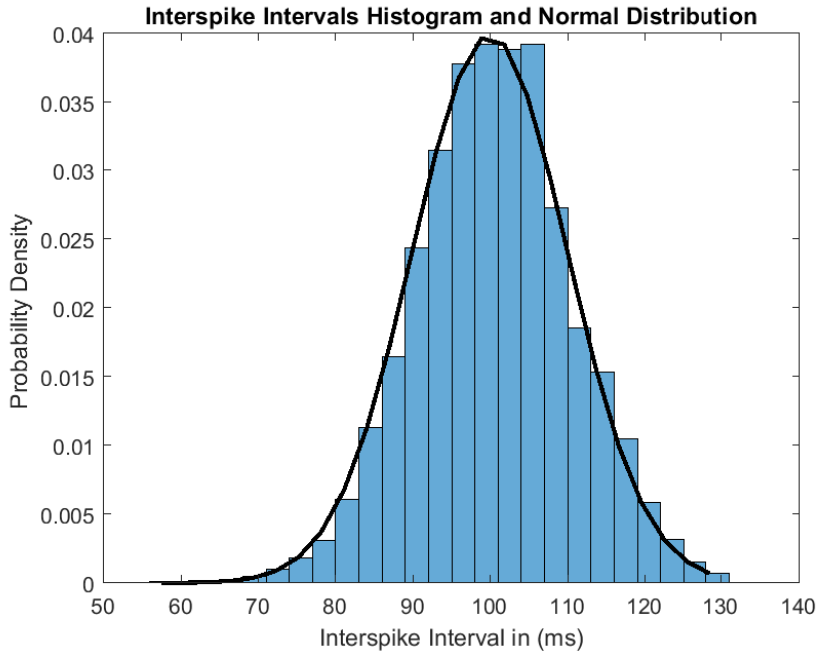

(b) Normalised histogram and Gaussian distribution

Figure 4.11: The distribution of interspike intervals. The firing rate is 10.30 spikes/second. The figure shows the normalised histogram along with the Gaussian distribution function (solid black curve).

Some spike trains recorded in experiments are found that their ISI are likely to be Gaussian distributed, for example, the motor unit recording in (Halliday et al., 1995). It is worth studying the dependence between Gaussian spike trains using UTO since the Gaussian model is able to represent the characteristics of some spike trains recorded in experiments. Figure 4.11 shows an example of artificial generated spike train with Gaussian distributed interspike intervals. The firing rate is $10.30\ spikes/s$ which is identical to the second motor unit spike train in (Halliday et al., 1995). The mean of ISI is about $100\ ms$ and the standard deviation of ISI is 10.

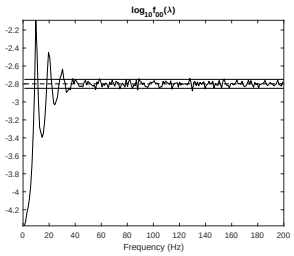

(a) Log spectrum of N_0

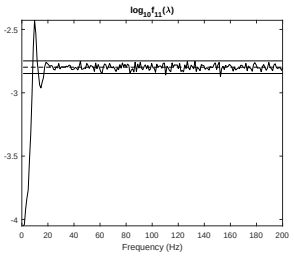

(b) Log spectrum of N_1

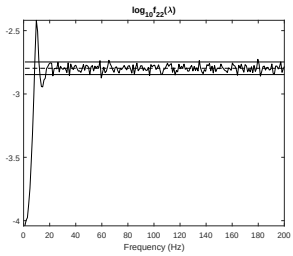

(c) Log spectrum of N_2

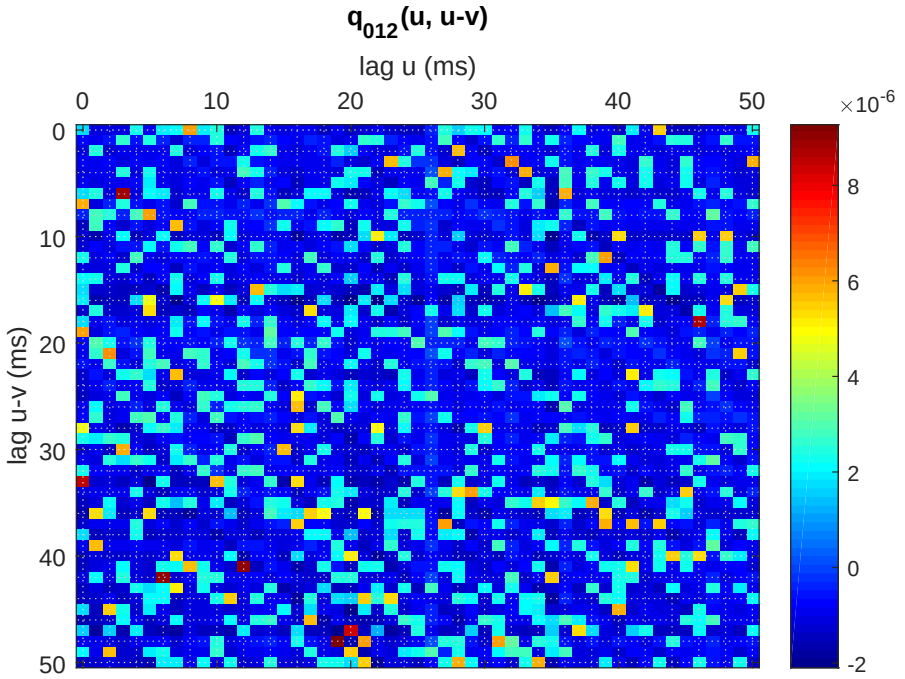

(d) Third order cumulant density

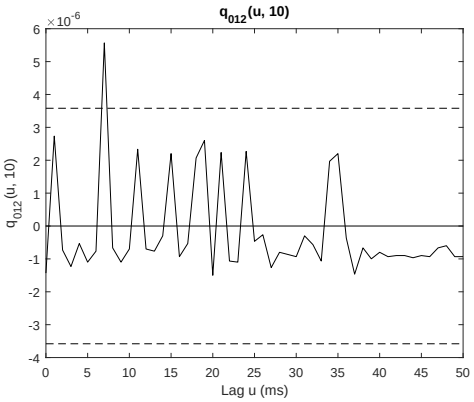

(e) A section of third order cumulant density

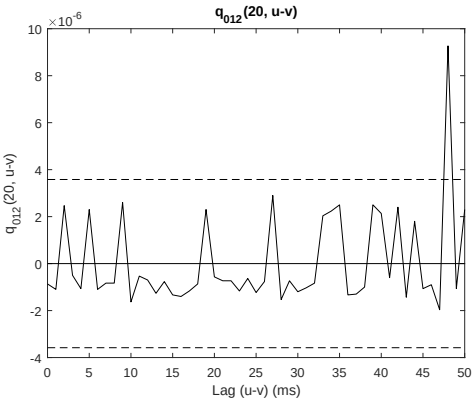

(f) A section of third order cumulant density

Figure 4.12: The top panel is plots of estimated log_{10} auto-spectrum of spike trains N_0, N_1 and N_2, respectively, (a) $log_{10}\hat{f}_{00}(\lambda)$, (b) $log_{10}\hat{f}_{11}(\lambda)$ and (c) $log_{10}\hat{f}_{22}(\lambda)$. The two solid lines represent upper and lower 95% confidence limits, dashed line represents the asymptotic value. The middle panel (d) is the pixel image of estimated third order cumulant density, $q_{012}(u, u-v)$ with the colour bar on its right indicating the strengths of different colour. The bottom panel is plots of third order cumulant density at fixed time lags $u - v = 10\ ms$ (e) and $u = 20\ ms$ (f) with the confidence limits and the asymptotic value.

The UTO analysis result for the three independent Gaussian spike trains with the same firing rate $10.30\ spikes/s$ are shown in fig 4.12. Spike train N_0 has $COV = 0.1$ and N_1 and N_2 have $COV = 0.2$. All the estimates in frequency domain have been constructed using segment length $T = 1024$ and number of segments $L = 292$, and all the estimates illustrated as measures in time domain have used the range of time lags $[0, 50]$ ms.

In figure 4.12, logarithm auto spectra estimates of the three Gaussian spike trains are illustrated on the top panel (see figure 4.12 (a), (b) and (c)). The asymptotic value shown as a dash line and confidence limits shown as two solid lines in each plots are estimated via assuming a random discharge with the same firing rates. All these three auto spectral share a dominant feature which is a significant peak near $10Hz$ in agreement with the firing rate of each spike trains, $10.30\ spikes/s$. Spike train N_0 has lower COV value ($COV = 0.1$) compared with N_1 and N_2 ($COV = 0.2$), therefore the estimated auto spectrum $log_{10}\hat{f}_{00}(\lambda)$ shows a more clear peak and oscillates more harmonically

In figure 4.12 (d), (e) and (f) are shown third order cumulant density estimates plotted over time lag range for 0 to $50ms$. The colour-coded graph (d) shows that the cumulants over all the lag pairs behave randomly. There are no areas of cumulant values but only scattered single pixels from random effects. The two sections of third order cumulants density at fixed time lags $u - v = 10\ ms$: $q_{012}(u, 10)$ (see figure 4.12(e)) and $u = 20\ ms$: $q_{012}(20, u - v)$ (see figure 4.12(f)) with confidence limits and asymptotic values indicate the well bounded values. The results are in agreement of the independence between the three Gaussian spike trains.

The UTO analysis framework has been verified by applying to some basic artificial configurations. The results obtained have shown that it is able to capturing the dependencies in these scenarios. This framework will be further applied to more complex configurations. In the next subsection, the UTO analysis framework will be used to analyse a simulated neural network using point cortical spiking neuron model (see

section 2.7.4).

4.4.2 Third Order Analysis on Simulated Network

The UTO analysis framework proposed in section 4.3 showed the ability to capture interactions between triplets of spikes in artificially generated spike trains in section 4.4.1. It is hence potentially a valuable tool to investigate dependencies in experimental spike train signals. The spiking neuron models discussed in section 2.7 simulate real biological signalling process and dynamics of neurons. Therefore, signals generated by simulated spiking neuron models have more resemblance to real neuronal signals compared with the generated ones based on the probability distributions in section 4.4.1. Applicability to these simulated signals could provide further verification of the proposed analysis framework.

This subsection presents the unified third order time-frequency domain analysis on the simulated spike trains which were generated using a cortical network model (see section 2.7.4). The simulated network and the signals will be briefly introduced, followed by the UTO analysis on the simulated spike train signals.

The network was constructed using the point-cortical neural model as described in section 2.7. The configuration was described in (Halliday, 2005) and the signals generated using this configuration were outputs of a C program. These signals are spike trains generated using a conductance-based synaptic integration model based on biophysical representation of cortical neurons. This kind of point neuron has conductance based formulation. Therefore, it will have nonlinear synaptic integration of inputs. Hence, third order effects may be exhibited in the simulated network. The signals received by each cell are from background inputs and from other cells in the same network. The background inputs consist of 100 excitatory inputs and 25 inhibitory inputs. Each input has an exponential interspike interval distribution triggered by a separate random spike train firing at $40\ spikes/s$. Excitatory populations thus provide 4000 EPSPs/s and Inhibitory populations provide 1000 IPSPs/s of background synaptic activation to

each cell. EPSP and IPSP synaptic conductances are modelled as an alpha function with the conductance scaling factor, G_{syn}, and the time constant, τ_{syn} (Rall, 1967; Halliday, 2005) as the parameters of the cortical network model (see equation (4.24)):

$$g_{syn}(t) = G_{syn}/\tau_{syn} exp(-t/\tau_{syn}) \tag{4.24}$$

.

There are 100 neurons in the network, arranged in a $(10*10)$ two dimensional grid (see figure 4.13 (a)). The ratio of excitatory to inhibitory neurons is 3 / 1 which is chosen to be consistent with the ratio reported in the cortex (Reeke et al., 2005). A centre-surround pattern which is essential in visual system is adopted for the connectivities within this network (see figure 4.13 (b) and (c)).The simulation generated 100 spike trains with duration 100 seconds. The configuration of this network is summarised in table 4.4.

Configurations	Network
Number of neurons	100
Topological structure	$10 * 10$
Excitatory neurons	75
Inhibitory neurons	25
E/I ration	3 / 1
Length of simulation	$100\ seconds$
Connectivity pattern	centre-surround

Table 4.4: Configuration summary of the simulated network.

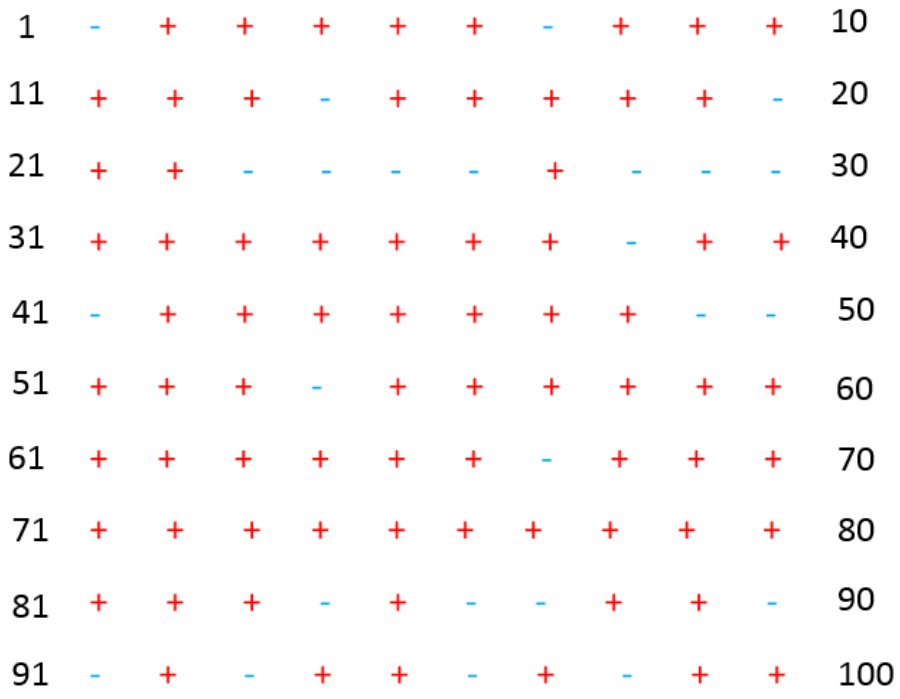

(a) Schematic plot of relative positions of excitatory neurons (red "+") and inhibitory neurons (blue "-").

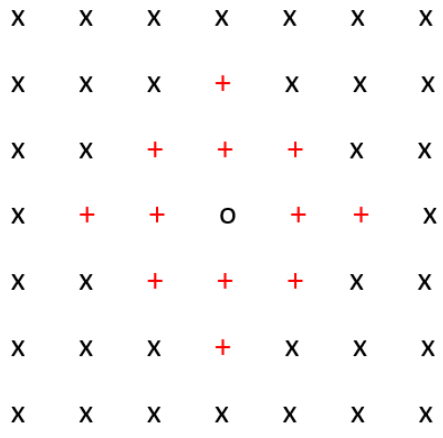

(b) Excitatory connectivities

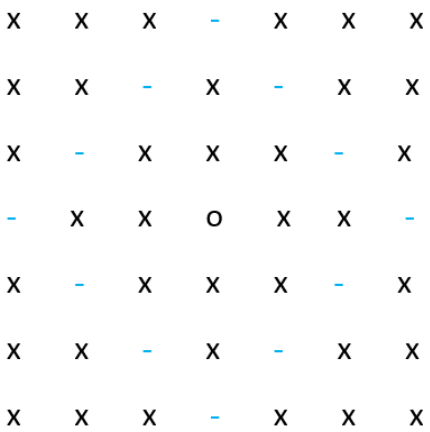

(c) Inhibitory connectivities

Figure 4.13: The top panel (a) is the schematic plot of relative positions of excitatory neurons (red '+') and inhibitory neurons (blue '-') in the $10 * 10$ 2-D sheet. The bottom panel is the schematic illustrations of centre-surround connectivities. In both subplots, black 'O' in the centre represents the presynaptic cell. In (b), red '+' illustrates postsynaptic neurons which receive excitatory inputs from the presynaptic neuron 'O'. In (c), blue '-' illustrates postsynaptic neurons which receive inhibitory inputs from the presynaptic neuron "O". The black 'X' in (b) and (c) represent the postsynaptic neurons which receive nothing from presynaptic neuron 'O'.

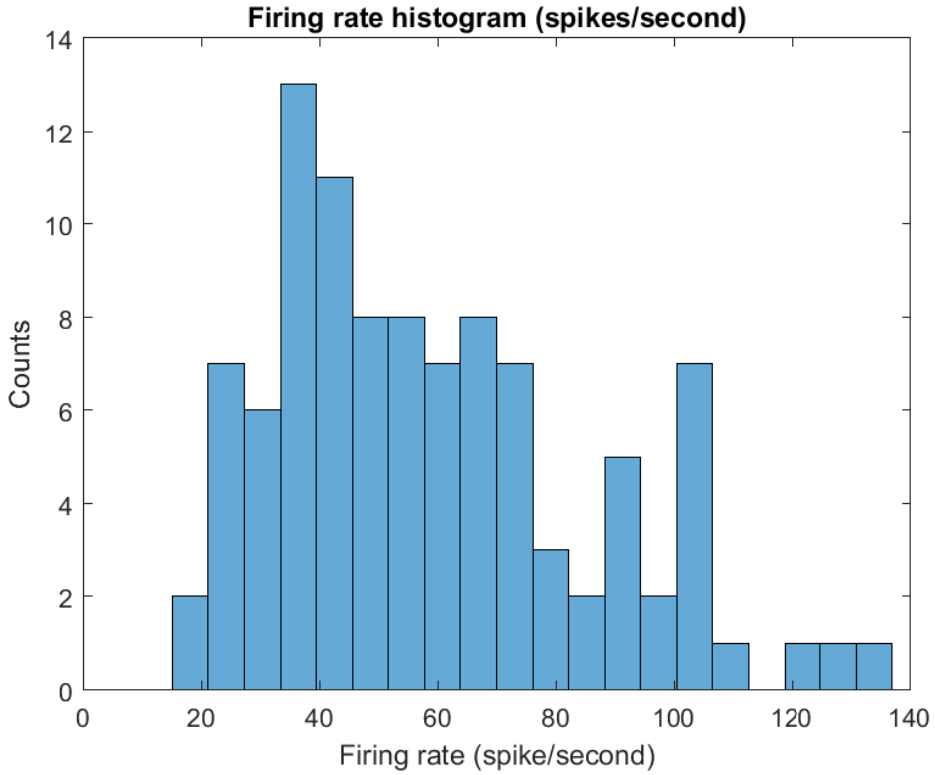

(a) Histogram of firing rate

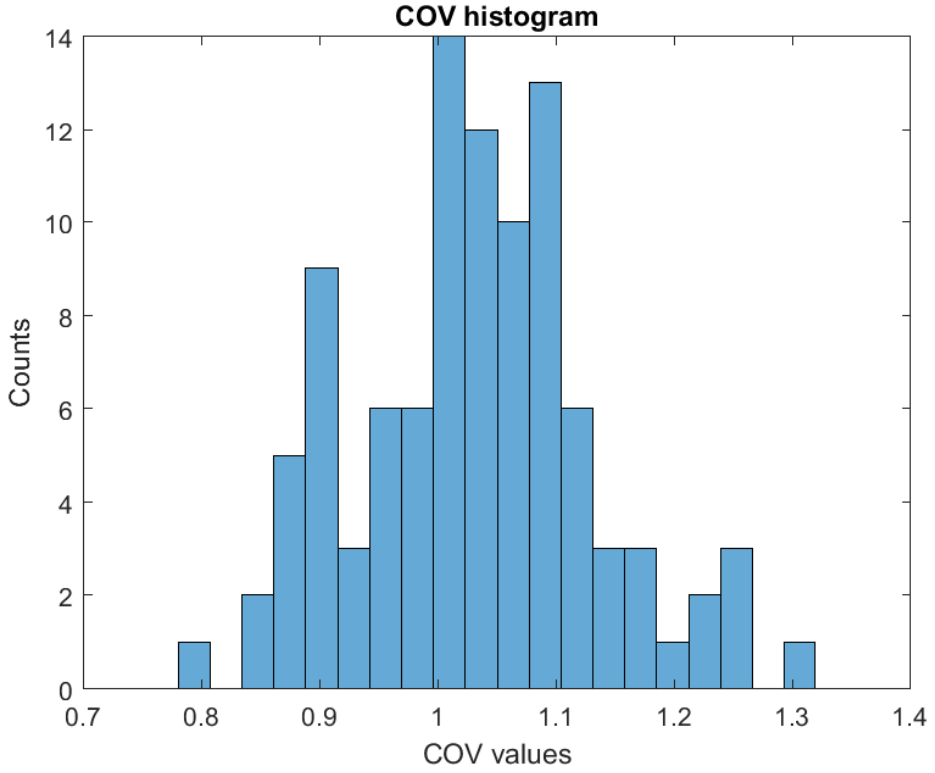

(b) Histogram of COV

Figure 4.14: Histogram plots of firing rates and COVs. (a) Distribution of the firing rates of the 100 spike trains, and firing rates range from 18.71 $spike/s$ to 135.18 $spikes/s$. (b) Distribution of the COVs of the 100 spike trains, and COVs range from 0.793 to 1.310.

The basic statistics of the 100 spike trains are used to reveal the properties of the spike train signals (see figure 4.14). The firing rates of the spike trains vary from 20 $spikes/s$ to around 140 $spikes/s$, with most neurons firing between 30 $spikes/s$ to 80 $spikes/s$. The mean lengths of interspike intervals ranges from 7.397 ms to 53.462 ms, corresponding to the highest and the lowest firing rate, respectively. The standard deviations of the interspike intervals of the 100 signals is between 6.405 to 58.685 ms. The COV values vary from 0.793 to 1.310, with the majority around 1, indicating that the means and standard deviations of ISI of these spike trains are numerically close, which indicates they have random, Poisson-like firing. The simulated network is subject to the analyses presented in section 4.3.

There are 5 cases taken into account. Considering the centre-surround pattern adopted in this simulated network (see figure 4.13 (b) and (c)), neurons separated in space are likely to communicate with each other with lower probability. Therefore, spike trains of spatially scattered neurons are highly likely to be uncorrelated. The first case involves spike trains generated by neurons 33, 57 and 10. Their relative positions can be indicated by figure 4.13 (a). The firing rates of these spike trains are 37.96 $spikes/s$, 44.16 $spikes/s$ and 26.74 $spikes/s$, respectively and the corresponding COV values are 0.879, 0.859 and 1.009. Figure 4.15 shows the analysis results. The spectra of the three spike trains have a reduced magnitude below 160 Hz, while the first two spectra (figure 4.15 (a) and (b)) are of spike trains having higher firing rates and show an increase below 10 Hz. As may be expected, the estimated cumulants density behaves randomly. There is no area indicating third order dependency between the three spike trains. Two sections through the third order cumulant density at fixed u and $u - v$ are shown in figure 4.15 (e) and (f). The two sections indicate that the presynaptic neurons spiking prior to an postsynaptic neuron has no facilitating effect on the output of the postsynaptic neuron, which indicates no third order interaction occurs between these three neurons in this network.

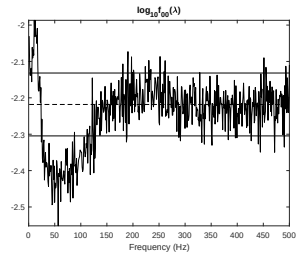

(a) Log spectrum of N_0

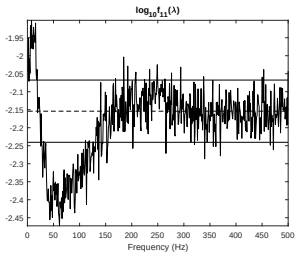

(b) Log spectrum of N_1

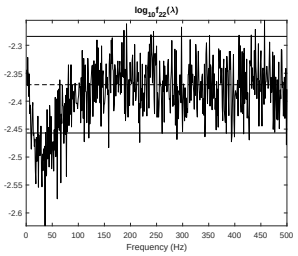

(c) Log spectrum of N_2

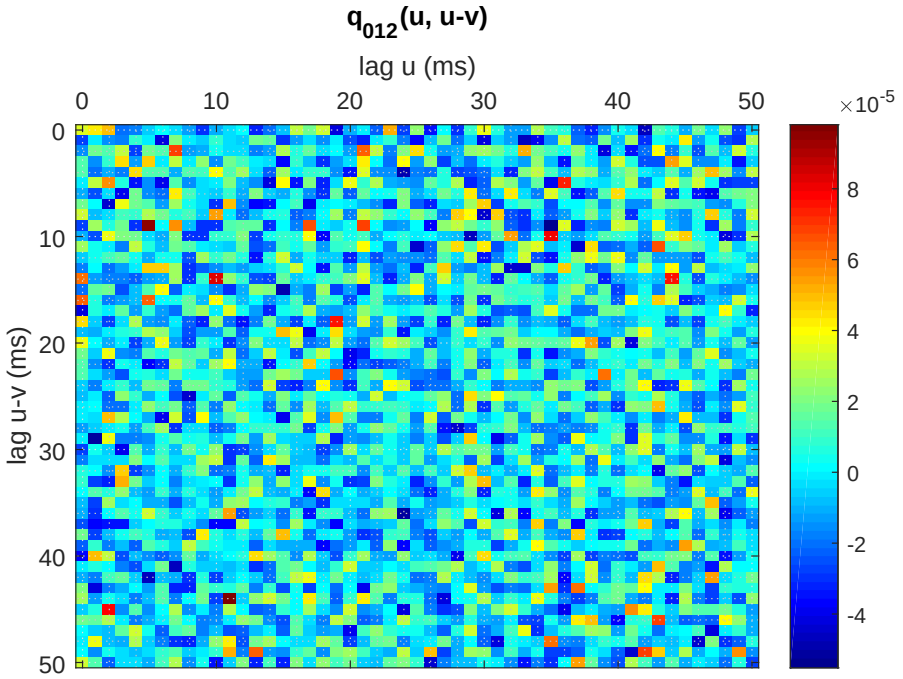

(d) Third order cumulant density

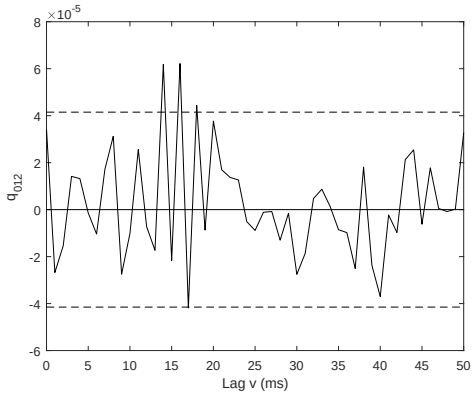

(e) A section of third order cumulant density

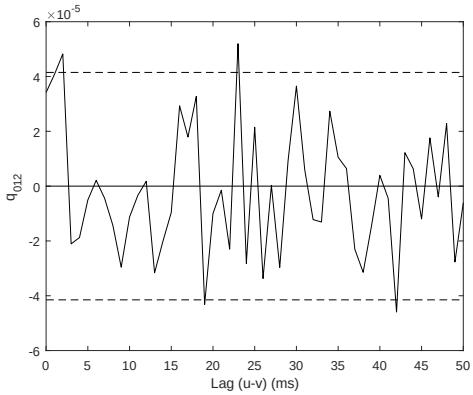

(f) A section of third order cumulant density

Figure 4.15: The top panel is plots of estimated log_{10} auto-spectrum of spike trains N_0, N_1 and N_2, respectively, (a) $log_{10}\hat{f}_{00}(\lambda)$, (b) $log_{10}\hat{f}_{11}(\lambda)$ and (c) $log_{10}\hat{f}_{22}(\lambda)$. The two solid lines represent upper and lower 95% confidence limits, dash line represents the asymptotic value. The middle panel (d) is the pixel image of estimated third order cumulant density, $q_{012}(u, u-v)$ with the colour bar on its right indicating the strengths of different colour. The bottom panel is plots of (e) and (f) third order cumulant density at fixed time lags with the confidence limits and the asymptotic value.

Figure 4.16 shows the analysis result of triplet neurons spatially close to each other. The relative positions of neurons 55, 45 and 56 are as shown in figure 4.13 (a). According to the centre-surround pattern of excitatory connectivity (figure 4.13 (b)), neuron 55 as a postsynaptic neuron receives excitatory inputs from presynaptic neurons 45 and 56. Therefore, third order interaction may be expected in this triplet.Similar to spectral in figure 4.15, a decrease in magnitude below 160 Hz can be found in all three spectra shown in figure 4.16 (a), (b) and (c). The third order cumulant estimate in figure 4.16 (d) shows significant third order interactions between the three spike trains. Significant values of the cumulant can be identified at the upper left corner of the pixel plot, within a $10\ ms * 10\ ms$ square. The highest positive value of the cumulant is located at a lag pair of $u = 2ms$ and $u - v = 1ms$. Two sections through the highest cumulant point show the interaction pattern in more detail (see figure 4.16 (e) and (f)). Significant values below $10ms$ lag can be interpreted as a third order interaction when presynaptic spikes occur less than $10ms$ before an output spike of the postsynaptic neuron. The highest cumulant at ($u = 2ms$, $u - v = 1ms$) indicates that two closely grouped input spikes facilitates an output spike most likely. This result is consistent with the centre-surround pattern of the excitatory connectivity adopted in this simulated network.

Figure 4.17 shows the analysis result after increasing the distance between the two presynaptic neurons and the postsynaptic neuron. The triplet consists of neurons 55, 35 and 57. The relative positions of these neurons are as shown in figure 4.13 (a). These two presynaptic neurons still send excitatory inputs to neuron 55 according to the centre-surround pattern of excitatory connectivity (figure 4.13 (b)). Therefore, significant values of third order cumulant density are expected from this triplet. The third order cumulant estimate in figure 4.17 (d) indicates the presence of third order interactions as expected. Significant values of the cumulants density can be identified in the similar upper left corner area, within an approximate the same $10\ ms * 10\ ms$ square. Compared with the results shown in figure 4.16, the maximal value of the cumulant density corresponds slightly larger lags along both u and $u - v$ axes, located at a lag pair of $u = 4ms$ and $u - v = 2ms$, which is consistent with the further relative positions compared with the triplet considered in figure 4.16. Two sections through

the maximum cumulant density show the third order interaction pattern in more detail (see figure 4.17 (e) and (f)). Significant values below $12ms$ lag can be interpreted as a third order interaction when presynaptic spikes occur less than $12ms$ prior to an output spike. This result is consistent with the centre-surround pattern of the excitatory connectivity and the relative positions in this simulated network.

Moving one of the presynaptics neuron by 1 unit further provides another combination of spike trains. Neuron 25 is one unit further away from postsynaptic neuron 55 compared to neuron 35 and is an inhibitory neuron. According to the interaction pattern of the inhibitory connectivity in the network (see figure 4.13 (c)), neuron 55 receives an inhibitory input from neuron 25. Figure 4.18 shows the analysis result of the triplet containing neurons 55, 25 and 57. The third order cumulant estimate in figure 4.18 (d) indicates the third order interactions are present but weaker compared with figure 4.17. Cumulant values near the origin at the upper left corner are still significantly higher. Compared with the results shown in figure 4.17, there is smaller area of significant cumulant density values, and the maximal value of the cumulant is located at a lag pair of $u = 2ms$ and $u - v = 7ms$. Two sections through the highest cumulant point show the third order interaction pattern in more detail (see figure 4.18 (e) and (f)). Significant values have a narrow duration in these two plots. In figure 4.18 (e), a section between $10\ ms$ to $45\ ms$ shows a smoother oscillation with almost continuous section of negative value approaching the lower confidence limit. This is probably due to the inhibitory effect of neuron 25 with slow time course.

Figure 4.19 shows the analysis result after further increasing the distance between the two presynaptic neurons and the postsynaptic neuron. This triplet consists of neurons 55, 5 and 60. The relative positions of these neurons are as shown in figure 4.13 (a). According to the centre-surround pattern shown in figure 4.13 (b) and (c), there are not any excitatory or inhibitory connectivities between these three neurons in addition to the increased spanning between them. The probability of showing any significant values of third order cumulant density are hence likely to be low. As might be expected, figure 4.19 (d) indicates that the values of estimated cumulant does not show

any dominant feature instead of fluctuating randomly. Two sections show the majority of third order cumulant values are bounded with only single values outside the upper and lower confidence limits (see figure 4.19 (e) and (f)). This suggests there are not any third order interactions between the chosen neuronal triplet.

This section shows results from using the unified third order time-frequency domain analysis network on a simulated cortical network. The results show that the proposed framework is capable of capturing third order interactions in a spiking neuronal network. This provides a strong evidence of the applicability of the framework. In the next section, the UTO analysis framework will be applied to the hippocampal data introduced in section 4.2.

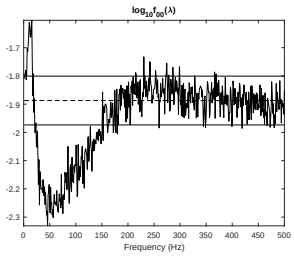

(a) Log spectrum of N_0

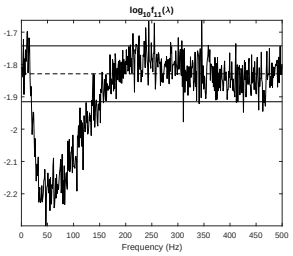

(b) Log spectrum of N_1

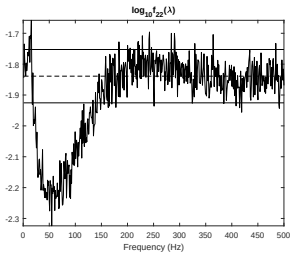

(c) Log spectrum of N_2

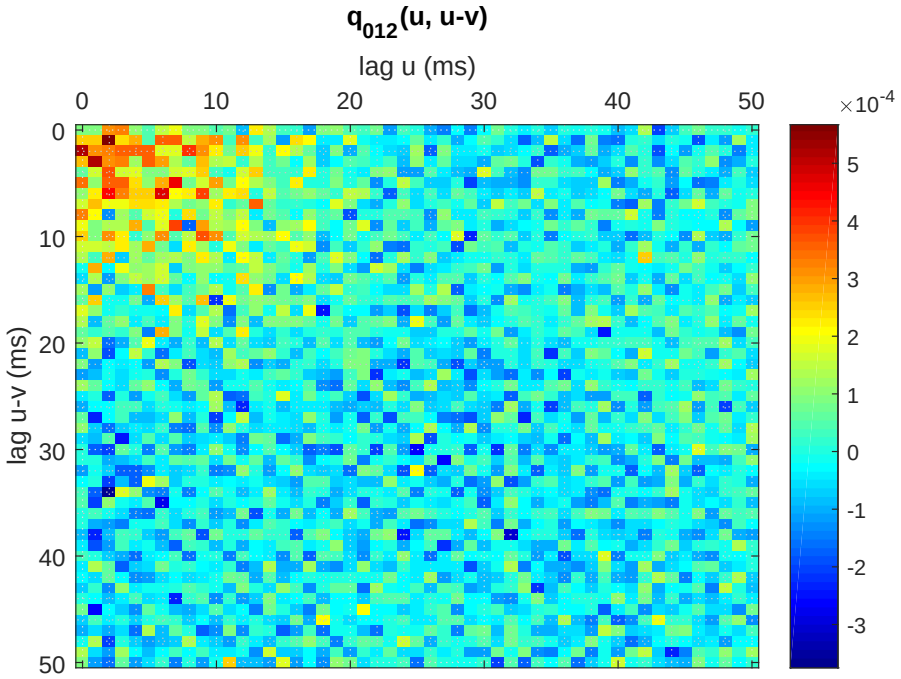

(d) Third order cumulant density

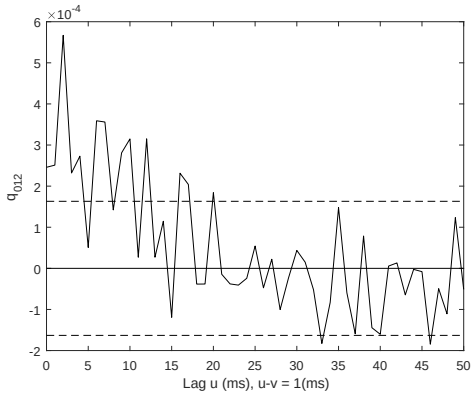

(e) A section of third order cumulant density

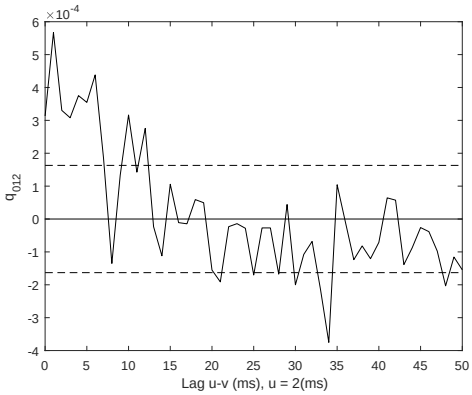

(f) A section of third order cumulant density

Figure 4.16: The top panel is plots of estimated log_{10} auto-spectrum of spike trains N_0, N_1 and N_2, respectively, (a) $log_{10}\hat{f}_{00}(\lambda)$, (b) $log_{10}\hat{f}_{11}(\lambda)$ and (c) $log_{10}\hat{f}_{22}(\lambda)$. The two solid lines represent upper and lower 95% confidence limits, dash line represents the asymptotic value. The middle panel (d) is the pixel image of estimated third order cumulant density, $q_{012}(u, u-v)$ with the colour bar on its right indicating the strengths of different colour. The bottom panel is plots of (e) and (f) third order cumulant density at fixed time lags with the confidence limits and the asymptotic value.

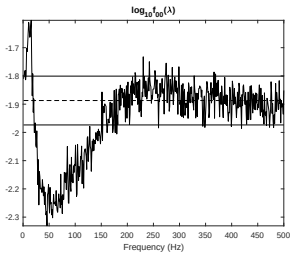

(a) Log spectrum of N_0

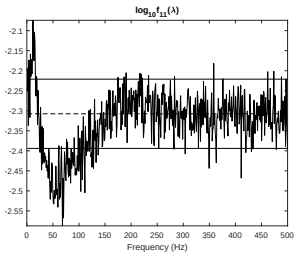

(b) Log spectrum of N_1

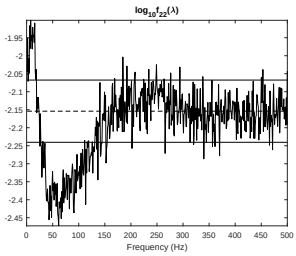

(c) Log spectrum of N_2

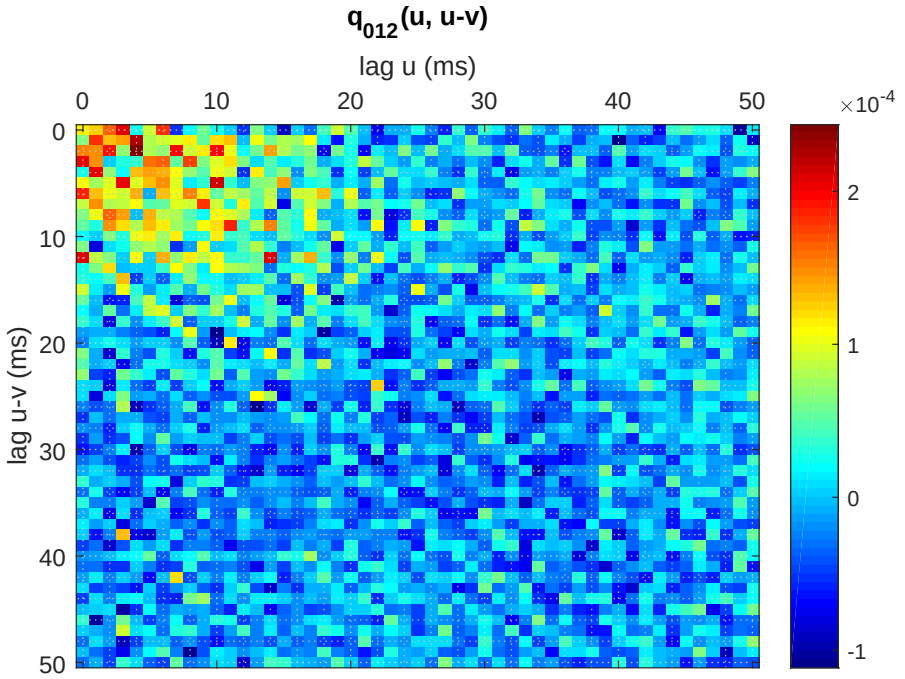

(d) Third order cumulant density

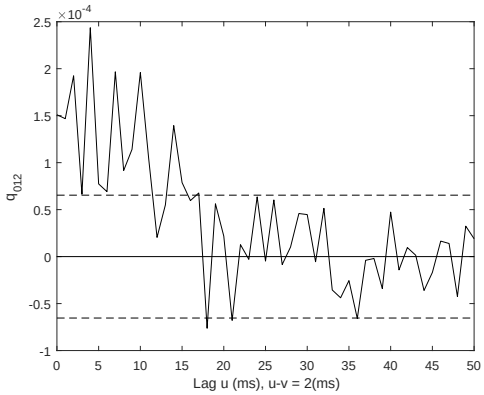

(e) A section of third order cumulant density

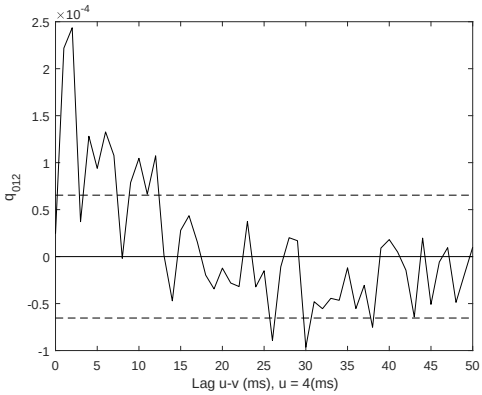

(f) A section of third order cumulant density

Figure 4.17: The top panel is plots of estimated log_{10} auto-spectrum of spike trains N_0, N_1 and N_2, respectively, (a) $log_{10}\hat{f}_{00}(\lambda)$, (b) $log_{10}\hat{f}_{11}(\lambda)$ and (c) $log_{10}\hat{f}_{22}(\lambda)$. The two solid lines represent upper and lower 95% confidence limits, dash line represents the asymptotic value. The middle panel (d) is the pixel image of estimated third order cumulant density, $q_{012}(u, u-v)$ with the colour bar on its right indicating the strengths of different colour. The bottom panel is plots of (e) and (f) third order cumulant density at fixed time lags with the confidence limits and the asymptotic value.

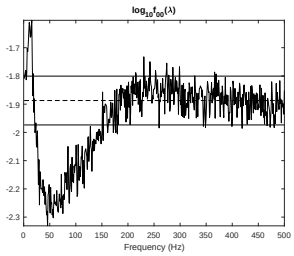

(a) Log spectrum of N_0

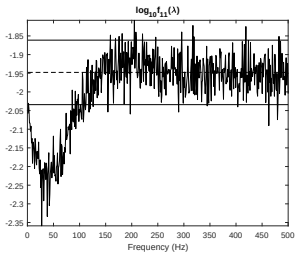

(b) Log spectrum of N_1

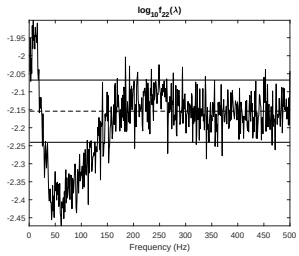

(c) Log spectrum of N_2

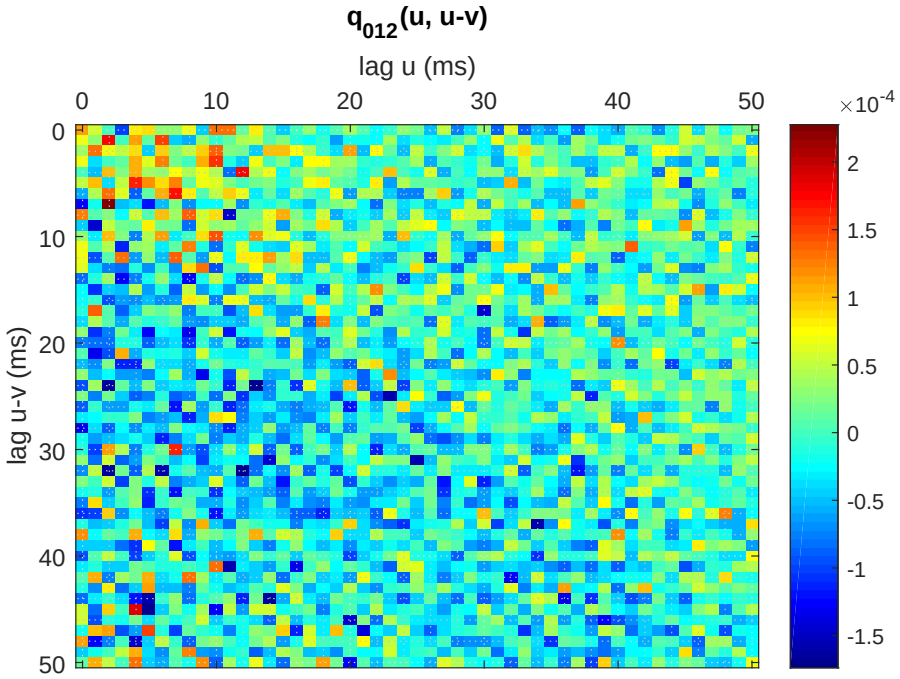

(d) Third order cumulant density

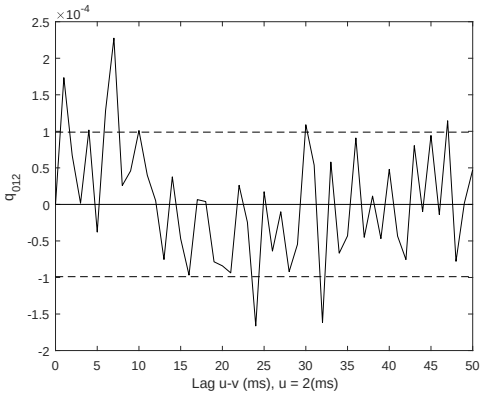

(e) A section of third order cumulant density

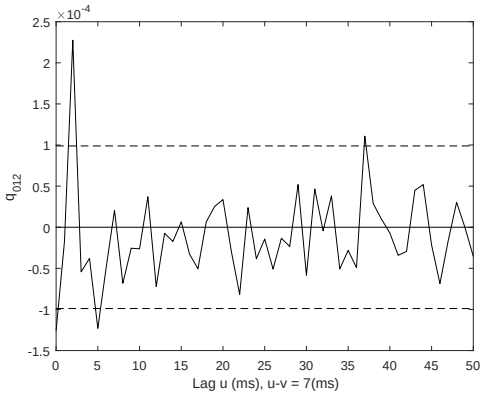

(f) A section of third order cumulant density

Figure 4.18: The top panel is plots of estimated log_{10} auto-spectrum of spike trains N_0, N_1 and N_2, respectively, (a) $log_{10}\hat{f}_{00}(\lambda)$, (b) $log_{10}\hat{f}_{11}(\lambda)$ and (c) $log_{10}\hat{f}_{22}(\lambda)$. The two solid lines represent upper and lower 95% confidence limits, dash line represents the asymptotic value. The middle panel (d) is the pixel image of estimated third order cumulant density, $q_{012}(u, u-v)$ with the colour bar on its right indicating the strengths of different colour. The bottom panel is plots of (e) and (f) third order cumulant density at fixed time lags with the confidence limits and the asymptotic value.

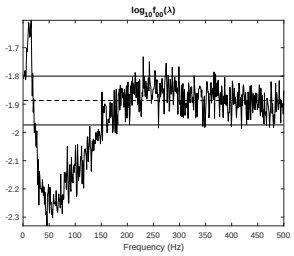

(a) Log spectrum of N_0

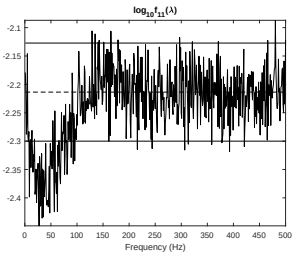

(b) Log spectrum of N_1

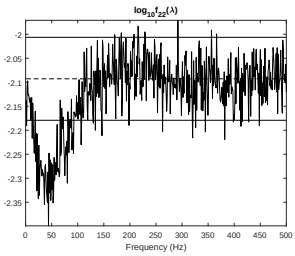

(c) Log spectrum of N_2

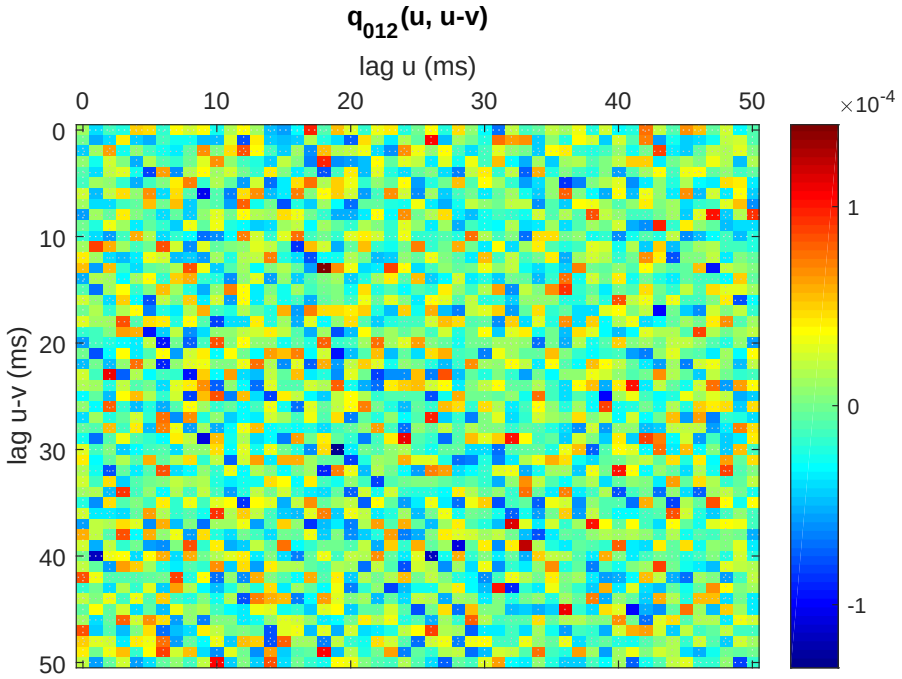

(d) Third order cumulant density

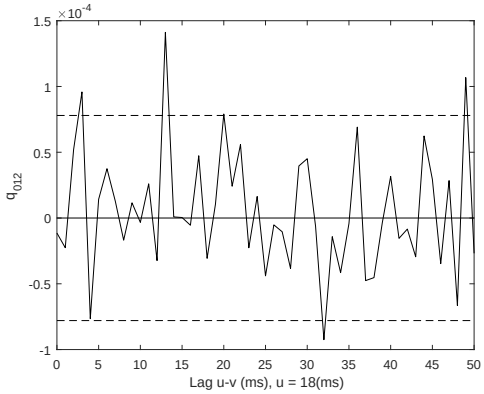

(e) A section of third order cumulant density

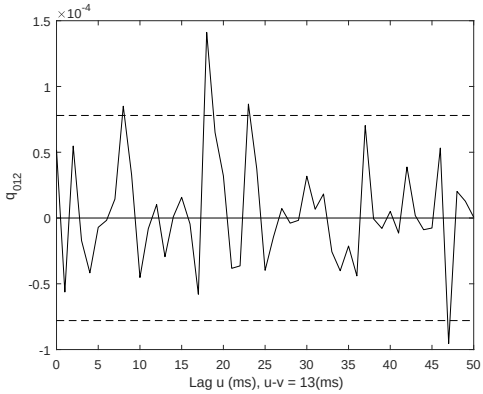

(f) A section of third order cumulant density

Figure 4.19: The top panel is plots of estimated log_{10} auto-spectrum of spike trains N_0, N_1 and N_2, respectively, (a) $log_{10}\hat{f}_{00}(\lambda)$, (b) $log_{10}\hat{f}_{11}(\lambda)$ and (c) $log_{10}\hat{f}_{22}(\lambda)$. The two solid lines represent upper and lower 95% confidence limits, dash line represents the asymptotic value. The middle panel (d) is the pixel image of estimated third order cumulant density, $q_{012}(u, u-v)$ with the colour bar on its right indicating the strengths of different colour. The bottom panel is plots of (e) and (f) third order cumulant density at fixed time lags with the confidence limits and the asymptotic value.

4.5 Third Order Analysis on Experimental Data

The UTO developed in section 4.3 has been applied to basic artificial generated triplet spike trains configurations (see section 4.4.1) and to simulated neural network using biophysical point neurone conductance model (see subsection 4.4.2). These verifications proved that the UTO analysis is applicable and able to capture the interactions among three spike trains. It is going to be used to analyse a Multielectrode Array (MEA) single unit dataset which has been discussed in section 4.2. This verification is going to be the proof of the applicability of this framework to real experimental spike trains. It also provides insight into the experimental data, revealing some third order "CA3 - CA1" interaction patterns in the hippocampus.

This dataset consists of 18 spike train signals (see Table 4.3) and each spike train is 5 mins duration. The estimates are obtained applying the UTO analysis using equations (4.7), (4.12), (4.18) - (4.21) to these 5 mins duration signals. All the estimates involving measures in frequency domain have been constructed using segment length $T = 1024$ and number of segments $L = 292$ since each signal is $300\ s$ duration, and all the estimates illustrated as measures in time domain have used the range of time lags $[0, 50]$ ms.

The information flow in hippocampal region is reported generally from CA3 subregion to CA1 subregion. Therefore, it is reasonable to take into account triplets consisting of two CA3 spike trains and one CA1 spike train from the same hemisphere of the brain, illustrated as figure 4.20. The analyses will first be conducted on four "CA3 - CA1" combinations in detail (see table 4.5, rows 1 - 4), since the spike trains in these combinations capture the two main types of third order interaction: short latency and longer latency. One non-"CA3 - CA1" combination is also shown in detail (see table 4.5, row 5). There is not any interactions expected as they are against the "CA3 - CA1" information flow pattern in the hippocampus.

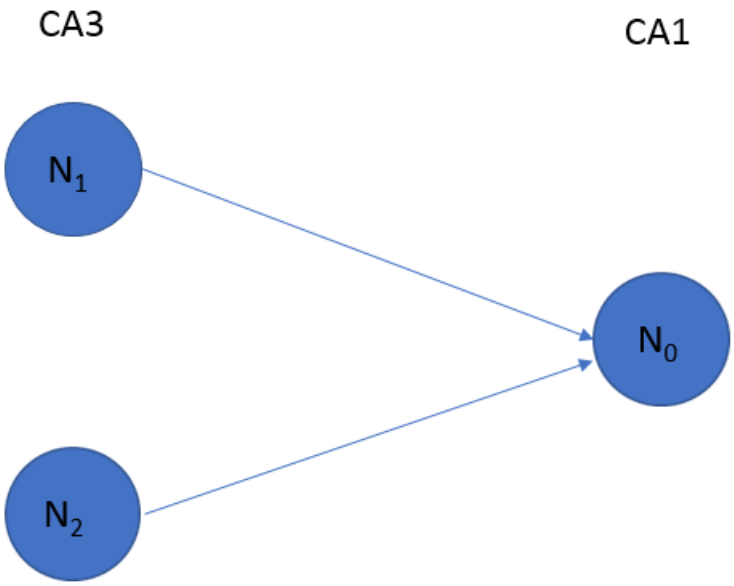

Figure 4.20: Schematic representation of the triplet of "CA3 - CA1" considered in this chapter. N_1 and N_2 are spike trains from the same CA3 subregion, N_0 is a spike train from the CA1 subregion.

N_0	N_1	N_2	Entry
sp10	sp1	sp5	Figure 4.21
sp10	sp1	sp6	Figure 4.22
sp10	sp1	sp7	Figure 4.23
sp10	sp5	sp6	Figure 4.24
sp1	sp15	sp10	Figure 4.25

Table 4.5: Configurations of the left hippocampus

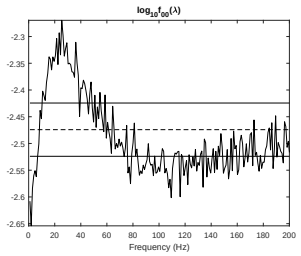

(a) Log spectrum of N_0

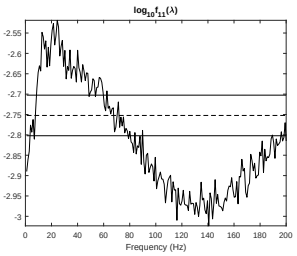

(b) Log spectrum of N_1

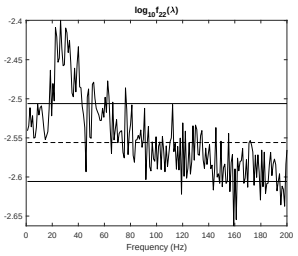

(c) Log spectrum of N_2

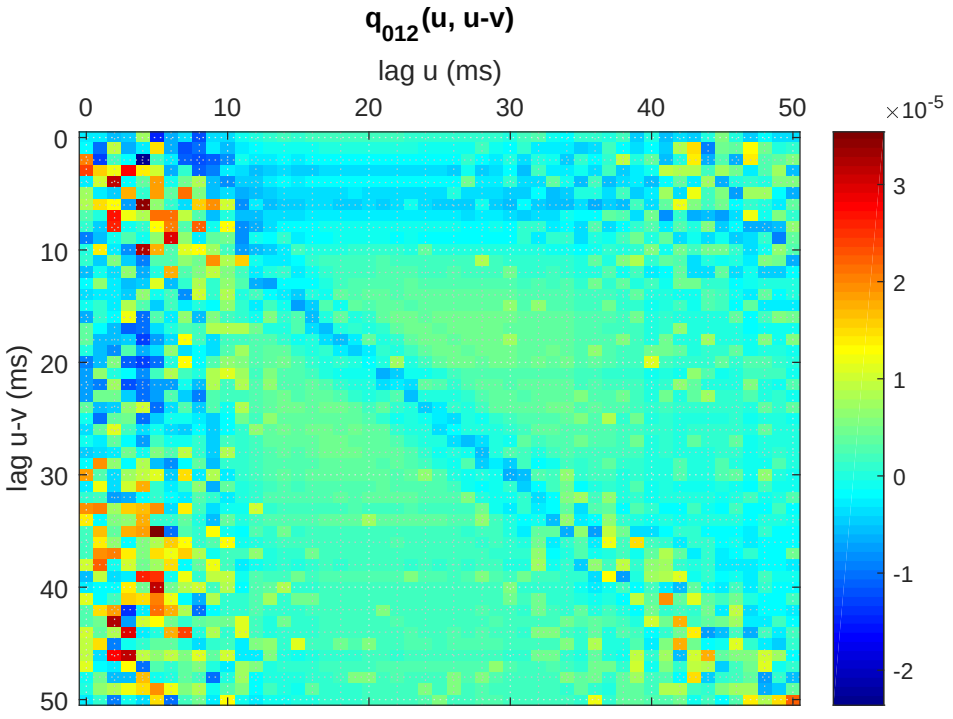

(d) Third order cumulant density

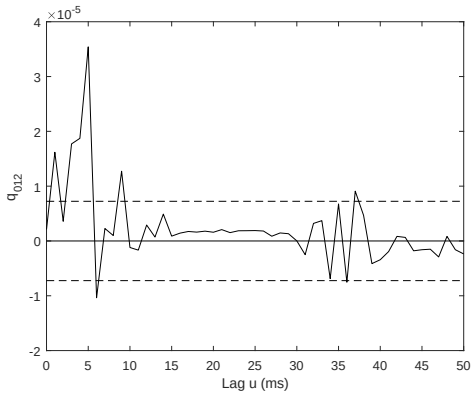

(e) A section of third order cumulant density

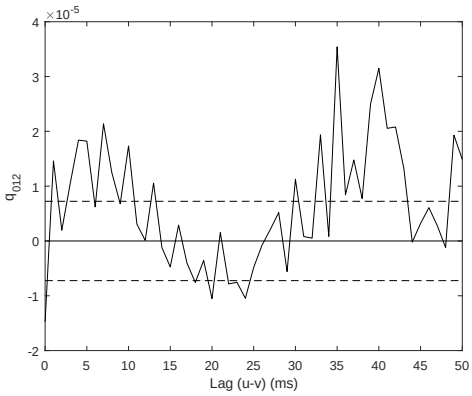

(f) A section of third order cumulant density

Figure 4.21: The top panel is plots of estimated log_{10} auto-spectrum of spike trains N_0, N_1 and N_2, respectively, (a) $log_{10}\hat{f}_{00}(\lambda)$, (b) $log_{10}\hat{f}_{11}(\lambda)$ and (c) $log_{10}\hat{f}_{22}(\lambda)$. The two solid lines represent upper and lower 95% confidence limits, dash line represents the asymptotic value. The middle panel (d) is the pixel image of estimated third order cumulant density, $q_{012}(u, u-v)$ with the colour bar on its right indicating the strengths of different colour. The bottom panel is plots of (e) and (f) third order cumulant density at fixed time lags with the confidence limits and the asymptotic value.

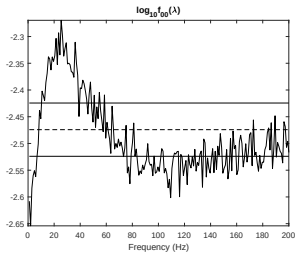

(a) Log spectrum of N_0

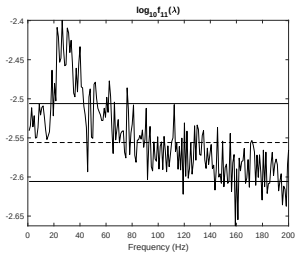

(b) Log spectrum of N_1

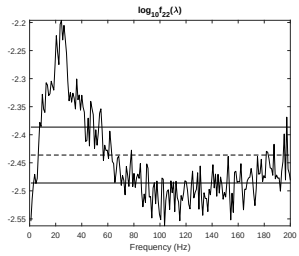

(c) Log spectrum of N_2

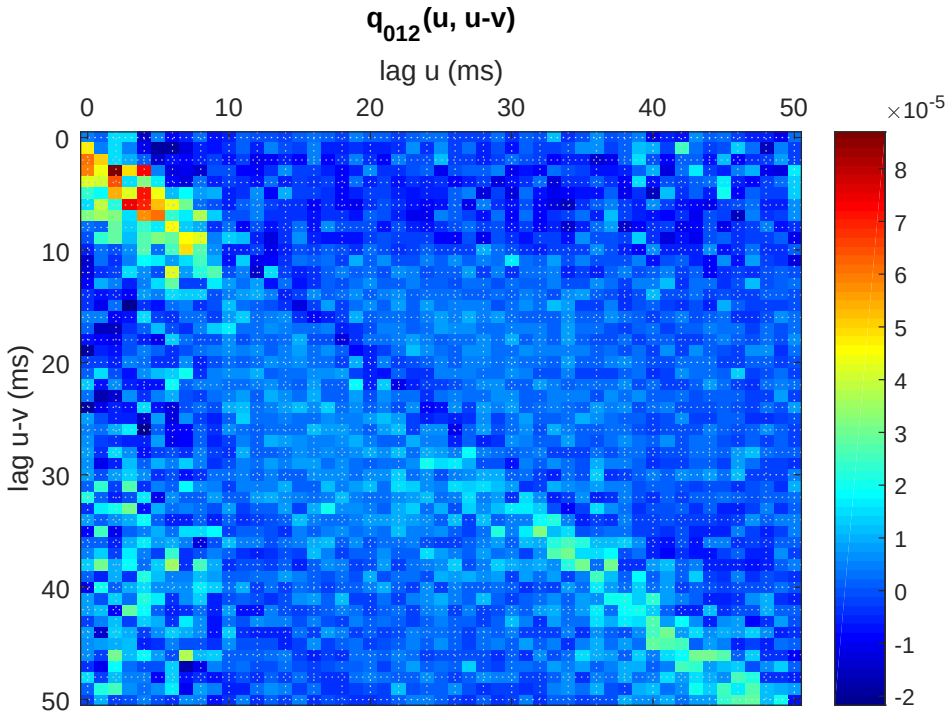

(d) Third order cumulant density

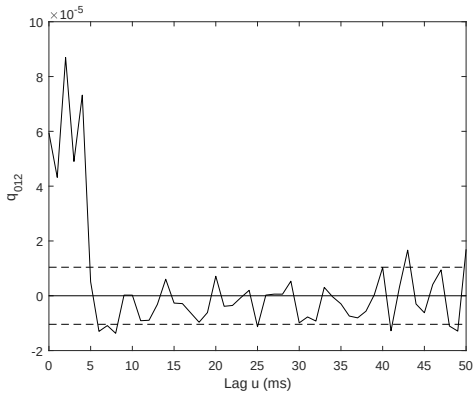

(e) A section of third order cumulant density

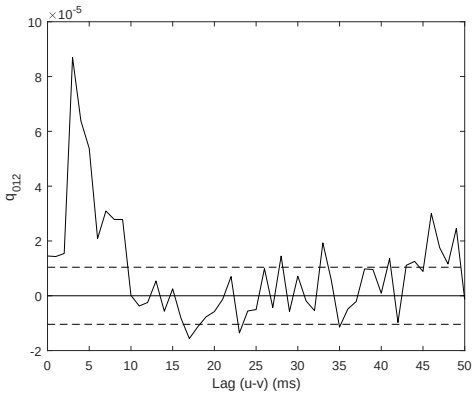

(f) A section of third order cumulant density

Figure 4.22: The top panel is plots of estimated log_{10} auto-spectrum of spike trains N_0, N_1 and N_2, respectively, (a) $log_{10}\hat{f}_{00}(\lambda)$, (b) $log_{10}\hat{f}_{11}(\lambda)$ and (c) $log_{10}\hat{f}_{22}(\lambda)$. The two solid lines represent upper and lower 95% confidence limits, dash line represents the asymptotic value. The middle panel (d) is the pixel image of estimated third order cumulant density, $q_{012}(u, u-v)$ with the colour bar on its right indicating the strengths of different colour. The bottom panel is plots of (e) and (f) third order cumulant density at fixed time lags with the confidence limits and the asymptotic value.

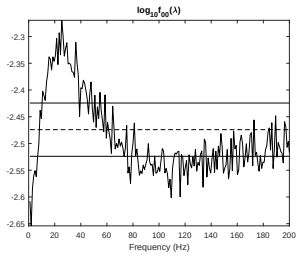

(a) Log spectrum of N_0

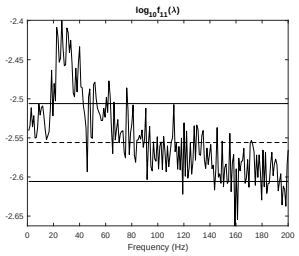

(b) Log spectrum of N_1

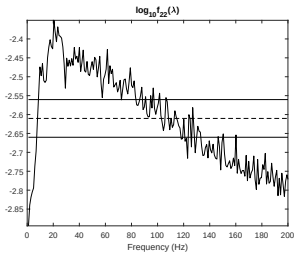

(c) Log spectrum of N_2

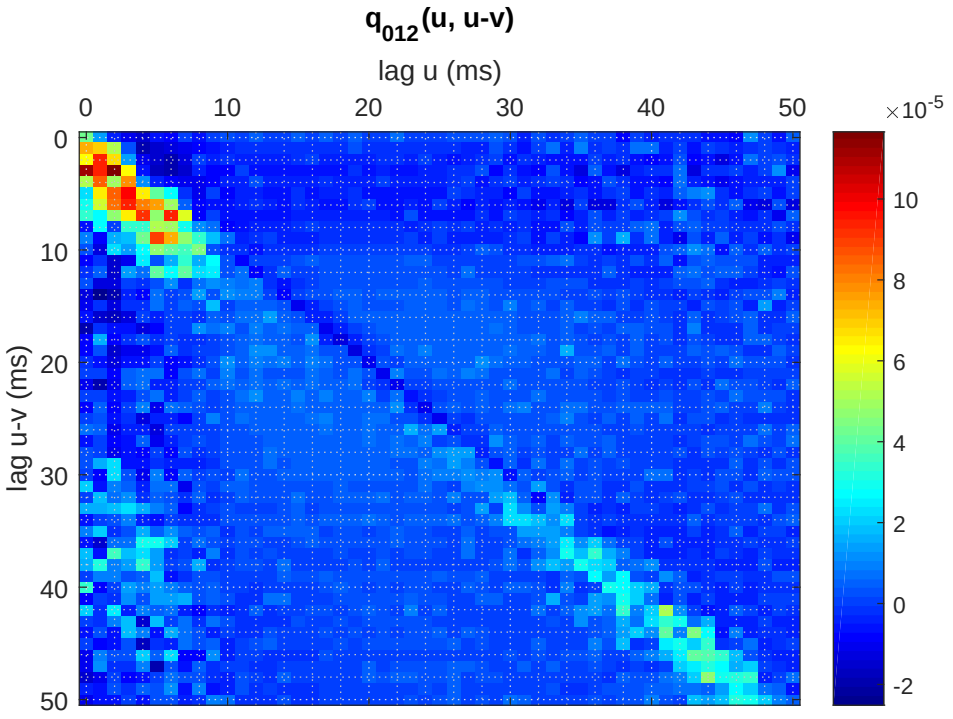

(d) Third order cumulant density

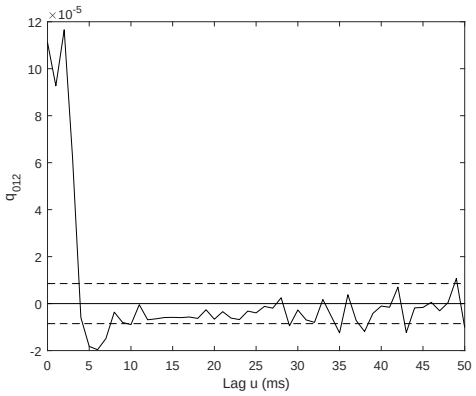

(e) A section of third order cumulant density

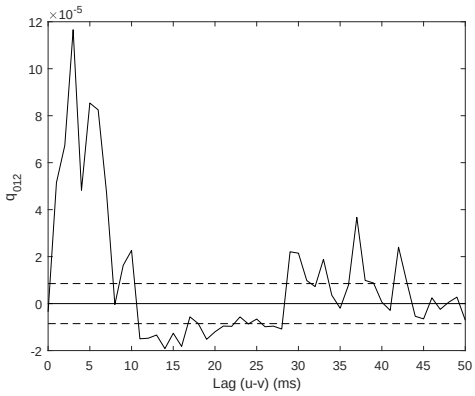

(f) A section of third order cumulant density

Figure 4.23: The top panel is plots of estimated log_{10} auto-spectrum of spike trains N_0, N_1 and N_2, respectively, (a) $log_{10}\hat{f}_{00}(\lambda)$, (b) $log_{10}\hat{f}_{11}(\lambda)$ and (c) $log_{10}\hat{f}_{22}(\lambda)$. The two solid lines represent upper and lower 95% confidence limits, dash line represents the asymptotic value. The middle panel (d) is the pixel image of estimated third order cumulant density, $q_{012}(u, u-v)$ with the colour bar on its right indicating the strengths of different colour. The bottom panel is plots of (e) and (f) third order cumulant density at fixed time lags with the confidence limits and the asymptotic value.

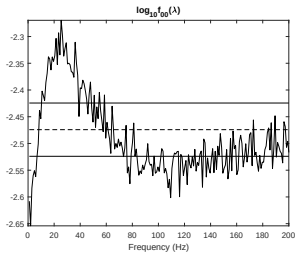

(a) Log spectrum of N_0

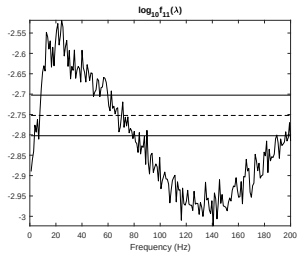

(b) Log spectrum of N_1

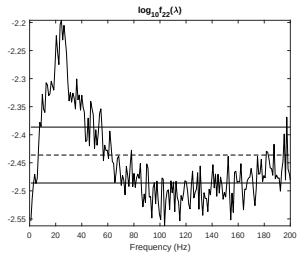

(c) Log spectrum of N_2

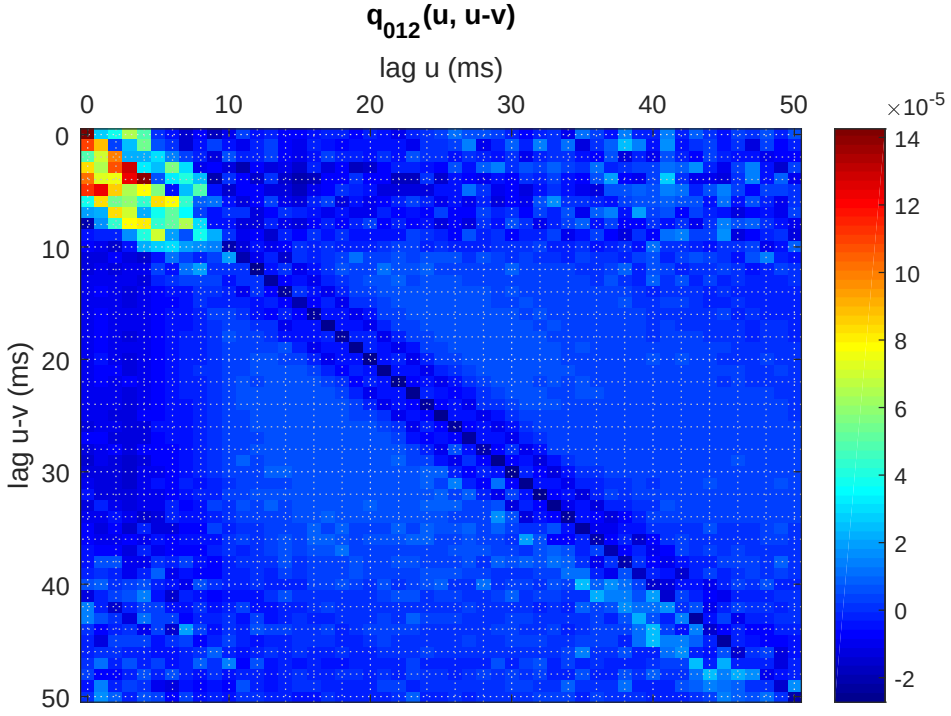

(d) Third order cumulant density

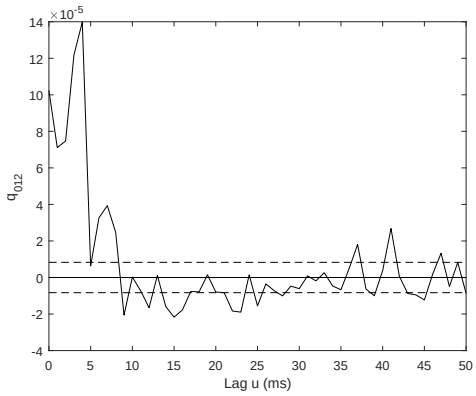

(e) A section of third order cumulant density

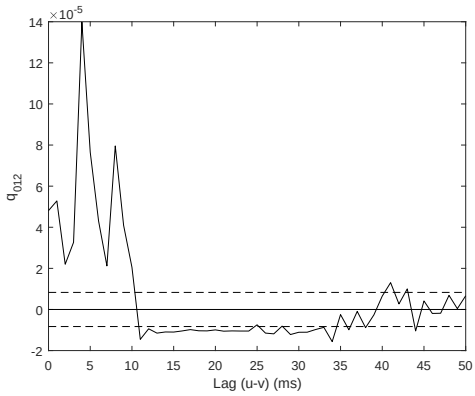

(f) A section of third order cumulant density

Figure 4.24: The top panel is plots of estimated log_{10} auto-spectrum of spike trains N_0, N_1 and N_2, respectively, (a) $log_{10}\hat{f}_{00}(\lambda)$, (b) $log_{10}\hat{f}_{11}(\lambda)$ and (c) $log_{10}\hat{f}_{22}(\lambda)$. The two solid lines represent upper and lower 95% confidence limits, dash line represents the asymptotic value. The middle panel (d) is the pixel image of estimated third order cumulant density, $q_{012}(u, u-v)$ with the colour bar on its right indicating the strengths of different colour. The bottom panel is plots of (e) and (f) third order cumulant density at fixed time lags with the confidence limits and the asymptotic value.

Figure 4.21 shows the estimated cumulant density $q_{012}(u, u-v)$ of the combination (sp10, sp1, sp5) (see table 4.5, row 1). The timing convention is that lags u and (u-v) in ms represent the time to previous input spikes from two CA3 neurons onto one CA1 neuron. Two regions where there are significant features can be identified in figure 4.21 (d). These are highlighted in the two sections at fixed u-v lag of 35 ms shown in figure 4.21 (e) and at fixed u lag of 5 ms shown in figure 4.21 (f). These sections indicate that significant third order interactions can occur when the third spike is between 5-10 ms prior to the CA1 spike and the second spike is between 5-10 ms or 35-45 ms prior to the CA1 spike. Figure 4.21 (a), (b) and (c) show auto-spectral estimates for the CA1 spike and the two CA3 spikes. The dominant feature in each spectrum is a peak around 25 Hz, representing corresponding mean rate of each spike (Yang and Halliday, 2018).

Figure 4.22 shows the estimated cumulant density $q_{012}(u, u-v)$ of another triplet spike trains (sp10, sp1, sp6) (see table 4.5, row 2). A region at the upper-left corner of the pixel diagram (see figures 4.22 (d)) where there is a dominant feature can be identified. Compared with figure 4.21 (d), the second dominant area near the lower-left corner clearly found in figure 4.21(d) is ambiguous in this case. According to the time convention in figure 4.7, the area indicating the occurrence of third order interaction is located with the range with u varying in $[0,\ 8]$ and $u-v$ varying in $[2, 10]$. Two sections going through the maximum value of cumulants at $(u, u-v) = (2, 3)\ ms$ are highlighted at fixed $u-v$ and u respectively in figure 4.22 (e) and (f). These sections indicate that significant third order interactions may take place when one spike in N_2 is between $0-8$ ms prior to the a spike in N_0, combined with a similar priority that a spike in N_1 occurs to the spike in N_0.

Figure 4.23 reveals the similar feature near the origin compared with figure 4.22. The result is consistent with the expectation since the signals taken into account are almost identical, with only the difference that the N_2 is recorded by the same node at the same single unit but spike-sorted out to be another spike trains, which can be expressed by the different spectral(see figure 4.22 (c) and 4.23 (c)). Since they are from the same

combination of single unites, the interaction features are hence similar.

Figure 4.24 shows the analysis result of another triplet neurons with the two inputs neurons in CA3 being spatially closer to each other (sp10-sp5-sp6) (see table 4.5, row 4). According to the time convention in figure 4.7, a relatively smaller difference between the two lag indices u and $u-v$ are expected since ideally it takes the two inputs $N1$ and $N2$ almost the same time to arrive at the output neuron. The third order cumulant estimate in figure 4.24 (d) can be taken as strong proof of the interactions between the the three spike trains. Significant values of the cumulant can be identified at the upper left corner of the pixel plot, located within a $10*10$ square. The highest positive value of the cumulant is located at a lag pair of $u = 4ms$ and $u - v = 4ms$. Two sections through the highest cumulant point show the interaction pattern in more detail (see figure 4.24 (e) and (f)). The ranges of lag u and $u - v$ indicating the occurrence are numerically close, which meets the expectation. Significant values below $10ms$ lag can be interpreted that the third order interaction is presented when presynaptic spikes precede less than $10ms$ to an output spike of the postsynaptic neuron. The highest cumulant at ($u = 4ms$, $u - v = 4ms$) indicates that a pair of closely grouped input spikes facilitates the output spike mostly.

Figure 4.25 shows the analysis result of another triplet signals (sp1-sp15-sp10). The nodes recorded these three signals are comparatively more scattered. Hence, the spatial distances between the single unites on which these spike trains are obtained are larger. The probability of showing any significant values of third order cumulant density are likely to be low. As might be expected, figure 4.25 (d) indicates that the values of estimated cumulant does not show any dominant areas but just single peaks scattering over the plane. Two sections show that almost all third order cumulant values are bounded with single values deviate the expectation at the lag $u - v = 0ms$ (see figure 4.25 (e) and (f)). This indicates there are not any third order interactions between the chosen neuronal triplet.

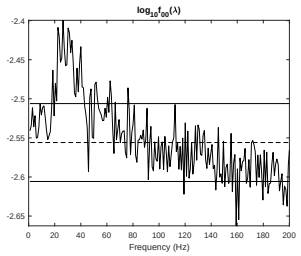

(a) Log spectrum of N_0

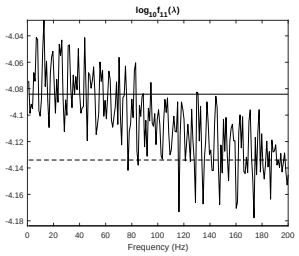

(b) Log spectrum of N_1

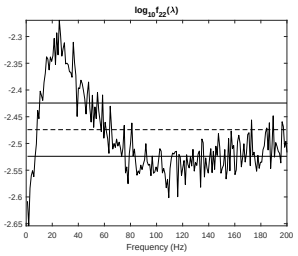

(c) Log spectrum of N_2

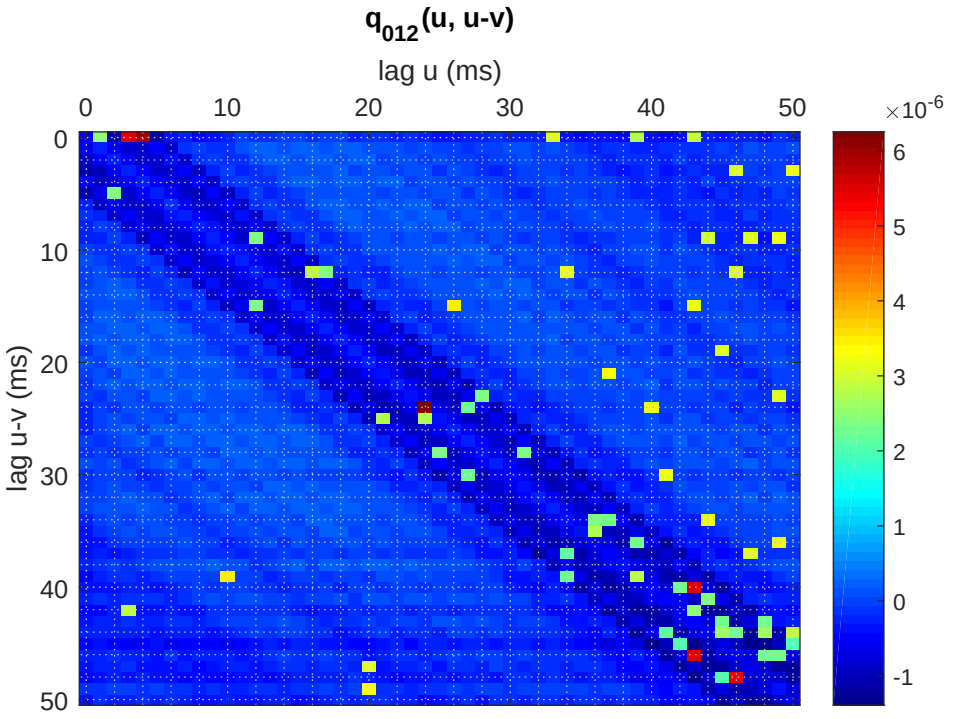

(d) Third order cumulant density

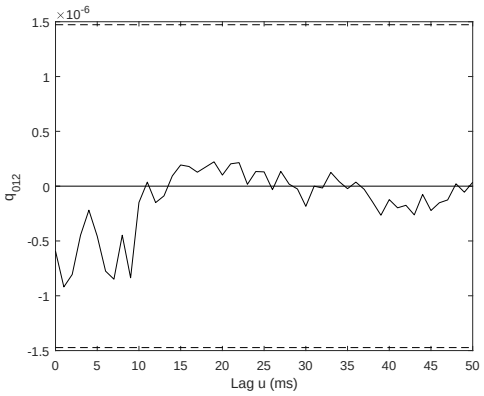

(e) A section of third order cumulant density

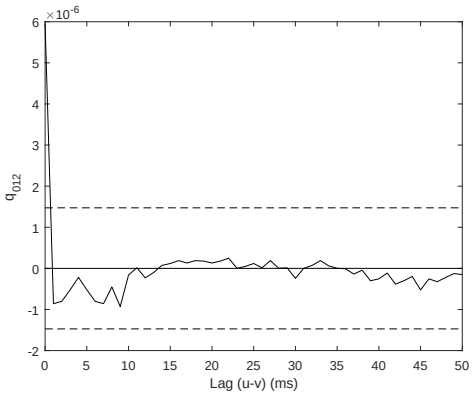

(f) A section of third order cumulant density

Figure 4.25: The top panel is plots of estimated log_{10} auto-spectrum of spike trains N_0, N_1 and N_2, respectively, (a) $log_{10}\hat{f}_{00}(\lambda)$, (b) $log_{10}\hat{f}_{11}(\lambda)$ and (c) $log_{10}\hat{f}_{22}(\lambda)$. The two solid lines represent upper and lower 95% confidence limits, dash line represents the asymptotic value. The middle panel (d) is the pixel image of estimated third order cumulant density, $q_{012}(u, u-v)$ with the colour bar on its right indicating the strengths of different colour. The bottom panel is plots of (e) and (f) third order cumulant density at fixed time lags with the confidence limits and the asymptotic value.

N_0	N_1	N_2	Entry
sp8 (Left CA1)	sp1 (Left CA3)	sp3 (Left CA3)	Figure 4.26 (a)
sp8 (Left CA1)	sp1 (Left CA3)	sp5 (Left CA3)	Figure 4.26 (b)
sp8 (Left CA1)	sp1 (Left CA3)	sp6 (Left CA3)	Figure 4.26 (c)
sp8 (Left CA1)	sp3 (Left CA3)	sp5 (Left CA3)	Figure 4.26 (d)
sp8 (Left CA1)	sp3 (Left CA3)	sp6 (Left CA3)	Figure 4.26 (e)
sp8 (Left CA1)	sp5 (Left CA3)	sp6 (Left CA3)	Figure 4.26 (f)
sp10 (Left CA1)	sp1 (Left CA3)	sp3 (Left CA3)	Figure 4.27 (a)
sp10 (Left CA1)	sp1 (Left CA3)	sp5 (Left CA3)	Figure 4.27 (b)
sp10 (Left CA1)	sp1 (Left CA3)	sp6 (Left CA3)	Figure 4.27 (c)
sp10 (Left CA1)	sp3 (Left CA3)	sp5 (Left CA3)	Figure 4.27 (d)
sp10 (Left CA1)	sp3 (Left CA3)	sp6 (Left CA3)	Figure 4.27 (e)
sp10 (Left CA1)	sp5 (Left CA3)	sp6 (Left CA3)	Figure 4.27 (f)
sp12 (Left CA1)	sp1 (Left CA3)	sp3 (Left CA3)	Figure 4.28 (a)
sp12 (Left CA1)	sp1 (Left CA3)	sp5 (Left CA3)	Figure 4.28 (b)
sp12 (Left CA1)	sp1 (Left CA3)	sp6 (Left CA3)	Figure 4.28 (c)
sp12 (Left CA1)	sp3 (Left CA3)	sp5 (Left CA3)	Figure 4.28 (d)
sp12 (Left CA1)	sp3 (Left CA3)	sp6 (Left CA3)	Figure 4.28 (e)
sp12 (Left CA1)	sp5 (Left CA3)	sp6 (Left CA3)	Figure 4.28 (f)
sp13 (Left CA1)	sp1 (Left CA3)	sp3 (Left CA3)	Figure 4.29 (a)
sp13 (Left CA1)	sp1 (Left CA3)	sp5 (Left CA3)	Figure 4.29 (b)
sp13 (Left CA1)	sp1 (Left CA3)	sp6 (Left CA3)	Figure 4.29 (c)
sp13 (Left CA1)	sp3 (Left CA3)	sp5 (Left CA3)	Figure 4.29 (d)
sp13 (Left CA1)	sp3 (Left CA3)	sp6 (Left CA3)	Figure 4.29 (e)
sp13 (Left CA1)	sp5 (Left CA3)	sp6 (Left CA3)	Figure 4.29 (f)

Table 4.6: Configurations of the left hippocampus

The analyses also are conducted on all this type of combinations to obtain a general sense of the dependencies in this dataset. All the combinations in the left hippocampal part are listed in table 4.6 and all the combinations in the right hippocampal part are listed in table 4.7. At this systematic analysis stage, all the results are illustrated as cumulant densities ploted as pixel diagrams with different colour representing different strength of the cumulant densities. Each result can be retrieved in table 4.6 and 4.7 using the “Entry” columns.

N_0	N_1	N_2	Entry
sp17 (Right CA1)	sp14 (Right CA3)	sp15 (Right CA3)	Figure 4.30 (a)
sp17 (Right CA1)	sp14 (Right CA3)	sp16 (Right CA3)	Figure 4.30 (b)
sp18 (Right CA1)	sp14 (Right CA3)	sp16 (Right CA3)	Figure 4.30 (c)

Table 4.7: Configurations of the right hippocampus

Figures 4.26, 4.27, 4.28 and 4.29 illustrate the systematic study of the left hippocampal (CA1, CA3, CA3) spikes triplet listed in table 4.6. Across all these triplets combinations, areas near the origins indicating short lags both along the u axis and $u - v$ axis can be identified with large cumulant densities values, which indicates that across the dataset, short spike times for three spikes with one from each train exist broadly. High cumulants in this types of region can imply that there is an increasing probability of occurrence of a significant third order interaction if the two referenced CA3 spikes are shortly prior to the CA1 spike.

In some cases where the signal $sp1$ involved, some features along the $u - v$ axis and with small u values can be identified (see figure 4.26 (a), (b) and (c), figure 4.27 (a), (b) and (c), figure 4.28 (a), (b) and (c) and figure 4.29 (a), (b) and (c)). According the time convention discussed in section 4.3, these significant areas with values of $u - v$ lying above the principal diagonal may indicates that a CA3 spontaneous spike in N_1 precedes the evoked CA3 spike in N_1 and there for the spontaneous one may be regarded as a conditioning contribution for investigating the contribution that the evoked one has to the subsequent CA1 spikes.

Figures 4.30 illustrates the systematic study of the right hippocampal (CA1, CA3, CA3) spikes triplet listed in table 4.7. Compared with the left hippocampus cases, the interactions in the right hippocampus are quieter due to the lower firing rates. Similar high cumulant densities area with short u and $u - v$ values exist.

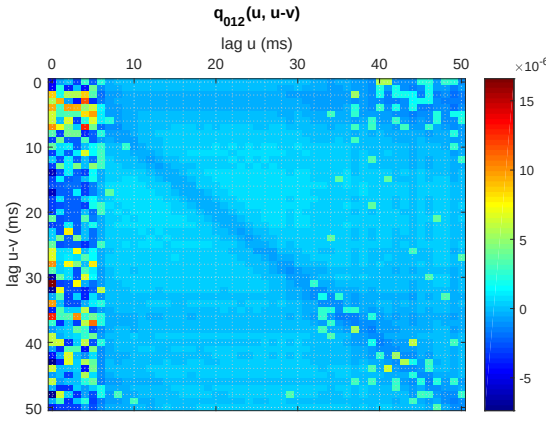

(a) N_0:sp8, N_1:sp1, N_2:sp3

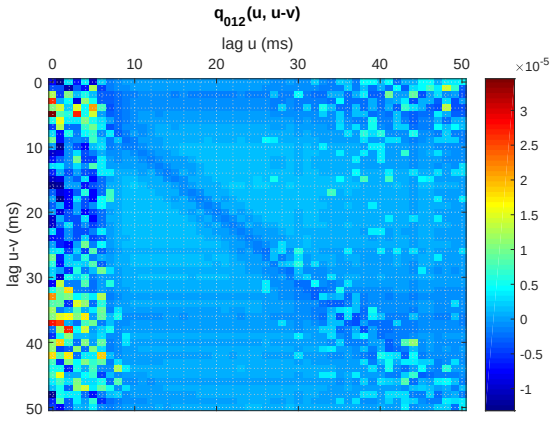

(b) N_0:sp8, N_1:sp1, N_2:sp5

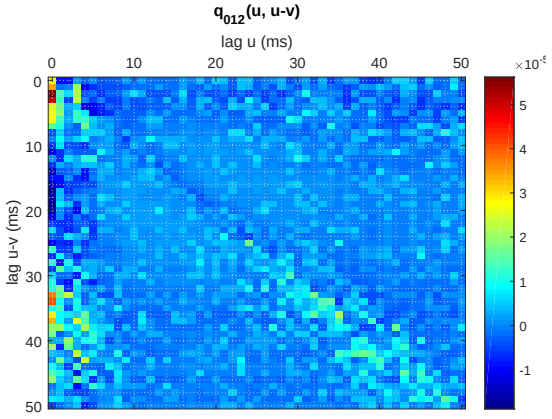

(c) N_0:sp8, N_1:sp1, N_2:sp6

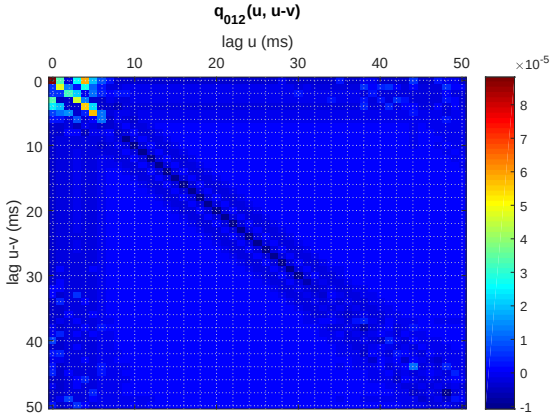

(d) N_0:sp8, N_1:sp3, N_2:sp5

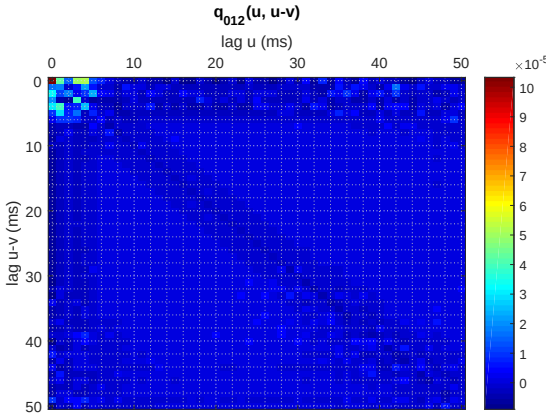

(e) N_0:sp8, N_1:sp3, N_2:sp6

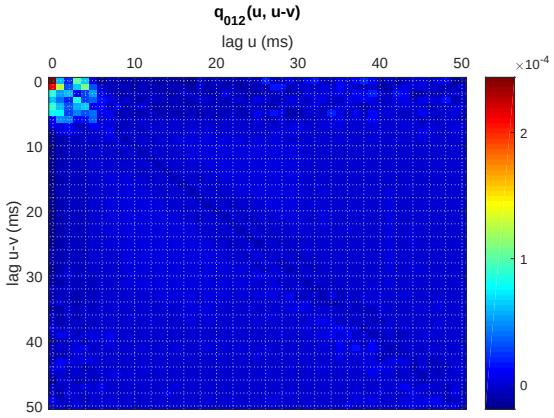

(f) N_0:sp8, N_1:sp5, N_2:sp6

Figure 4.26: Third order cumulant density estimates of the hippocampal data (see section 4.2).

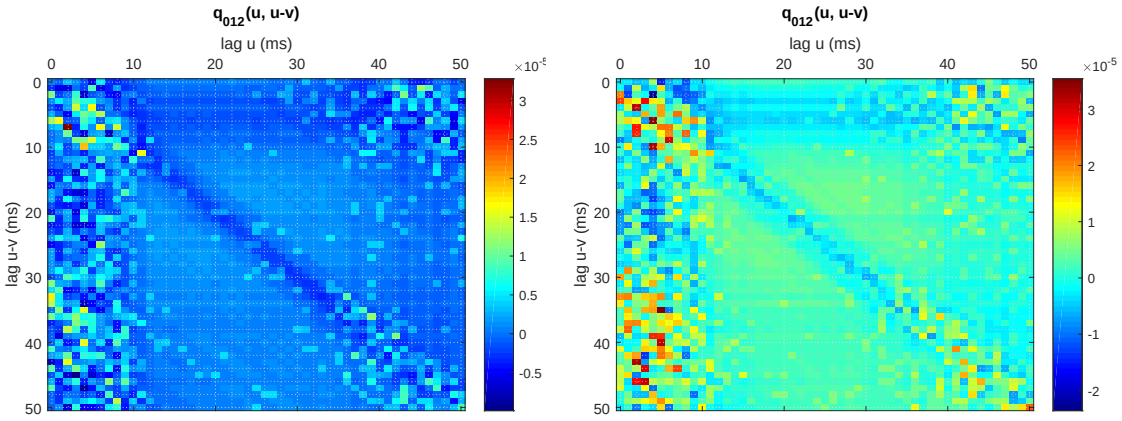

(a) N_0:sp10, N_1:sp1, N_2:sp3

(b) N_0:sp10, N_1:sp1, N_2:sp5

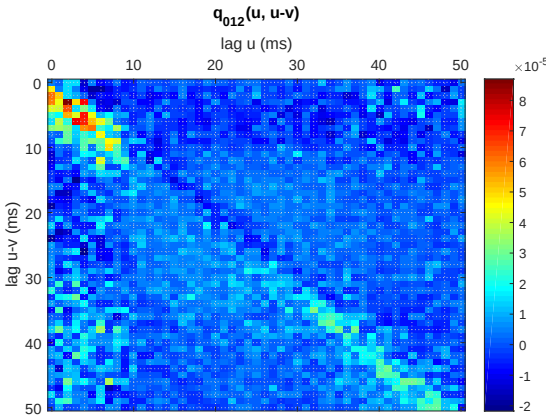

(c) N_0:sp10, N_1:sp1, N_2:sp6

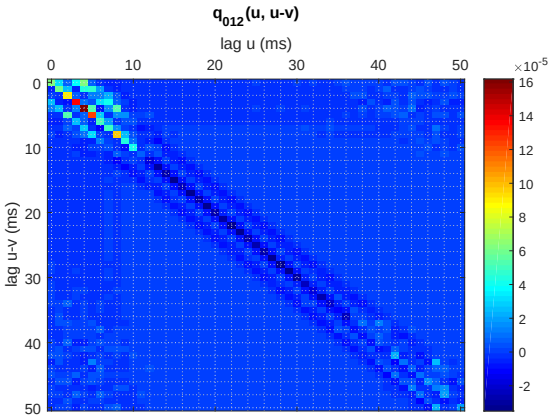

(d) N_0:sp10, N_1:sp3, N_2:sp5

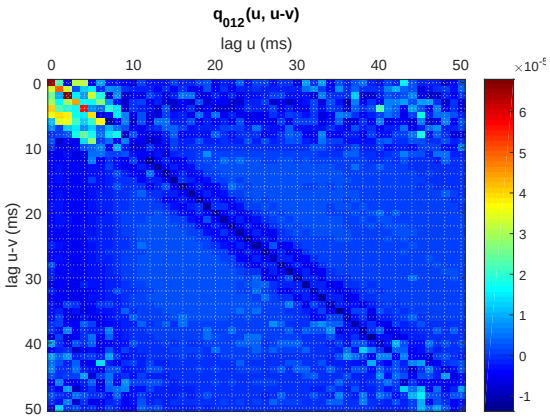

(e) N_0:sp10, N_1:sp3, N_2:sp6

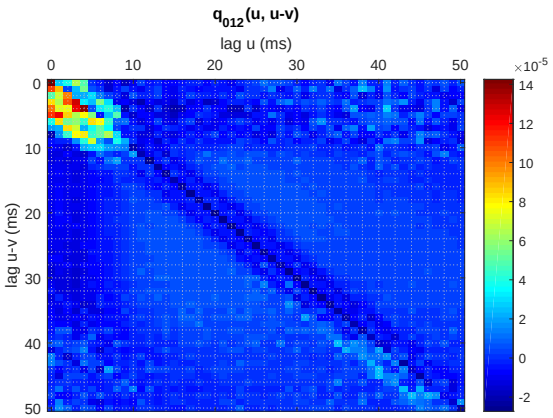

(f) N_0:sp10, N_1:sp5, N_2:sp6

Figure 4.27: Third order cumulant density estimates of the hippocampal data (see section 4.2).

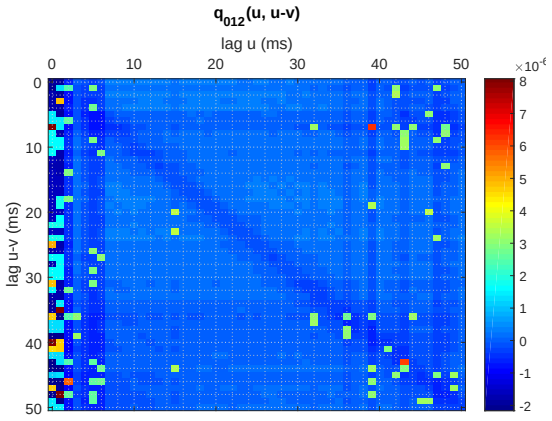

(a) N_0:sp12, N_1:sp1, N_2:sp3

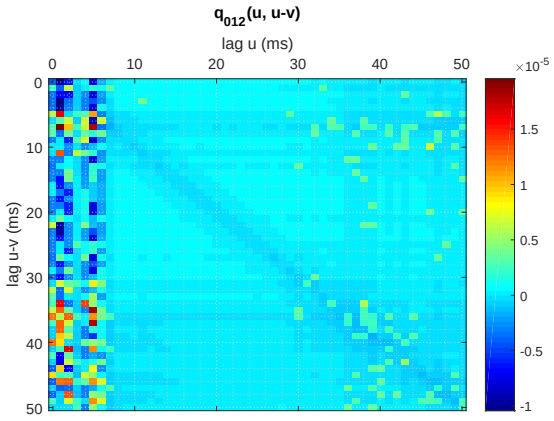

(b) N_0:sp12, N_1:sp1, N_2:sp5

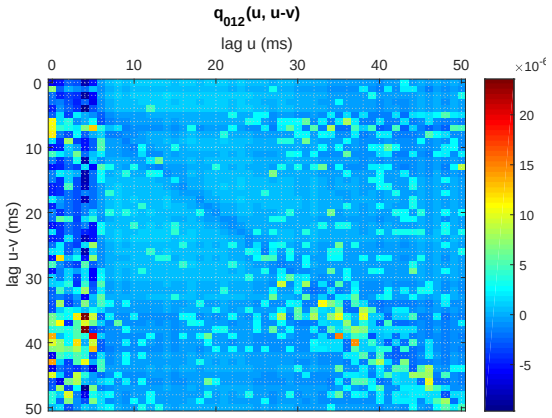

(c) N_0:sp12, N_1:sp1, N_2:sp6

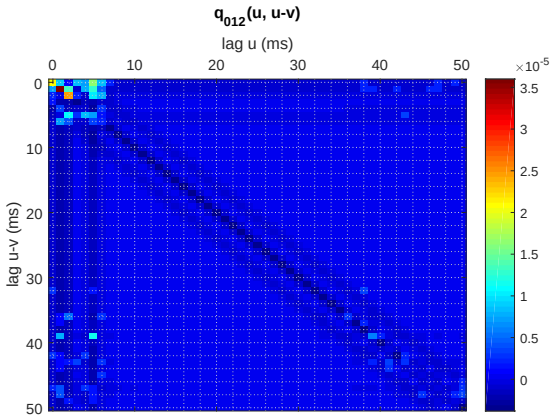

(d) N_0:sp12, N_1:sp3, N_2:sp5

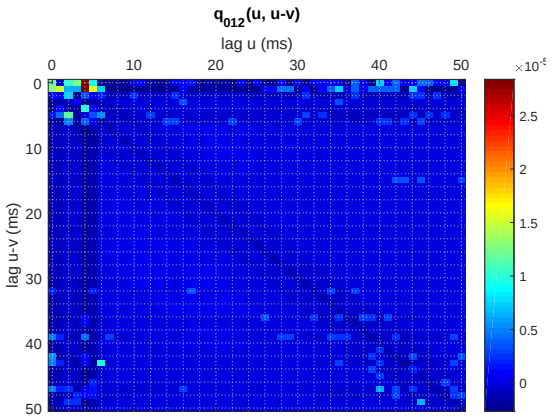

(e) N_0:sp12, N_1:sp3, N_2:sp6

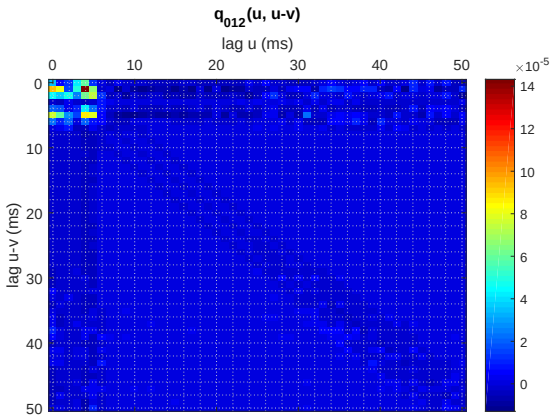

(f) N_0:sp12, N_1:sp5, N_2:sp6

Figure 4.28: Third order cumulant density estimates of the hippocampal data (see section 4.2).

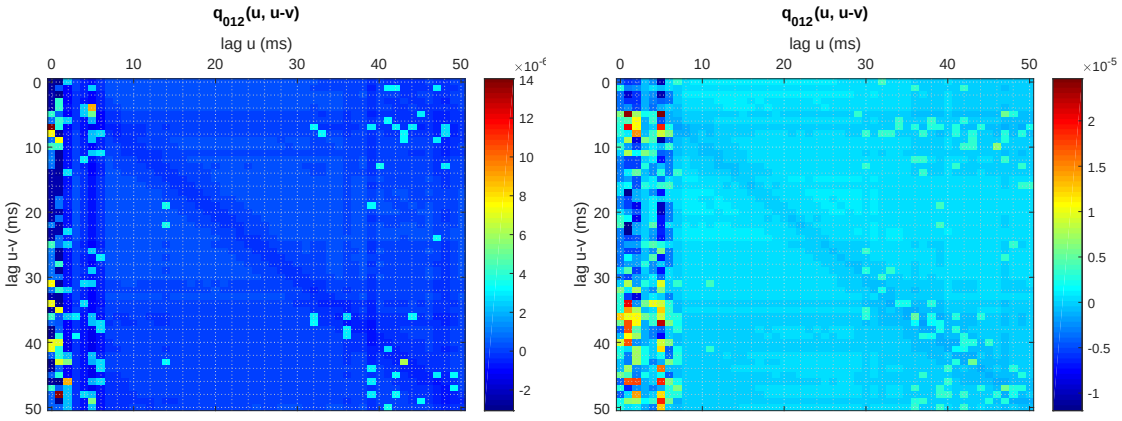

(a) N_0:sp13, N_1:sp1, N_2:sp3

(b) N_0:sp13, N_1:sp1, N_2:sp5

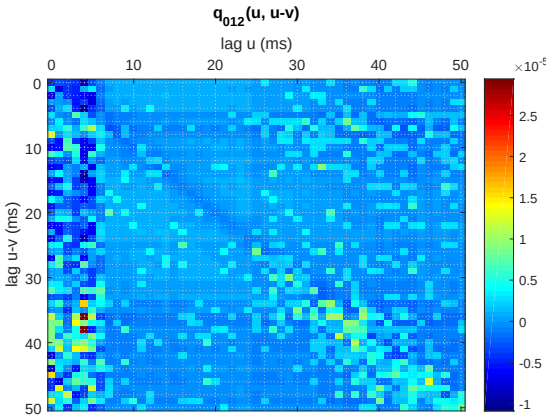

(c) N_0:sp13, N_1:sp1, N_2:sp6

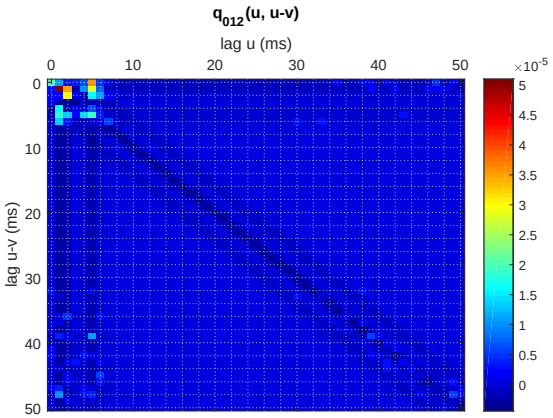

(d) N_0:sp13, N_1:sp3, N_2:sp5

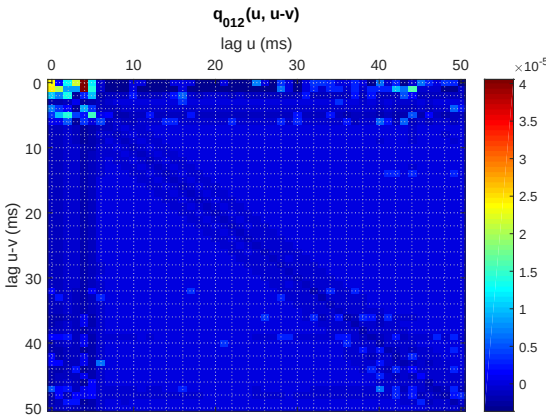

(e) N_0:sp13, N_1:sp3, N_2:sp6

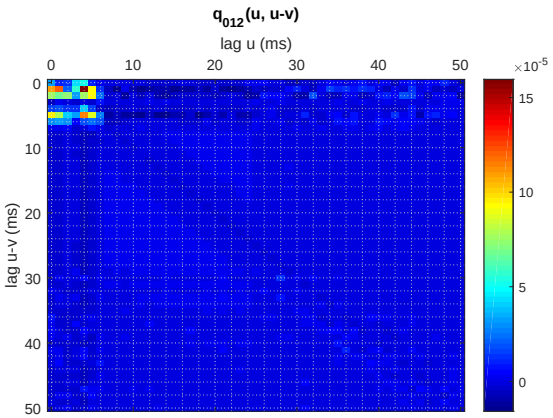

(f) N_0:sp13, N_1:sp5, N_2:sp6

Figure 4.29: Third order cumulant density estimates of the hippocampal data (see section 4.2).

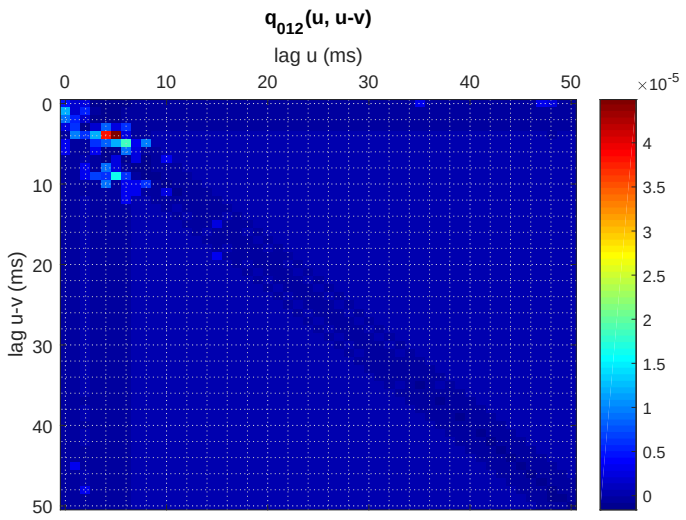

(a) N_0:sp17, N_1:sp14, N_2:sp15

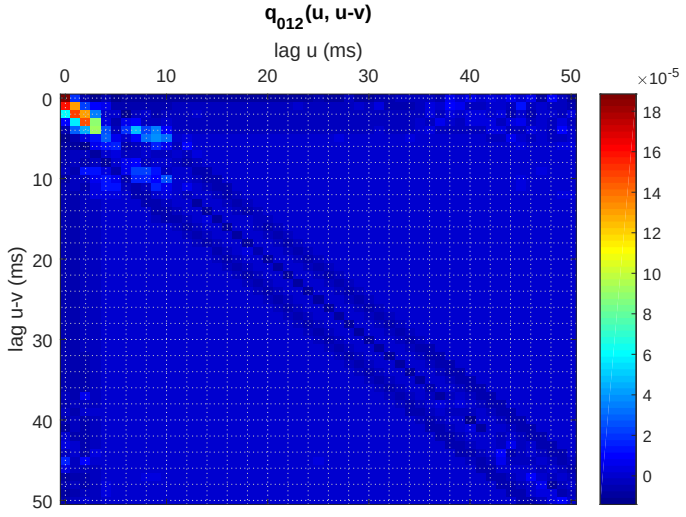

(b) N_0:sp17, N_1:sp14, N_2:sp16

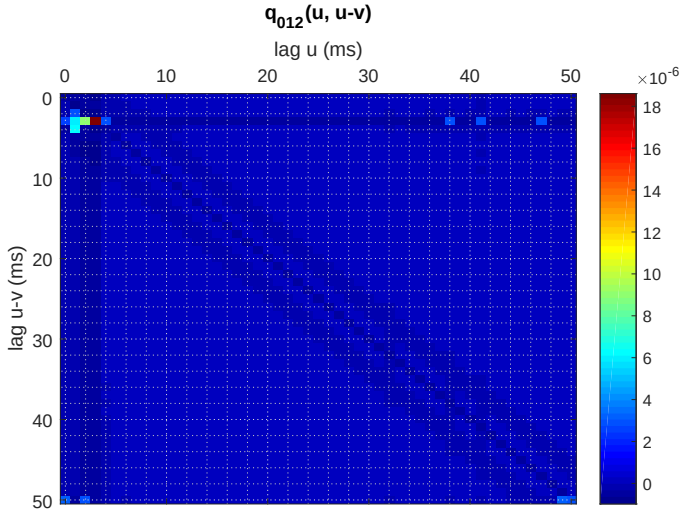

(c) N_0:sp18, N_1:sp14, N_2:sp16

Figure 4.30: Third order cumulant density estimates of the hippocampal data (see section 4.2).

4.6 Conclusion

The UTO analysis framework for neural spike train signals is developed in this chapter. This framework provides flexible access starting either from time domain or frequency domain and avoids the calculation of the second order terms. The framework is applied to artificial generated dataset, simulated neuronal framework using point-cortical spiking neuron model and experimental MEA spike trains. The dependencies in the artificial data are successfully detected by the framework. In the spiking neuron model case, the UTO proves useful to reveal the connectivities between presynaptic and postsynaptic neurons. In the experimental data case, two main interaction patterns are identified by using the proposed framework. One is significant third order interactions with the short lags (about $[0, 10]\ ms$) on both u and $u\ -\ v$ axes (for example, figure 4.24). The other is significant third order cumulants found on short lag u (about $[0, 10]\ ms$) but existing on both short and large $u\ -\ v$ lags (about $[32, 48]\ ms$) (for example, figure 4.21). The results provide insights into the third order interaction patterns based on the "CA3-CA1" information flow mechanism in the hippocampus: the first pattern is that two CA3 spikes are highly likely to facilitate the CA1 neuron firing a short time aftewards, and the second pattern is that a short latency in conjunction with a long latency between CA3 spikes and a CA1 spike can also enhance the firing probability of CA1 neuron.

Chapter 5. Mutual Information Analysis

Contents

5.1 Introduction

Given two time series $\{X(t)\} = \{x(t_1),\ x(t_2),\ x(t_3),\ ...,\ x(t_n)\}$ and $\{Y(t)\} = \{y(t_1),\ y(t_2),\ y(t_3),\ ...,\ y(t_n)\}$, their Mutual Information (MI) is a metric to quantify the statistical dependence between the two series (Cover and Thomas, 2012). There has been substantial developments of the theory and estimation techniques since it was first proposed by Shannon (Shannon and Weaver, 1949) to measure the average number of units of $\{X\}$ which could be predicted by considering $\{Y\}$ (see section 3.5) (Moon et al., 1995b; Fraser and Swinney, 1986; Darbellay et al., 1999; Walters-Williams and Li, 2009). Since MI is a probability-based metric which does not require the assumption of linearity, it is potentially capable of capturing universal dependencies beyond linear measures. Nonlinear dependencies are often observed in nervous system, which makes MI a suitable measurement.

In this chapter, a scheme of generating MI to be a function of time lag u will be presented in section 5.2. The MI at every single lag is going to be estimated using

the k-th nearest neighbour statistics method (Kraskov et al., 2004) combined with a spike train preprocessing. Some results for MI analyses for simulated network data (see section 4.4.2) and experimental data (see section4.2) will be discussed in section 5.3 and section 5.4 respectively.

5.2 Mutual Information Function

5.2.1 Mutual Information Function

Recall that MI $I(X,Y)$ between two random variable X and Y is mathematically defined as equation (3.37) and equation (3.38) for the case when X and Y are both discrete and both continuous, respectively. It is also defined as (Cover and Thomas, 2012):

$$I(X,Y) = H(X) + H(Y) - H(X,Y) \tag{5.1}$$

where $H(X)$, $H(Y)$ are entropies of X and Y and $H(X,Y)$ are joint entropy of these two random variables (see equations (3.34) and (3.35)).

Time series are collections of random variables indexed in the order they occurred. The concept of MI could be generalised to investigate the dependence between two time series $\{X(t)\}$ and $\{Y(t)\}$ by introducing a lag variable u and measuring:

$$I(u) = I(X(t), Y(t+u)) \tag{5.2}$$

at each lag u (Cellucci et al., 2005; Guha, 2006).

Two spike trains which record spiking times will be considered. To conduct MI analysis on these two series can suffer from several problems. Usually, the two series are of different length, which makes alignment fail. However, if the two series are transferred

to point processes with the same length, then direct methods based on measuring the binary "words" distribution could be adopted (Strong et al., 1998). This estimator needs large amounts of data. In this thesis, another way to estimate MI between spike trains is proposed.

Let the spike train with lower number of spikes be denoted as N_l and the spike train with higher number of spikes be denoted as N_h (see figure 5.1). $X(n)$ is the series recording the firing time of N_l, and N_l contains n_l spikes, hence the duration of inter-spike interval (ISI) of N_l is:

$$\Delta t(n) = X(n+1) - X(n) \tag{5.3}$$

where $n = 1, 2, ..., n_l - 1$. Let $r(n)$ be the local firing rate of N_h, defined as the number of spikes of N_h during N_l ISI $[X(n),\ X(n+1))$, $c(n)$, normalised over the corresponding ISI duration $\Delta t(n)$:

$$r(n) = \frac{c(n)}{\Delta t(n)} \tag{5.4}$$

where $n = 1, 2, ..., n_l - 1$. In this way, the alignment of the two original series are maintained in $r(n)$ and $\Delta t(n)$, and the length of the two newly-obtained series are the same.

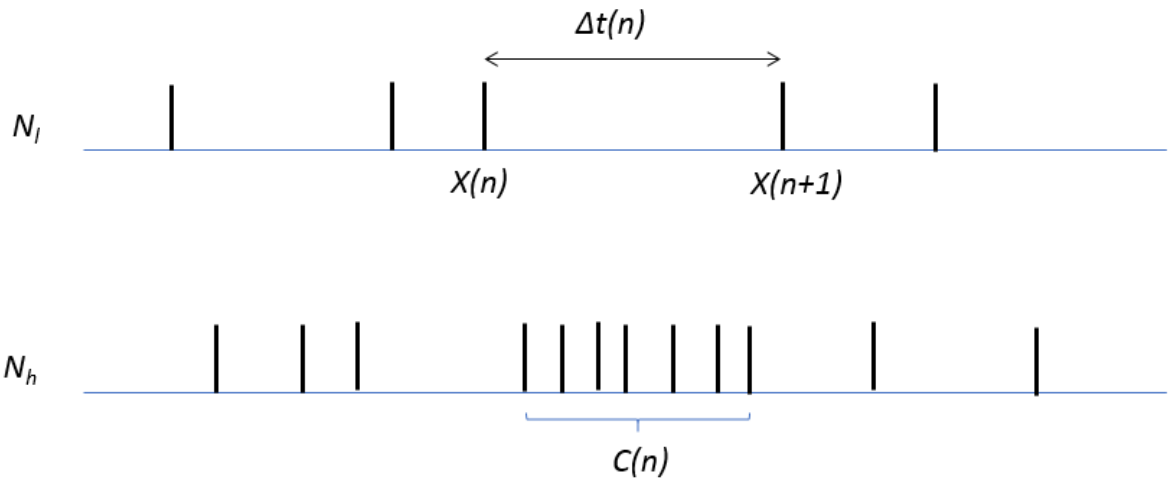

Figure 5.1: Schematic representation of the transformation of two spike trains to two series with the same length.

The entropy terms in equation (5.1) are estimated from k-th nearest neighbour statistics reviewed in section 3.5 using equations (3.47) to (3.53). For each lag u introduced, the estimated MI is constructed using the entropy terms.

5.2.2 Baseline Construction associated with the Proposed MIF

The estimated MIF values need to be tested against the baseline which indicates no dependent relationship existing between the two spike trains under investigation if the estimated MIF values are below the baseline. The baseline is obtained using artificial Poisson spike trains (see section 4.4.1). Two spike trains from spiking neuron model or real experiment are taken into account, for the consistent fashion, denoted as N_l and N_h. Suppose the numbers of spikes in N_l and in N_h are denoted as n_l and n_h respectively. The firing rates are approximately estimated as:

$$R_l = \frac{n_l}{R} \tag{5.5}$$

$$R_h = \frac{n_h}{R} \tag{5.6}$$

where R is the recording length of time. Two artificial Poisson spike trains with the firing rates R_l and R_h are generated, denoted as N_{pl} and N_{ph}. Therefore, the artificial Poisson spike trains and the two spike trains under investigation have the same firing rates. After the two Poisson spike trains are generated, the proposed MIF of N_{pl} and N_{ph} is calculated at the same lag interval.

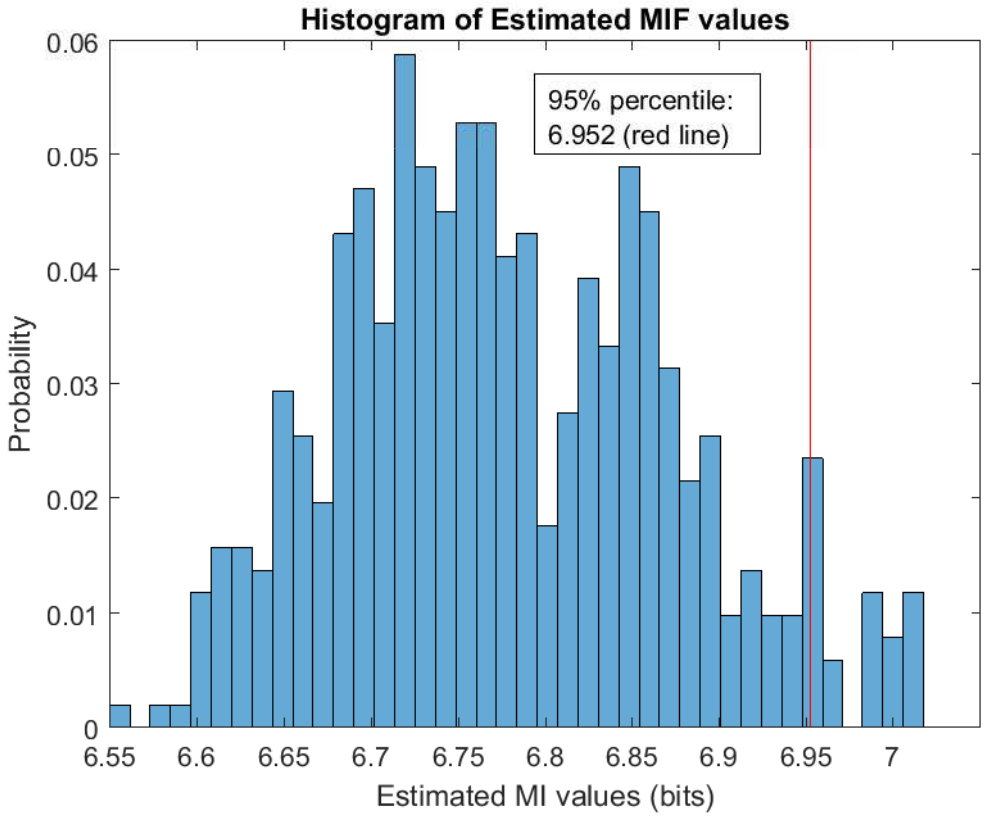

Figure 5.2: Histogram of the MIF values of two Poisson spike trains on $[0,\ 50]\ ms$. The histogram is obtained by 200 trials. The vertical red line indicates the 95% percentile of the MIF values. In this case, the 95% percentile is at 6.952. The firing rates used in this case to generate two Poisson spike trains are $11.11\ spikes/sec$ and $21.08\ spikes/sec$, which are identical to the estimated firing rates of sp5 and sp10 in the experiment dataset (see section 4.2)

Calculating the baseline is a time consuming task because taking more trials of simulations can increase the reliability of the estimated 95% percentile value. Considering the trade-off between the computational efficiency and the reliability of the estimated baseline value, the trial of calculating the MIF of two Poisson spike trains are repeated 200 times, after which the distribution of the MIF values of all trials is approximated by a histogram.

Figure 5.2 shows an example of the normalised histogram of the estimated MIF values using 200 trials. The two Poisson spike trains used to construct this histogram have firing rate 11.11 $spikes/sec$ and 21.08 $spikes/sec$, which are identical to the sp5 and sp10 respectively in the experimental dataset (see section 4.2, table 4.3). The Main feature of this distribution is bimodal, at around 6.72 and 6.85. The overall shape is not heavily skew. The tails on both sides are comparably converging, which makes the estimated MIF values of the simulated Poisson spike trains well bounded. This is a good property to calibrate the estimated MIF values of the real experimental spike trains. The 95% percentile of this distribution is marked by the vertical red line at 6.952 bits which is used to construct the baseline. The baseline distinguishes that the MIF values beneath this line is highly likely to indicate the independence of the two spike trains, while the MIF values above it is a evidence of the dependence and interaction.

5.3 Mutual Information Function Analysis on Simulated Network

The MIF using k-th nearest estimation approach is presented in section 5.2. In this section, the evaluation of this approach is conducted by applying it to simulated neuronal network spike trains from 100 spiking neuron network using a point-cortical model (see section 2.7 and section 4.4.2). The centre-surrounded pattern adopted in this simulated network is taken into account by considering the configurations that the postsynaptic neuron is fixed, and the distances between the presynaptic and postsynaptic neuron are gradually increased. The MIF of the presynaptic and postsynaptic neurons are investigated in each pair. As the relative distance between the presynaptic and postsynaptica neurons increase, the dependency between the two spike trains is likely dropping gradually, which is implied by the estimated MIF values and the areas on which the MIF values depart from the baseline.

Figure 5.3 shows the result for MIF analysis of presynaptic and postsynaptic neurons

which are spatially close to each other. The postsynaptic neuron is at position 55 while the presynaptic neuron is at 45 (see figure 4.13) which has excitatory effect directly onto neuron 55. The estimated MI at each lag u is plotted in figure 5.3. In each plot, the dashed black line is the baseline indicating there is not any dependency between the two spike trains under investigation (see section 5.2). This baseline is calculated by 200 trials of applying the MIF to two Poisson spike trains (see section 4.4.1) whose firing rates are identical to the two real spike trains. Plots 5.3 (a) and 5.3 (b) show similar areas $[0,\ 20]\ ms$ where the estimated MI values significantly depart from the baseline. MI values over lags close to $0\ ms$ are significant, which agrees with the close position of these two neurons. The peak of the estimated MIF occurs near $u = 6\ ms$ in both plots. One interpretation is that postsynaptic neuron 55 could be predicted by looking at the state of presynaptic neuron 45 from 0 to $22\ ms$ preceding to neuron 55. The best prediction could be made by investigating the state of neuron 45 at $6\ ms$ before neuron 55. Considering the central-surrounded pattern and the direct excitatory connectivity between neurons, the strong MI values over short duration are consistent with this expectation. The two plots use different numbers k of nearest points. The top panel (a) is estimated using $k = 5$ and the bottom panel (b) is estimated using $k = 10$. It is noticed that the local maximals and minimals in each plot are similar. However, the estimated curve in the bottom panel seems comparably smoother because of more nearest points used.

Figure 5.4 shows the result for MIF analysis of presynaptic and postsynaptic neurons with a bigger spatial separation. Neuron 55 remains the postsynaptic neuron and presynaptic neuron is at 35 (see figure 4.13). According to the center-surrounded pattern, the excitatory connectivity between neuron 35 and 55 still exists. In this case, the intervals of lag u indicating significant dependencies lay on $[0,\ 12]$ in plot (a) and $[0,\ 13]$ in plot (b), which are shorter compared with figure 5.3. The significant MIF values imply that inspecting the state of the presynaptic neuron 35 could be useful to reduce the uncertainty of the state of postsynaptic neuron 55 about 0 to $12\ ms$ afterwards. The shorter duration of significant values are reasonable due to the longer distance between the two neurons. It is worth noticing that in this case, the values below the baseline in plot (b) behave more consistently while the corresponding part in plot (a) fluctuates a

bit more randomly.

Figure 5.5 is the results for another pair of neurons with longer distance and inhibitory connectivity between them. In this case, the presynaptic neuron 25 has an inhibitory effect on the postsynaptic neuron 55 based on the centre-surrounded pattern of the inhibitory connectivity (see figure 4.13 (c)). The intervals where MIF values are larger than the baseline are divided in two sections, in which the MIF values are just above the baseline value. The dominant features in both plots (a) and (b) are a double-peak shape above the baseline. Each peak is of short duration. In addition to that the MIF values are just above the baseline, It may suggest weak inhibitory effect from neuron 25 onto neuron 55.

Moving the presynaptic neuron by 2 units further provides the pair of neurons 5 and 55. Considering the relative positions and the center-surrounded patterns described in section 4.4.2, there are not any excitatory or inhibitory connectivities between these two neurons. The analysis results are showed in figure 5.6. Almost all the estimated MIF values are below the baseline which indicating there are not any dependencies found. The values of the MIF at all lags behave randomly in both plot 5.6 (a) and 5.6 (b). There are discrete time values where the MIF values are higher than baseline in plot (a). However, their appearances are most likely by chance than indicating any real dependencies. The results suggest that there are unlikely to be any dependencies between spike trains from neuron 5 and from neuron 55. The uncertainty of one signal can not be reduced by investigating the other signal by any means.

In this section, the proposed MIF are evaluated by applying it to the simulated network. The results show the MIF is capable of measuring the interactions and dependencies between simulated spike trains using point-cortical spiking neuron model. In the next section, the approach will be further evaluated by applying it to the MEA spike trains.

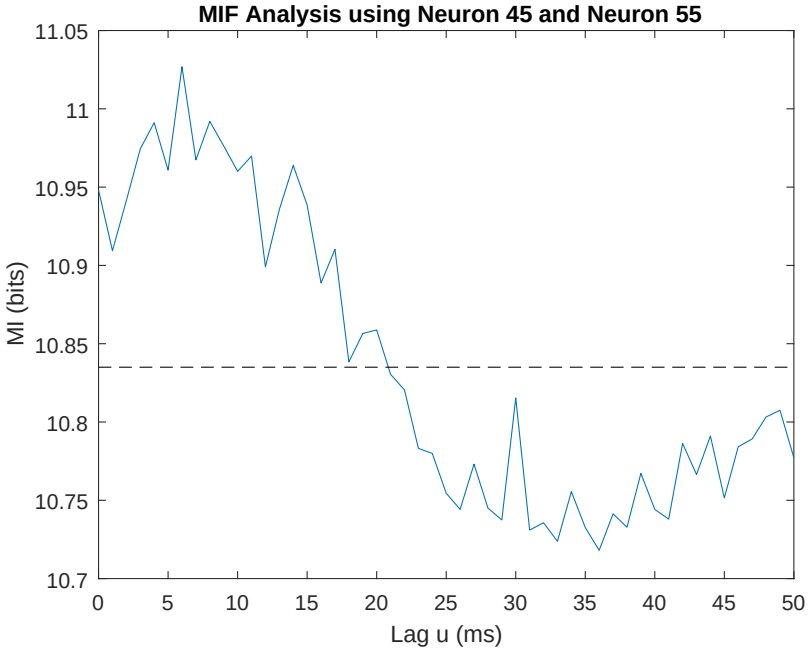

(a) MI in bits, $k = 5$.

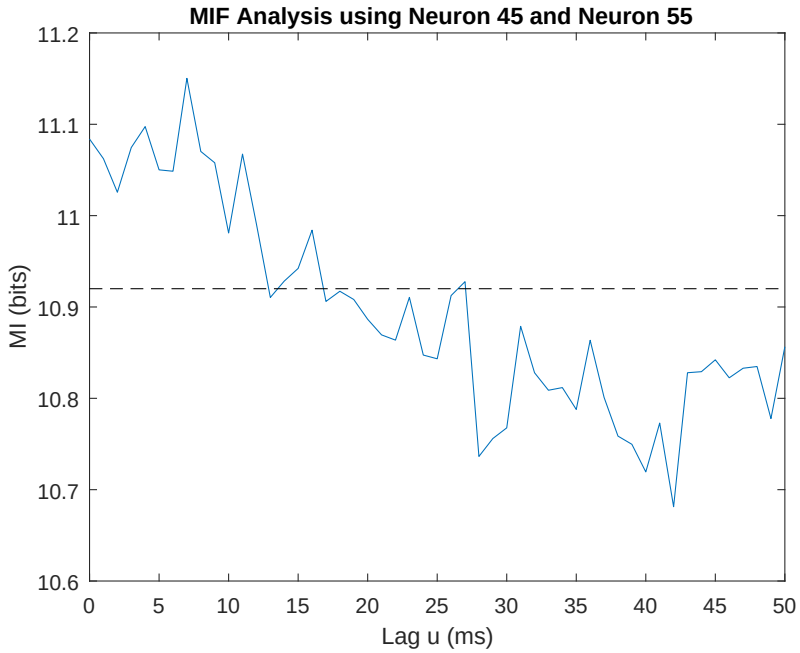

(b) MI in bits, $k = 10$.

Figure 5.3: The results for MI analysis using the proposed methods (k-th nearest estimate). The top panel (a) is the estimated MI as a function $I(u)$ against time lag u, $k = 5$. The bottom panel (b) shows estimated MI of the same signal pair with $k = 10$

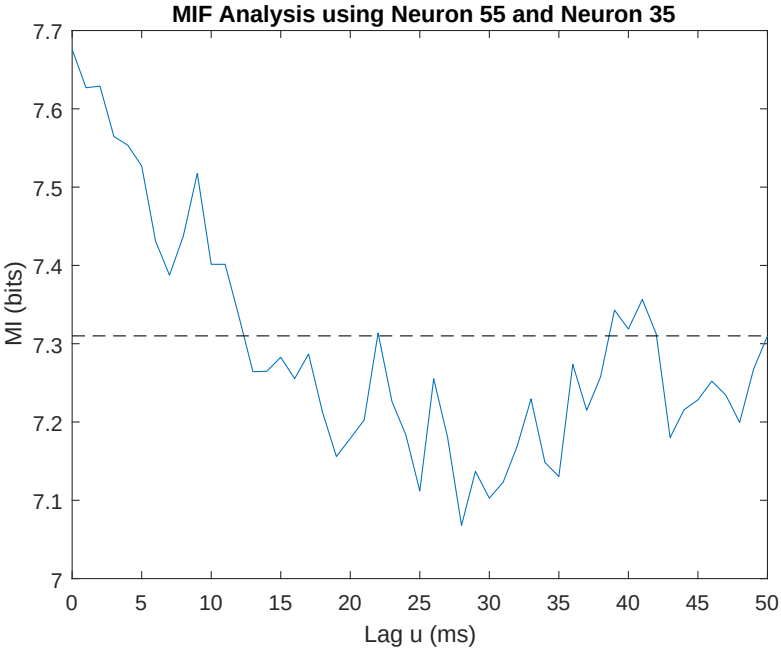

(a) MI in bits, $k = 5$.

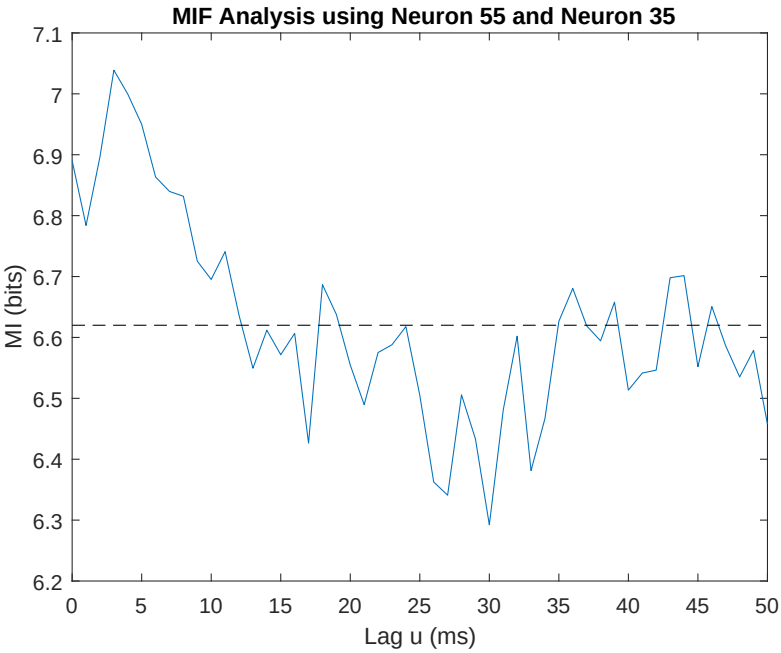

(b) MI in bits, $k = 10$.

Figure 5.4: The results for MI analysis using the proposed methods (k-th nearest estimate). The top panel (a) is the estimated MI as a function $I(u)$ against time lag u, $k = 5$. The bottom panel (b) shows estimated MI of the same signal pair with $k = 10$

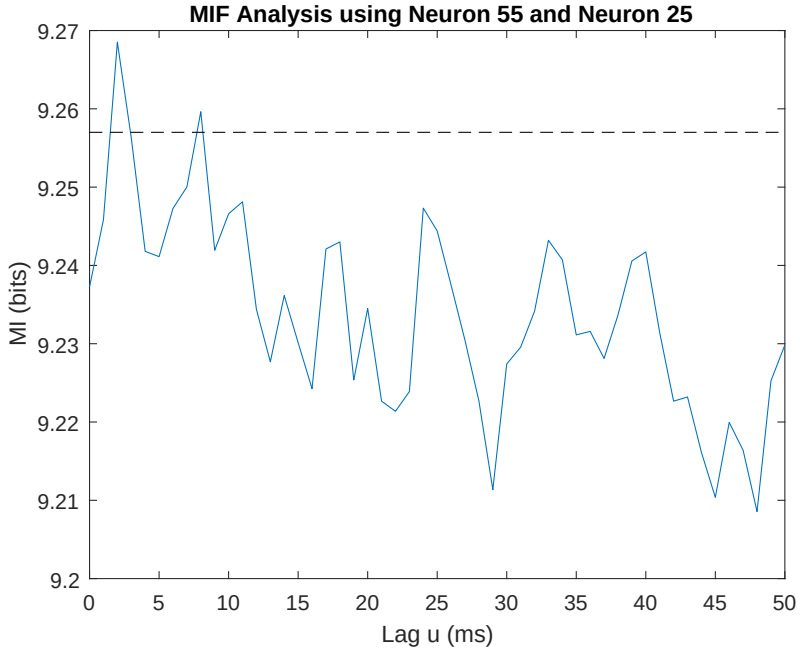

(a) MI in bits, $k = 5$.

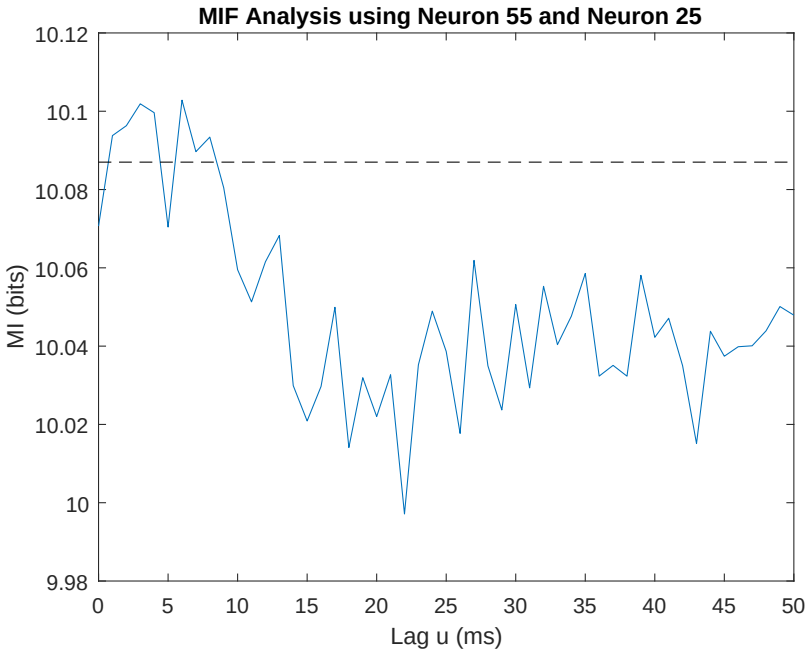

(b) MI in bits, $k = 10$.

Figure 5.5: The results for MI analysis using the proposed methods (k-th nearest estimate). The top panel (a) is the estimated MI as a function $I(u)$ against time lag u, $k = 5$. The bottom panel (b) shows estimated MI of the same signal pair with $k = 10$

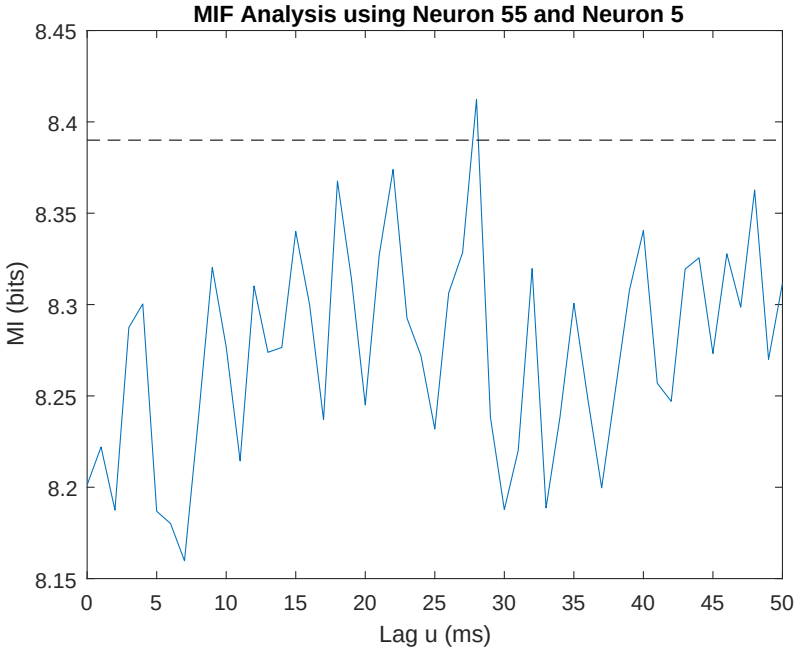

(a) MI in bits, $k = 5$.

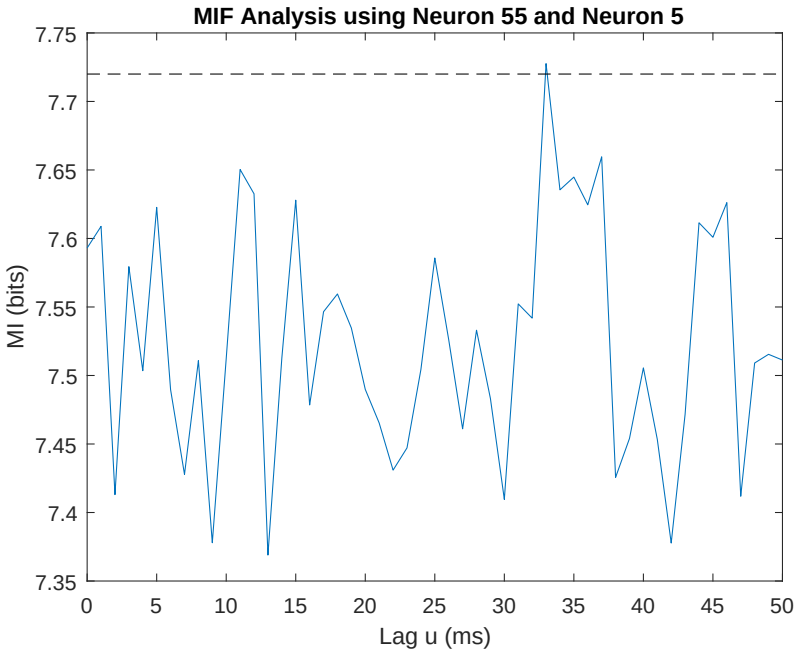

(b) MI in bits, $k = 10$.

Figure 5.6: The results for MI analysis using the proposed methods (k-th nearest estimate). The top panel (a) is the estimated MI as a function $I(u)$ against time lag u, $k = 5$. The bottom panel (b) shows estimated MI of the same signal pair with $k = 10$

5.4 Mutual Information Function Analysis on Experimental Data

The MIF using k-th nearest estimation approach is applied to simulated neuronal network spike trains in section 5.3. The results for the simulated data successfully reveal the connectivities between presynaptic and postsynaptic neurons. In this section, the evaluation of this approach will be continued by using it to study dependencies between the MEA single unit spike trains (see section 4.2). Two detailed examples will be illustrated first, followed by a systematic investigation of the experimental dataset using MIF. Comparison between MIF and second- and third- order approaches will be conducted.

Figure 5.7 shows the estimated MIF $I(u)$ between sp1 and sp10 (see table 4.2). The spike train sp1 is from left CA3 subregion with firing rate $17.47 spikes/s$. The spike train sp10 is from left CA1 subregion with firing rate $21.08 spikes/s$. In each plot, the dashed black line is the baseline indicating there is not any dependency between the two spike trains under investigation. This baseline is calculated in the same way as described in section 5.2. Plots 5.7 (a) and 5.7 (b) both show strong dependency over the lag u interval $[0,\ 15]$. The peak of the estimated MIF occurs around $u = 5\ ms$ in both plots. Some secondary features at large lag values can be identified in both plots. The estimated MIF values in the some intervals between $[30,\ 45]$ also depart from the baseline in both plots. It could be argued that there is a causal relationship between sp1 and sp10 with the former providing information to predict the state of the latter $[0,\ 15]$ ms afterwards. It is consistent with the "CA3 - CA1" information flow pattern in hippocampus. The two plots use different numbers k of nearest points. The top panel (a) is estimated using $k\ =\ 5$ and the bottom panel (b) is estimated using $k\ =\ 10$. It is noticed that the estimated MIF is sensitive to the choice of k value in this case as the shapes of the two MIF curve are slightly different.

Figure 5.8 shows the result for the pair of sp5 and sp10. The spike train sp5 is from

left CA3 subregion with firing rate $11.11\ spikes/sec$. The shape of the estimated MIF in this case is similar to figure 5.7. The interval of significant MIF values is $[0, 10]\ ms$ which is shorter duration compared with figure 5.7. Plots (a) and (b) both show strong dependency over the lag u interval $[0,\ 10]\ ms$. Clear secondary features on the lag u interval $[33,\ 40]\ ms$ and $[43,\ 46]\ ms$ could be found in plot (a). The strong dependencies in this case could also be explained by the "CA3 - CA1" information mechanism. In the plot (b), the second feature occurs on a continuous interval about $[36,\ 44]\ ms$, which is slightly different to plot (a).

Figure 5.9 to 5.10 shows some MIF analysis results for the "CA3 - CA1" pair spike trains across this experimental data. Almost all the figures show a significant area on short delays about $[0,\ 10]\ ms$. The maximum of the estimated MIF value are mostly located at $u\ <\ 5\ ms$, which are consistent with the results from TOF analysis. This may suggest that the spike trains from CA3 subregion is highly likely to carry the information which is needed to predict the state of spiking neuron in CA1 subregion a few milliseconds afterwards. It can be used as the proof of dependence between the two spike trains. Some of the pairs have secondary feature found around $[35,\ 45]\ ms$ (for example, figure 5.9 (a) and (b)) or $[20,\ 25]\ ms$ (for example, figure 5.10 (a)), which indicates that there may be another interaction pattern existing in such "CA3 - CA1" pairs.

It is worthy of noticing that the estimated MIF shows a section of constant values in some cases, for example, the flat section during $[8,\ 31]\ ms$ in figure 5.9 (c) and the flat section during $[9,\ 26]\ ms$ in figure 5.9 (e). These flat sections may result from the imbalance of firing times in the spike trains taken into account. According to figure 5.1 and equation (5.2), due to the imbalance of the spiking times of the spike trains, there is possibility that for several continuous lags u, the number of spikes $c(n)$ of N_h located in the corresponding ISI of N_l remain the same, thus, the local firing rate, $r(n)$, for each ISI, $\Delta t(n)$, remain unchanged (see figure 5.1). That is to say the preprocessing proposed in section 5.2 may generate two identical series $\Delta t(n)$ and $c(n)$ for these u, which leads to the constant values of the estimated MIF in those sections.

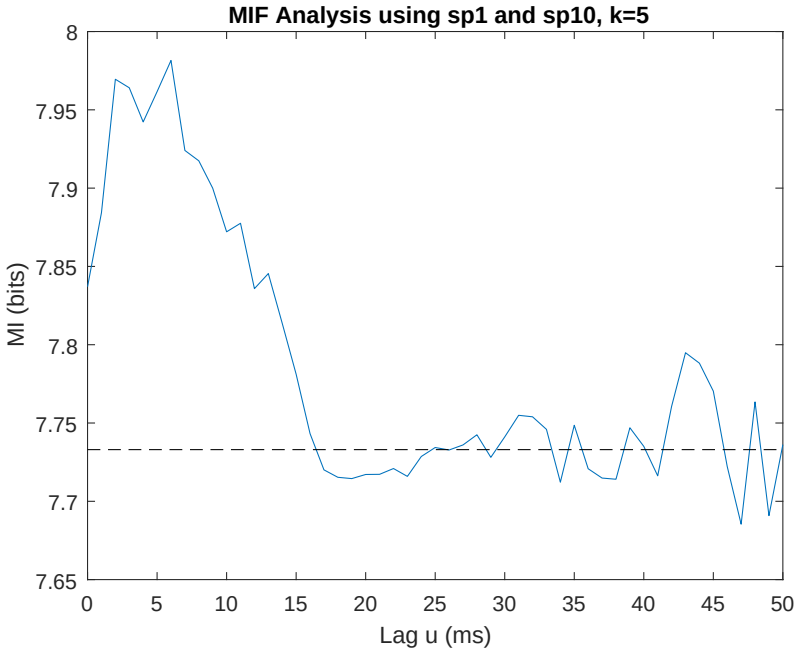

(a) MI in bits, $k = 5$.

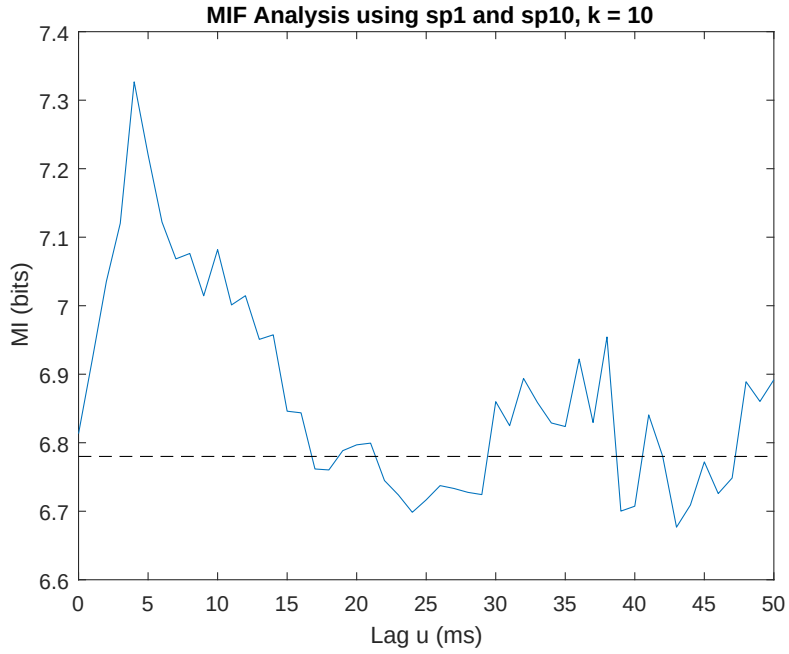

(b) MI in bits, $k = 10$.

Figure 5.7: The results for MI analysis using the proposed methods (k-th nearest estimate). The top panel (a) is the estimated MI as a function $I(u)$ against time lag u, $k = 5$. The bottom panel (b) shows estimated MI of the same signal pair with $k = 10$

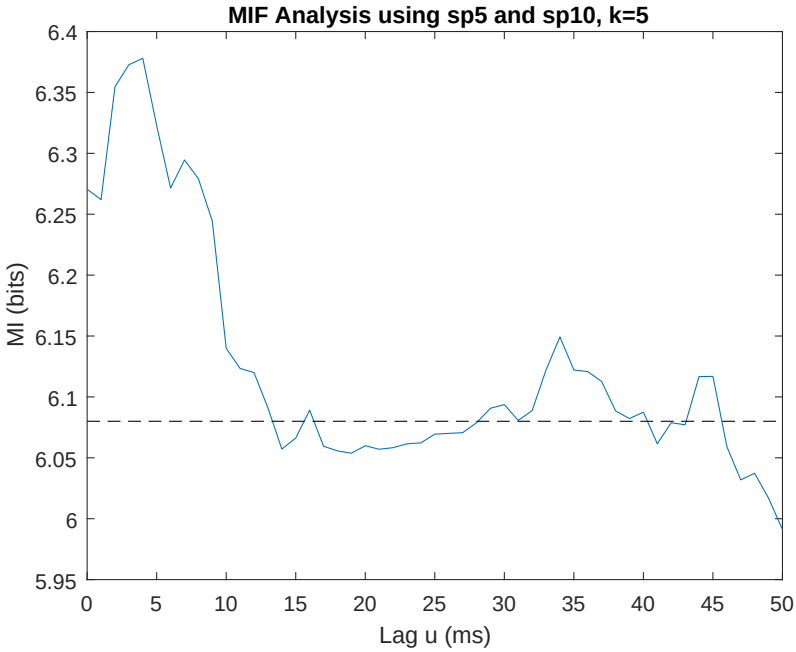

(a) MI in bits, $k = 5$.

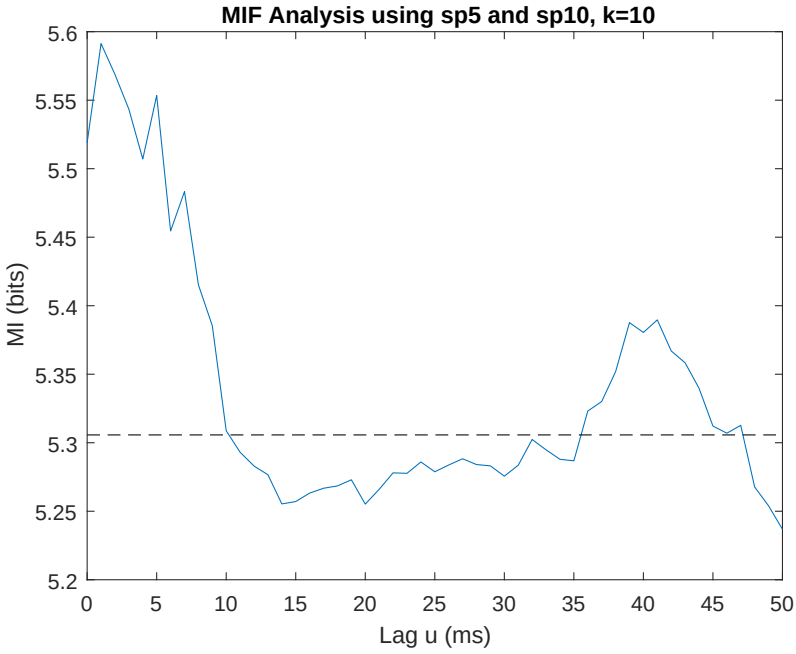

(b) MI in bits, $k = 10$.

Figure 5.8: The results for MI analysis using the proposed methods (k-th nearest estimate). The top panel (a) is the estimated MI as a function $I(u)$ against time lag u, $k = 5$. The bottom panel (b) shows estimated MI of the same signal pair with $k = 10$

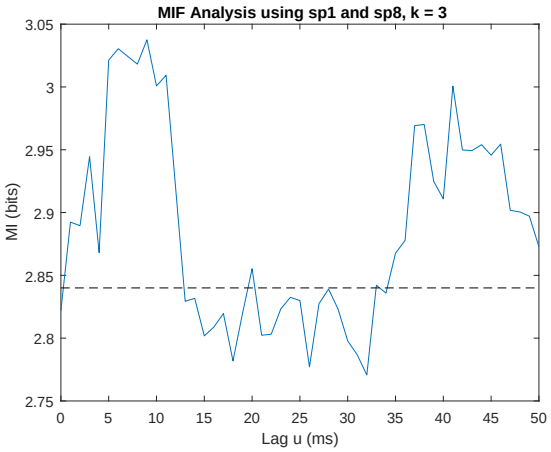

(a) MIF analysis using sp1 and sp8

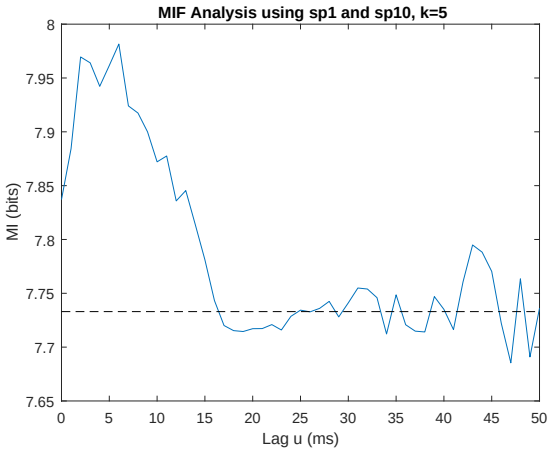

(b) MIF analysis using sp1 and sp10

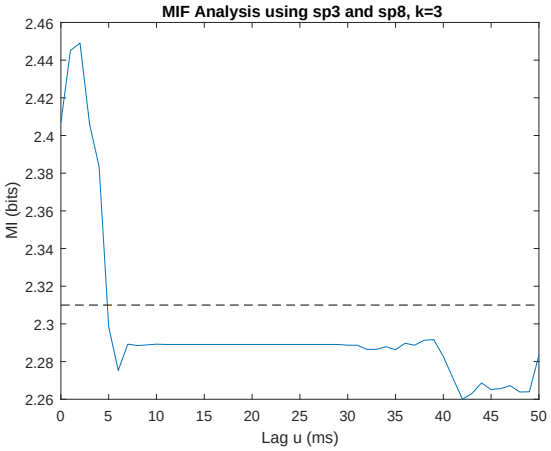

(c) MIF analysis using sp3 and sp8

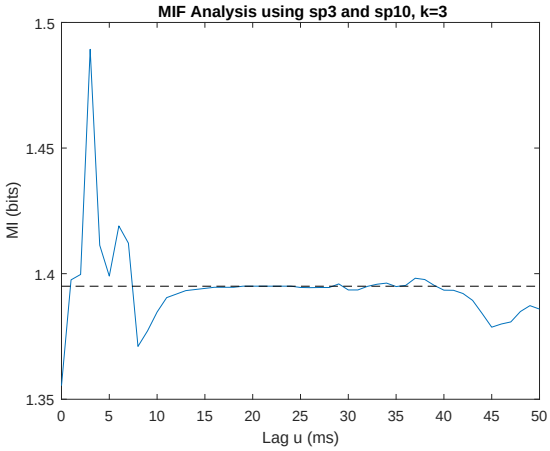

(d) MIF analysis using sp3 and sp10

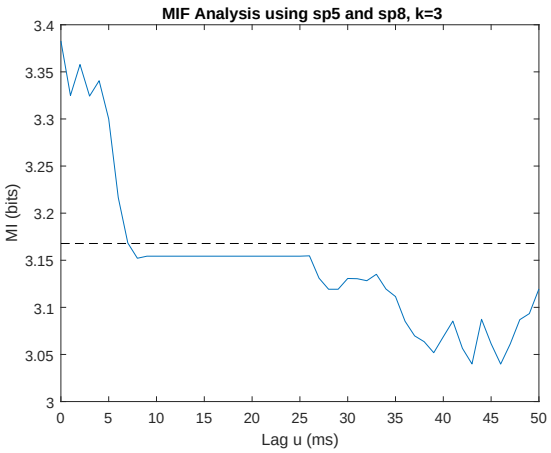

(e) MIF analysis using sp5 and sp8

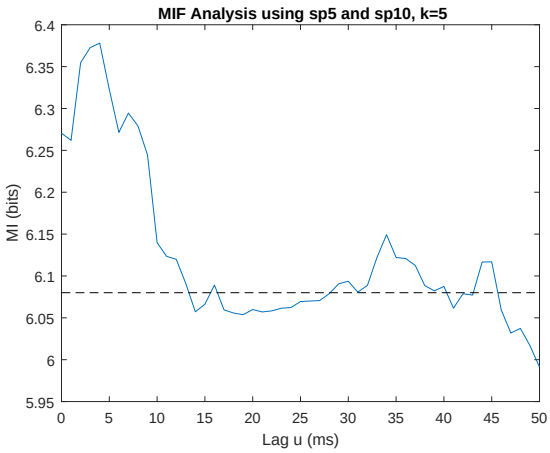

(f) MIF analysis using sp5 and sp10

Figure 5.9: MIF estimates of the hippocampal data (see section 4.2).

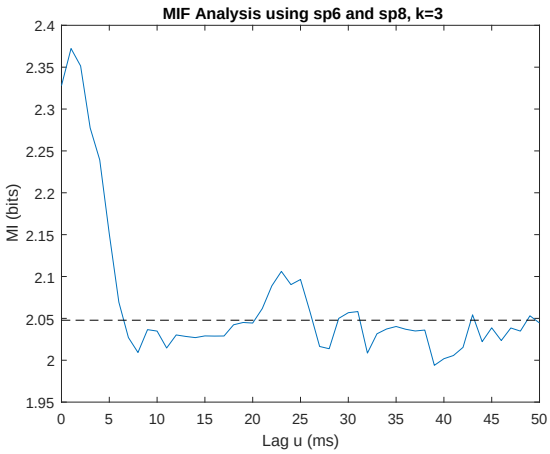

(a) MIF analysis using sp6 and sp8

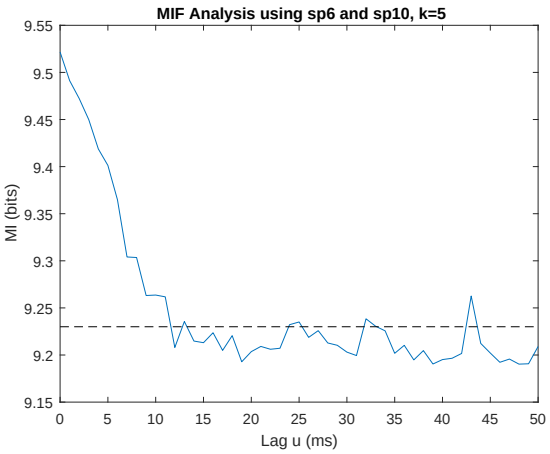

(b) MIF analysis using sp6 and sp10

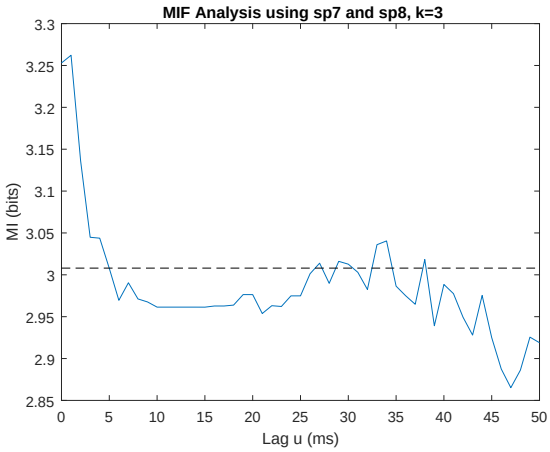

(c) MIF analysis using sp7 and sp8

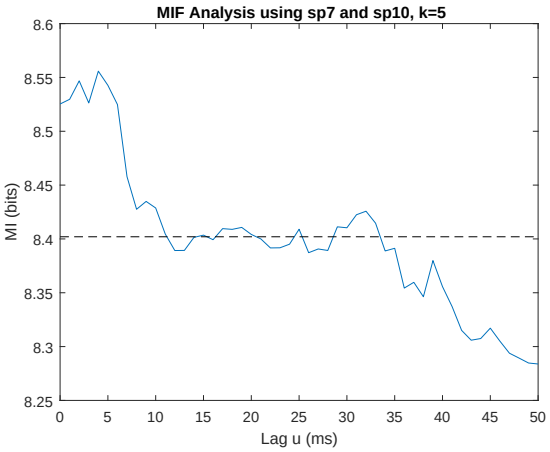

(d) MIF analysis using sp7 and sp10

Figure 5.10: MIF estimates of the hippocampal data (see section 4.2).

Figure 5.11 shows the comparison between the estimated MIF values and second order cumulant density (see section 3.2) analyses for the "CA3 - CA1" pair sp1 and sp8 (see tables 4.2 and 4.3)on the same lag range $[0,\ 50]\ ms$. In this case, In addition to the short latency interval $[0,\ 12]\ ms$, the second order cumulant density also captures another interval $[35,\ 45]\ ms$ with significant cumulant density values above the upper confidence limit. Figure 5.11 (b) shows the estimated MIF over the same range of lags. The double-peak feature is also captured, which is consistent with the second order cumulant density. The long latency area indicating dependency in plot (b) is wider compared with plot (a). The result may suggest that there are linear dependencies between sp1 and sp8 in the both short ($[0,\ 12]\ ms$) and long latencies($[35,\ 45]\ ms$) intervals. Nonlinear dependency may also exist in the long latency interval since the secondary peak in plot (b) is wider (up to $u = 50\ ms$) than in plot (a).

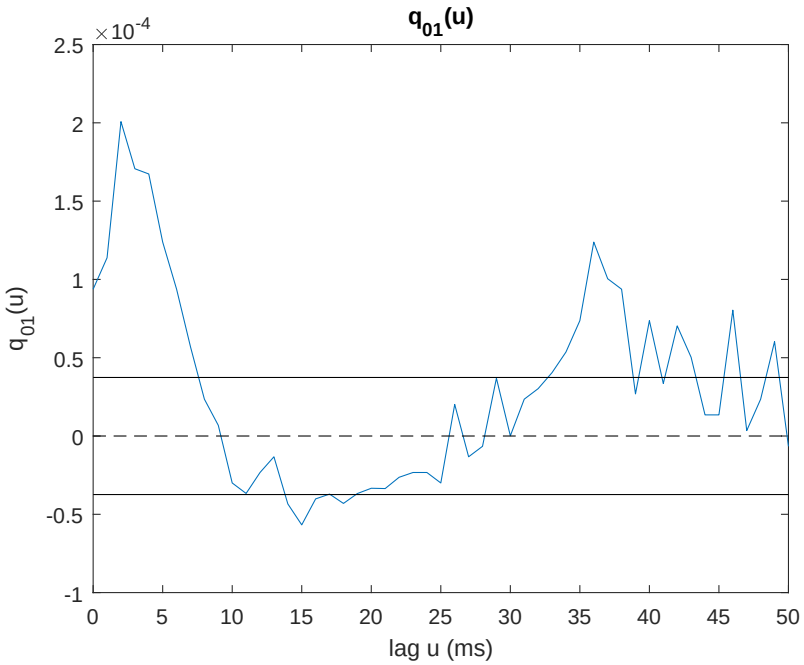

(a) Estimated second order cumulant density of sp1 and sp8.

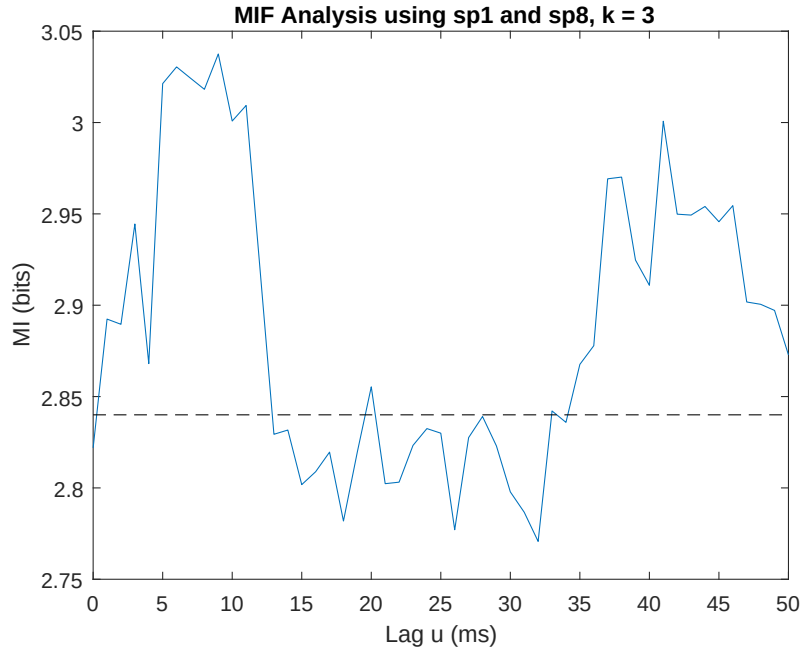

(b) Estimated MIF of sp1 and sp8 .

Figure 5.11: The comparison of MIF and second order cumulant density of sp1 and sp8. The top panel (a) shows the estimated second order cumulant density. The bottom panel (b) is the estimated MI as a function $I(u)$ against time lag u, $k = 3$ of the same signals. Both plots show two areas of features: around $[0,\ 12]\ ms$ and $[35,\ 45]\ ms$.

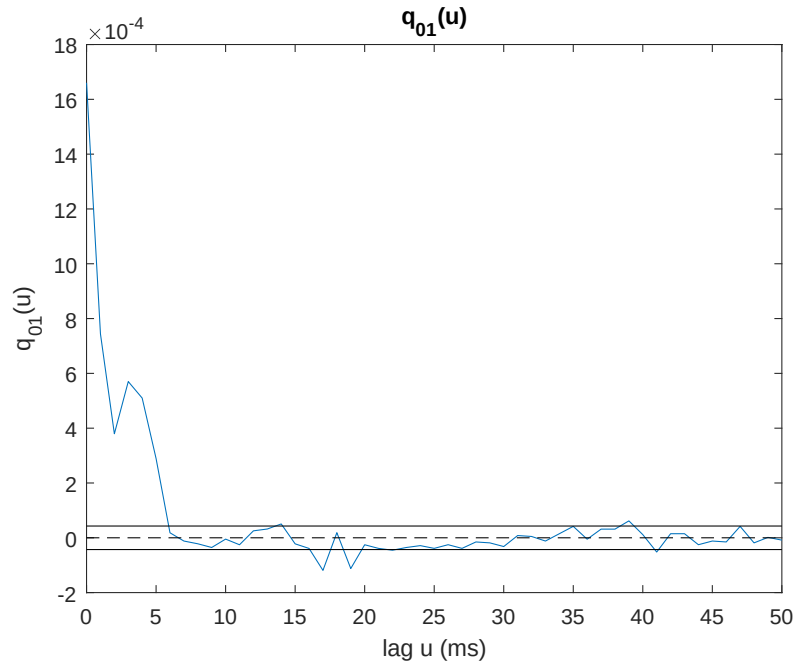

(a) Estimated second order cumulant density of sp6 and sp8.

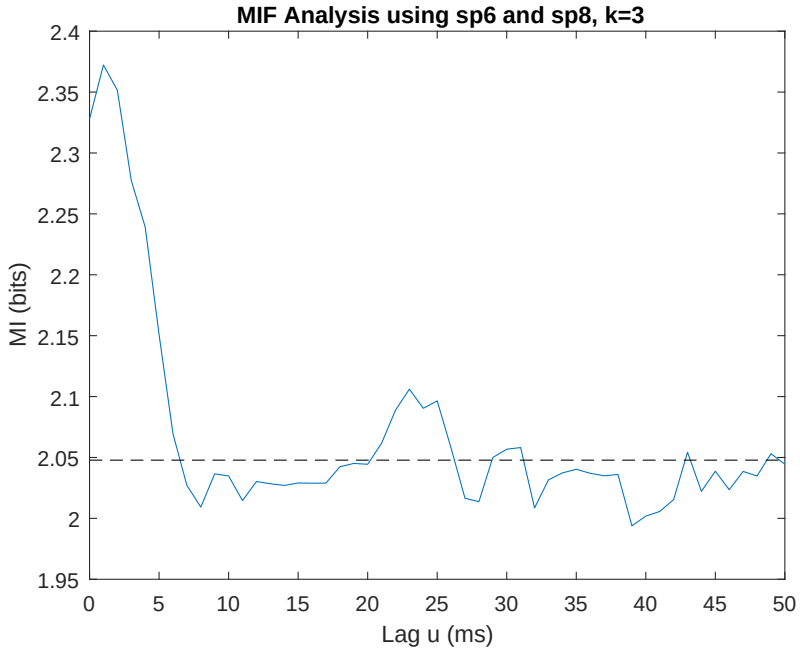

(b) Estimated MIF of sp6 and sp8 .

Figure 5.12: The comparison of MIF and second order cumulant density of sp6 and sp8. The top panel (a) shows the estimated second order cumulant density, which has only short lags with $[0,\ 5]\ ms$ indicating dependency between the spike trains. The bottom panel (b) is the estimated MI as a function $I(u)$ against time lag u, $k = 3$ of the same signals, which shows two areas of features: around $[0,\ 6]\ ms$ and $[20,\ 26]\ ms$.

Figure 5.12 shows another example of comparison between second order measurement and MIF. In the case, sp6 and sp8 are taken into account (see tables 4.2 and 4.3). The

estimated second order cumulant density shows a strong peak in the interval $[0,\ 5]\ ms$, apart from that, in the rest range of lags, the cumulant density is almost bounded with the confidence limits. In contrast, the MIF value reveals a secondary feature on $u = [21,\ 27]\ ms$ in addition to the similar short latency interval $[0,\ 6]\ ms$. Since the second significant area is absent in the cumulant density. This may suggest that there is nonlinear dependency between sp6 and sp8 corresponding to the interval $u = [21,\ 27]\ ms$.

5.5 Conclusion

In this chapter, a novel approach using ISI and local firing rate to estimate the MI between two series is presented. This approach transfers the spiking times series with different length to two series with the same length and keeps the alignment of the two corresponding spike trains. Afterwards, the k-th nearest estimation is applied to these series to estimate MI at each lag u. The proposed approach are applied to the simulated neuronal network spike trains and the experimental spike trains. In the simulation case, dependencies which could imply the excitatory or inhibitory connections are revealed by the significant MIF values. In the experimental data case, strong dependencies consistent with the "CA3 - CA1" interaction pattern found in the subregions of hippocampus are detected using the proposed MIF measurement. In addition to widely found short latency interval which is around $[0,\ 10]\ ms$, some spike trains also shown a second area of MIF values located at longer latency intervals, for example, $[20,\ 25]\ ms$ and $[35,\ 50]\ ms$, above the baseline. Comparisons between estimated second order cumulant density and MIF may suggest that there are nonlinear dependencies between signals. Hence, MIF, along with UTO analysis framework and second order measurements provides a complementary tool to have insight into the dependent relationships between spike train signals.

Chapter 6. Conclusions and Future Work

Contents

6.1 General Summary

This project carries out research on applying signal processing approaches to neural spike train data. Interaction detection and dependencies between neurons are the focus of this project. The Unified framework of Third Order time and frequency Domain analysis (UTO) and Mutual Information Function (MIF) are proposed and applied to artificial and experimental spike train signals. The results obtained from the applications show that they are applicable and practical techniques.

This chapter will first generally summarise this project, and then make summaries and conclusions chapter by chapter in more detail. Limitations and future work will be discussed at last.

This thesis presents two approaches using spike train signals to detect the interactions and dependencies at the neuronal level. The Unified framework of Third Order time and frequency domain analysis (UTO) proves a reliable tool to quantify third order (non-linear) interactions and dependencies. This framework takes into account the flexibility by providing analysis access starting from either time domain or frequency domain. It also has well-established procedures to estimate confidence intervals, which is useful in hypothesis testing in the neuronal analysis application. UTO analysis was

applied to artificial generated data, simulated neuronal network data adopting central-surrounded feature and experimental recordings including 30 channels of spike trains from rat hippocampus.

Generalising Mutual Information (MI) to study the dependencies between spike trains provides a tool to reveal general dependencies beyond the linearity. Problems in estimating MI between spike trains are two fold. For one side, if the spiking times data is considered, the two series may be of different length and the alignment of the two signals is lost; on the other hand, if the actual "$0\ 1$" processes are used, the probabilistic estimation suffers from the requirement of large amounts of data. The proposed MIF using k-th nearest estimator overcomes these problem by transferring the two series of spiking times to an interspike interval (ISI) series and a local firing rate series. This data processing method combined with the k-th nearest probability density estimation approach provides a novel tool to view the dependency in a wider sense. The analyses using the proposed MIF to study simulated neuronal network signals and MEA single unit signals prove that MIF could facilitate the study of dependency in simultaneously recorded signals.

The novel contributions in this project come from unifying the third order measures in time domain and frequency domain, implementing a mutual information estimator and using these techniques to explore the dependencies in spike trains beyond the widely used linear measurements scope. Adopting third order analysis demonstrates a triplet interaction pattern existing between some neurons. Despite separated time and frequency domain methods, the unified framework provides flexible access and computational efficiency without calculating all lower order terms. The Mutual information is based on probability metrics and hence it measures the dependencies in universal sense without replying on the the assumption of linearity. Applying UTO analysis and MIF can provide more insight beyond the linear relationships between signals.

6.2 Chapter Summaries and Conclusions

Chapter 2 adopts a top-down view to describe the biological background of the nervous system. A brief description of the central nervous system and brain is presented. Since this project focuses on the cell level, neurons as the basic cell in the nervous system are described in detail. This chapter also reviews signalling properties in neurons and in synapses. Action potentials, also known as spikes, as the prototype of neuronal signalling are also reviewed. Since simulated neuronal networks play an important role in the verification of the techniques in this project, some spiking neuron models are presented in detail. Modelling of spiking neuronal network provides surrogate data which are useful in the evaluation of the proposed techniques. The experimental data used in this project are a 30 channel spike trains sorted from a Multielectrode Array (MEA) recording. Therefore, MEA techniques and the spike sorting procedure are discussed in this chapter as well.

Chapter 3 reviews several signal processing techniques which have applications in dependence analysis. The review of the dependence between spike trains starts with the most widely used correlation function in time domain. It is followed by a description of the disjoint Fourier Transform, the estimation of spectra and the computation of coherence. The final parts of this chapter review higher order statistics, information theory and mutual information used in signal processing area. The review in this chapter lays the foundation of the implementation of the proposed novel techniques in this thesis.

Chapter 4 presents the Unified Framework of Third Order Time and Frequency Domain Analysis (UTO) and the results for the application of this framework. The chapter begins with a brief description of the experimental data and the experiment which produces the spike train signals used in this project. It is followed by a detailed description of UTO analysis with theoretical core equations and estimation procedures. It is followed by the results for UTO analysis of simple artificial data, surrogate data generated by a simulated neuronal network and the experimental data, which shows

successful applications. In each application, the proposed framework detects the dependencies as expected. In the simulated neuronal network case, the framework yields estimates of the interactions between triplet neurons, which are consistent with the centre-surrounded pattern adopted in this network. In the experimental signal case, UTO analysis reveals interactions with short time lags and illustrates the typical interactions between CA3 neurons and CA1 neurons. The results also suggest that there are two patterns of third order interactions in hippocampus. One is that two input spikes with very short time difference from subregion CA3 facilitates the firing probability of neurons in CA1 after 5 to 10 ms . The other is that a 35 to 45 ms long time difference between the two input spikes from CA3 also increases the firing probability of neurons in CA1 subregion. These evaluations and findings prove the applicability of the proposed framework.

Chapter 5 presents the Mutual Information Function (MIF) developed in this project and reports the results for MIF analysis. The definition of the MIF and the corresponding estimating procedure are presented first, followed by the analysis results organised in the same way as in Chapter 4. In the simulated neuronal network case, the proposed MIF detects the dependencies which represent the excitatory or inhibitory connectivities between neurons. In the experimental MEA single unit spike train case, the MIF method indicates the dependencies which could be explained by the "CA3 - CA1" information flow pattern in hippocampus. In majority of the "CA3 - CA1" pairs, MIF shows significant values departing from the baseline on short delay range of $[0, 10]$ ms. For some pairs, there are secondary features found in the interval $[35,\ 45]$ ms. This may suggest that in hippocampus, the state of a spiking neuron in CA3 is useful to predicate the state of a spiking neuron in CA1.

6.3 Future Work

The goal of the study of neuronal dependencies is to deepen the understanding of the interaction patterns and dependencies between neurons. The applicability of the proposed third order framework and mutual information function is proved by the results

for surrogate data and MEA spike train signals. The usage of these techniques paves the way for a range of new points of research for exploration. The findings obtained by applying the proposed techniques are promising, which could potentially be the foundations for further development of more sophisticated and more robust estimators. The following are the suggestions for the future work.

1. One possible way in near future is to extend the Unified Framework of Third Order Time and Frequency Domain analysis (UTO) to suit the hybrid data (Halliday et al., 1995) which contains both point processes, for example spike trains, and continuous time series, for example EEG. The ability of handling hybrid data will enhance the feasibility of the framework since a wide range of neuronal data are formed by simultaneously recorded spike trains and time series, for example, tremor, LFP signals and spike trains. A framework capable of processing hybrid data will allow the exploration of the third order dependencies in such data.

2. According to the results obtained in this thesis, further study could potentially focus on the conditional or partial measurement which takes into account that neurons have background inputs as well as interactions with each other. Although the third order framework takes up to 3 neurons, it is not able to rule out the possibility that the dependency detected results from common background inputs rather than interactions among the three neurons. In the second order case, the partial measurements, for example, partial spectral and partial coherence are well established and provide starting point to carry out higher order partial measures estimate (Halliday et al., 1995), (Sun et al., 2004).

3. The estimate of mutual information always relies on the probability estimation since it is a probability based metric. Due to the special binary property of spike trains, estimation of the joint probability density is always problematic. Further research could potentially focus on the reliable estimation of probability densities. This thesis provides a way to transfer spike trains to some continuous series. Therefore, sophisticated estimators, such as kernel based methods and some parametric method (Hlaváčková-

Schindler et al., 2007), (Shlens et al., 2007) could be potentially considered in further research.

4. Mutual information also suffers from the problem of common inputs. Possible improvement might rely on the study of more sophisticated information theory related metric. Transfer entropy is reported to have the advantage to overcome the common inputs dilemma (Schreiber, 2000), which could potentially be another approach.

5. Higher order mutual information measurement is also a promising field worthy of paying attention to. The definition is intuitively direct based how the mutual information is defined in usually encountered two-variable case. However, as the dimension increases, the joint probability is more difficult to estimate. The data required to conduct a reliable estimation increase dramatically, as well as the computational cost.

References

Abramowitz, M. and Stegun, I. A. (1965). *Handbook of mathematical functions: with formulas, graphs, and mathematical tables*, volume 55. Courier Corporation.

Aertsen, A. M., Gerstein, G. L., Habib, M. K., and Palm, G. (1989). Dynamics of neuronal firing correlation: modulation of effective connectivity. *Journal of neurophysiology*, 61(5):900–917.

Alexander, G. E. and Crutcher, M. D. (1990). Functional architecture of basal ganglia circuits: neural substrates of parallel processing. *Trends in neurosciences*, 13(7):266–271.

Alexander, G. E., DeLong, M. R., and Strick, P. L. (1986). Parallel organization of functionally segregated circuits linking basal ganglia and cortex. *Annual review of neuroscience*, 9(1):357–381.

Ashburner, J. and Friston, K. J. (2000). Voxel-based morphometrythe methods. *Neuroimage*, 11(6):805–821.

Bartlett, M. (1963). The spectral analysis of point processes. *Journal of the Royal Statistical Society. Series B (Methodological)*, pages 264–296.

Benignus, V. et al. (1969). Estimation of the coherence spectrum and its confidence interval using the fast fourier transform. *Audio and Electroacoustics, IEEE Transactions on*, 17(2):145–150.

Biswal, B., Zerrin Yetkin, F., Haughton, V. M., and Hyde, J. S. (1995). Functional connectivity in the motor cortex of resting human brain using echo-planar mri. *Magnetic resonance in medicine*, 34(4):537–541.

Borst, A. and Theunissen, F. E. (1999). Information theory and neural coding. *Nature neuroscience*, 2(11):947–957.

Brazier, M. A. and Casby, J. U. (1952). Crosscorrelation and autocorrelation studies of electroencephalographic potentials. *Electroencephalography and clinical neurophysiology*, 4(2):201–211.

Brillinger, D. R. (1965). An introduction to polyspectra. *Annals of Mathematical Statistics*, 36:1351–1374.

Brillinger, D. R. (1972). The spectra analysis of stationary interval functions. *Proceedings of 6th Berkeley Symposium: Mathematics, Statistics, Probability*, 1:483–513.

Brillinger, D. R. (1975a). Estimation of product densities. *Proceedings of Computer Science and Statistics 8th Annual Symposium on the Interface*, pages 431–438.

Brillinger, D. R. (1975b). Estimation of product densities. *Proceedings of Computer Science and Statistics 8th Annual Symposium on the Interface*, pages 431–438.

Brillinger, D. R. (1975c). Identification of point process systems. *Annals of probability*, 3:909–929.

Brillinger, D. R. (1976). Identification of second-order product densities. *Journal of royal statistical society B*, 38:60–66.

Brillinger, D. R. (1978). Comparative analysis of the study of ordinary time series and of point process. *Developments in statistics*, 1:33–133.

Brillinger, D. R. (1981). *Time series: data analysis and theory*. Siam.

Brillinger, D. R., Bryant, H. L. J., and Segundo, J. P. (1976). Identification of synaptic interactions. *Biological cybernetics*, 22:213–228.

Burkitt, A. N. (2006). A review of the integrate-and-fire neuron model: I. homogeneous synaptic input. *Biological cybernetics*, 95(1):1–19.

Buzsáki, G., Anastassiou, C. A., and Koch, C. (2012). The origin of extracellular fields and currentseeg, ecog, lfp and spikes. *Nature reviews neuroscience*, 13(6):407.

Carracedo, L. M., Kjeldsen, H., Cunnington, L., Jenkins, A., Schofield, I., Cunningham, M. O., Davies, C. H., Traub, R. D., and Whittington, M. A. (2013). A neocortical delta rhythm facilitates reciprocal interlaminar interactions via nested theta rhythms. *The Journal of Neuroscience*, 33(26):10750–10761.

Carter, G. C. (1987). Coherence and time delay estimation. *Proceedings of the IEEE*, 75(2):236–255.

Carter, G. C., Knapp, C. H., and Nuttall, A. H. (1973). Estimation of the magnitude-squared coherence function via overlapped fast fourier transform processing. *Audio and Electroacoustics, IEEE Transactions on*, 21(4):337–344.

Cellucci, C. J., Albano, A. M., and Rapp, P. E. (2005). Statistical validation of mutual information calculations: Comparison of alternative numerical algorithms. *Physical Review E*, 71(6):066208.

Charles, A. C., Merrill, J. E., Dirksen, E. R., and Sandersont, M. J. (1991). Intercellular signaling in glial cells: calcium waves and oscillations in response to mechanical stimulation and glutamate. *Neuron*, 6(6):983–992.

Conway, B. A., Halliday, D. M., and Rosenberg, J. R. (1993). Detection of weak synaptic interactions between single ia afferent and motor-unit spike trains in the decerebrate cat. *Journal of Physiology*, 471:379–409.

Cooley, J. W. and Tukey, J. W. (1965). An algorithm for the machine calculation of complex fourier series. *Mathematics of computation*, 19(90):297–301.

Coomber, B., O'Donoghue, M. F., and Mason, R. (2008). Inhibition of endocannabinoid metabolism attenuates enhanced hippocampal neuronal activity induced by kainic acid. *Synapse*, 62(10):746.

Cover, T. M. and Thomas, J. A. (2012). *Elements of information theory*. John Wiley & Sons.

da Silva, F. L., Pijn, J. P., and Boeijinga, P. (1989). Interdependence of eeg signals:

linear vs. nonlinear associations and the significance of time delays and phase shifts. *Brain topography*, 2(1-2):9–18.

Darbellay, G. A., Vajda, I., et al. (1999). Estimation of the information by an adaptive partitioning of the observation space. *IEEE Transactions on Information Theory*, 45(4):1315–1321.

Dayan, P. and Abbott, L. F. (2001). *Theoretical neuroscience*, volume 806. Cambridge, MA: MIT Press.

Eckhorn, R. and Pöpel, B. (1974). Rigorous and extended application of information theory to the afferent visual system of the cat. i. basic concepts. *Kybernetik*, 16(4):191–200.

El-Gaby, M., Shipton, O. A., and Paulsen, O. (2015). Synaptic plasticity and memory: new insights from hippocampal left–right asymmetries. *The Neuroscientist*, 21(5):490–502.

Fraser, A. M. and Swinney, H. L. (1986). Independent coordinates for strange attractors from mutual information. *Physical review A*, 33(2):1134.

Freiwald, W. A., Valdes, P., Bosch, J., Biscay, R., Jimenez, J. C., Rodriguez, L. M., Rodriguez, V., Kreiter, A. K., and Singer, W. (1999). Testing non-linearity and directedness of interactions between neural groups in the macaque inferotemporal cortex. *Journal of neuroscience methods*, 94(1):105–119.

Freund, T. F. and Buzsáki, G. (1996). Interneurons of the hippocampus. *Hippocampus*, 6(4):347–470.

Gamerman, D. and Lopes, H. F. (2006). *Markov chain Monte Carlo: stochastic simulation for Bayesian inference*. CRC Press.

Gazzaniga, M. S. (2000). *Cognitive neuroscience: A reader.* Blackwell Publishing.

Gazzaniga, M. S. (2004). *The cognitive neurosciences*. MIT press.

Gentner, D., Holyoak, K. J., Holyoak, K. J., and Kokinov, B. N. (2001). *The analogical mind: Perspectives from cognitive science*. MIT press.

Gerstein, G. L. and Perkel, D. H. (1972). Mutual temporal relationships among neuronal spike trains: statistical techniques for display and analysis. *Biophysical Journal*, 12(5):453 – 473.

Gerstner, W. and Kistler, W. M. (2002). *Spiking neuron models: Single neurons, populations, plasticity*. Cambridge university press.

Gevins, A. and Schaffer, R. (1979). A critical review of electroencephalographic (eeg) correlates of higher cortical functions. *Critical reviews in bioengineering*, 4(2):113–164.

Geweke, J. (1982). Measurement of linear dependence and feedback between multiple time series. *Journal of the American statistical association*, 77(378):304–313.

Gouaux, E. and MacKinnon, R. (2005). Principles of selective ion transport in channels and pumps. *science*, 310(5753):1461–1465.

Granger, C. W. (1969). Investigating causal relations by econometric models and cross-spectral methods. *Econometrica: Journal of the Econometric Society*, pages 424–438.

Grassberger, P. (1988). Finite sample corrections to entropy and dimension estimates. *Physics Letters A*, 128(6):369–373.

Greicius, M. D., Krasnow, B., Reiss, A. L., and Menon, V. (2003). Functional connectivity in the resting brain: a network analysis of the default mode hypothesis. *Proceedings of the National Academy of Sciences*, 100(1):253–258.

Guha, A. (2006). Analysis of dependence structures of hybrid stochastic processes using mutual information.

Halliday, D., Rosenberg, J., Amjad, A., Breeze, P., Conway, B., and Farmer, S. (1995). A framework for the analysis of mixed time series/point process datatheory and application to the study of physiological tremor, single motor unit discharges and electromyograms. *Progress in biophysics and molecular biology*, 64(2):237–278.

Halliday, D. M. (2005). Spike-train analysis for neural systems. pages 555–580.

Hille, B. et al. (2001). *Ion channels of excitable membranes*, volume 507. Sinauer Sunderland, MA.

Hlaváčková-Schindler, K., Paluš, M., Vejmelka, M., and Bhattacharya, J. (2007). Causality detection based on information-theoretic approaches in time series analysis. *Physics Reports*, 441(1):1–46.

Hodgkin, A. and Huxley, A. (1952a). The components of membrane conductance in the giant axon of loligo. *The Journal of physiology*, 116(4):473–496.

Hodgkin, A. L. and Huxley, A. F. (1952b). A quantitative description of membrane current and its application to conduction and excitation in nerve. *The Journal of physiology*, 117(4):500–544.

Izhikevich, E. M. (2007). *Dynamical systems in neuroscience*. MIT press.

Izhikevich, E. M. and Edelman, G. M. (2008). Large-scale model of mammalian thalamocortical systems. *Proceedings of the national academy of sciences*, 105(9):3593–3598.

Izhikevich, E. M. et al. (2003). Simple model of spiking neurons. *IEEE Transactions on neural networks*, 14(6):1569–1572.

Kamboh, A. M. and Mason, A. J. (2013). Computationally efficient neural feature extraction for spike sorting in implantable high-density recording systems. *IEEE transactions on neural systems and rehabilitation engineering*, 21(1):1–9.

Kandel, E. R., Schwartz, J. H., and Jessel, T. M. (1995). *Essentials of neural science and behavior*. Prentice-Hall.

Kandel, E. R., Schwartz, J. H., Jessell, T. M., et al. (2000). *Principles of neural science*, volume 4. McGraw-Hill New York.

Karkare, V., Gibson, S., and Marković, D. (2013). A 75-μw, 16-channel neural spike-sorting processor with unsupervised clustering. *IEEE Journal of Solid-State Circuits*, 48(9):2230–2238.

Kennel, M. B., Shlens, J., Abarbanel, H. D., and Chichilnisky, E. (2005). Estimating entropy rates with bayesian confidence intervals. *Neural Computation*, 17(7):1531–1576.

Kraskov, A., Stögbauer, H., and Grassberger, P. (2004). Estimating mutual information. *Physical review E*, 69(6):066138.

London, M., Schreibman, A., Häusser, M., Larkum, M. E., and Segev, I. (2002). The information efficacy of a synapse. *Nature neuroscience*, 5(4):332–340.

Melssen, W. J. and Epping, W. J. M. (1987). Detection and estimation of neural connectivity based on cross-correlation analysis. *Biological cybernetics*, 57:403–414.

Mendel, J. M. (1991). Tutorial on higher-order statistics (spectra) in signal processing and system theory: theoretical results and some applications. *Proceedings of the IEEE*, 79(3):278–305.

Metcalfe, A. V. and Cowpertwait, P. S. (2009). *Introductory time series with R*.

Moon, Y.-I., Rajagopalan, B., and Lall, U. (1995a). Estimation of mutual information using kernel density estimators. *Physical Review E*, 52(3):2318–2321.

Moon, Y.-I., Rajagopalan, B., and Lall, U. (1995b). Estimation of mutual information using kernel density estimators. *Physical Review E*, 52(3):2318.

Moser, M.-B. and Moser, E. I. (1998). Functional differentiation in the hippocampus. *Hippocampus*, 8(6):608–619.

Neter, J., Kutner, M. H., Nachtsheim, C. J., and Wasserman, W. (1996). *Applied linear statistical models*, volume 4. Irwin Chicago.

Nicholls, J. G., Martin, A. R., Wallace, B. G., and Fuchs, P. A. (2001). *From neuron to brain*, volume 271. Sinauer Associates Sunderland, MA.

Nikias, C. L. and Raghuveer, M. R. (1987). Bispectrum estimation: A digital signal processing framework. *Proceedings of the IEEE*, 75(7):869–891.

Obeid, I., Morizio, J. C., Moxon, K. A., Nicolelis, M. A., and Wolf, P. D. (2003). Two multichannel integrated circuits for neural recording and signal processing. *IEEE transactions on biomedical engineering*, 50(2):255–258.

O'keefe, J. and Nadel, L. (1978). *The hippocampus as a cognitive map*. Oxford: Clarendon Press.

Panzeri, S., Schultz, S. R., Treves, A., and Rolls, E. T. (1999). Correlations and the encoding of information in the nervous system. *Proceedings of the Royal Society of London B: Biological Sciences*, 266(1423):1001–1012.

Parpura, V., Heneka, M. T., Montana, V., Oliet, S. H., Schousboe, A., Haydon, P. G., Stout, R. F., Spray, D. C., Reichenbach, A., Pannicke, T., et al. (2012). Glial cells in (patho) physiology. *Journal of neurochemistry*, 121(1):4–27.

Pereda, E., Quiroga, R. Q., and Bhattacharya, J. (2005). Nonlinear multivariate analysis of neurophysiological signals. *Progress in neurobiology*, 77(1):1–37.

Perkel, D. H., Gerstein, G., and Moore, G. P. (1967). Neuronal spike trains and stochastic point processes: Ii. simultaneous spike trains. *Biophysical journal*, 7(4):419 – 440.

Pijn, J., Vijn, P., Da Silva, F. L., Boas, W. V. E., and Blanes, W. (1990). Localization of epileptogenic foci using a new signal analytical approach. *Neurophysiologie Clinique/Clinical Neurophysiology*, 20(1):1–11.

Press, W. H., Flannery, B. P., Teukolsky, S. A., Vetterling, W. T., et al. (1989). *Numerical recipes*, volume 2. Cambridge university press Cambridge.

Priestley, M. B. (1981). *Spectral analysis and time series*. Academic press.

Quiroga, R. Q., Kraskov, A., Kreuz, T., and Grassberger, P. (2002). Performance of different synchronization measures in real data: a case study on electroencephalographic signals. *Physical Review E*, 65(4):041903.

Quiroga, R. Q., Nadasdy, Z., and Ben-Shaul, Y. (2004). Unsupervised spike detection and sorting with wavelets and superparamagnetic clustering. *Neural computation*, 16(8):1661–1687.

Reeke, G. N., Poznanski, R. R., Lindsay, K. A., Rosenberg, J. R., and Sporns, O. (2005). *Modeling in the neurosciences: from biological systems to neuromimetic robotics*. CRC Press.

Reinagel, P. and Reid, R. C. (2000). Temporal coding of visual information in the thalamus. *The Journal of Neuroscience*, 20(14):5392–5400.

Rey, H. G., Pedreira, C., and Quiroga, R. Q. (2015). Past, present and future of spike sorting techniques. *Brain research bulletin*, 119:106–117.

Rigas, A. (1983). Point processes and time series analysis: Theory and applications to complex physiological system. *Proceedings of Computer Science and Statistics 8th Annual Symposium on the Interface*, pages 431–438.

Rosenberg, J. R., Amjad, A. M., Breeze, P., Brillinger, D. R., and Halliday, D. M. (1989). The fourier approach to the identification of synaptic coupling between neuronal spike trains. *Progress in Biophysics and Modecular Biology*, 53:1–31.

Rosenberg, J. R., Murray-Smith, D. J., and Rigas, A. (1982). An introduction to the application of system identification techniques to elements of neuromuscular system. *Transactions of the Institute of Measurement and Control*, 4(4):187–201.

Rubinov, M. and Sporns, O. (2010). Complex network measures of brain connectivity: uses and interpretations. *Neuroimage*, 52(3):1059–1069.

Sameshima, K. and Baccalá, L. A. (1999). Using partial directed coherence to describe neuronal ensemble interactions. *Journal of neuroscience methods*, 94(1):93–103.

Schraudolph, N. N. (2004). Gradient-based manipulation of nonparametric entropy estimates. *Neural Networks, IEEE Transactions on*, 15(4):828–837.

Schreiber, T. (2000). Measuring information transfer. *Physical review letters*, 85(2):461.

Searsl, T. A. and Stagg, D. (1976). Short-term synchronization of intercostal motoneurone acitivity. *Journal of Physiologyl*, 263(3):357 – 381.

Senik, M., ODonoghue, M., and Mason, R. (2013). Intra-and interhippocampal connectivity in a ka-induced mtle rat model. In *Program No. 143.05. 2013 Neuroscience Meeting Plan*.

Shannon, C. E. and Weaver, W. (1949). The mathematical theory of information.

Shepard, G. M. (1988). *Neurobiology*. Oxford University Press.

Shlens, J., Kennel, M. B., Abarbanel, H. D., and Chichilnisky, E. (2007). Estimating information rates with confidence intervals in neural spike trains. *Neural Computation*, 19(7):1683–1719.

Shumway, R. H. and Stoffer, D. S. (2011). Time series regression and exploratory data analysis. In *Time series analysis and its applications*, pages 47–82. Springer.

Silverman, B. W. (1986). *Density estimation for statistics and data analysis*, volume 26. CRC press.

Steuer, R., Kurths, J., Daub, C. O., Weise, J., and Selbig, J. (2002). The mutual information: detecting and evaluating dependencies between variables. *Bioinformatics*, 18(suppl 2):S231–S240.

Strong, S. P., Koberle, R., van Steveninck, R. R. d. R., and Bialek, W. (1998). Entropy and information in neural spike trains. *Physical review letters*, 80(1):197–200.

Suárez, R., Gobius, I., and Richards, L. J. (2014). Evolution and development of interhemispheric connections in the vertebrate forebrain. *Frontiers in human neuroscience*, 8:497.

Sun, F. T., Miller, L. M., and D'esposito, M. (2004). Measuring interregional functional connectivity using coherence and partial coherence analyses of fmri data. *Neuroimage*, 21(2):647–658.

Taxidis, J., Coomber, B., Mason, R., and Owen, M. (2010). Assessing cortico-hippocampal functional connectivity under anesthesia and kainic acid using generalized partial directed coherence. *Biological cybernetics*, 102(4):327–340.

Trappenberg, T. (2010). *Fundamentals of computational neuroscience*. OUP Oxford.

Troyer, T. W. and Miller, K. D. (1997). Physiological gain leads to high isi variability in a simple model of a cortical regular spiking cell. *Neural Computation*, 9(5):971–983.

Walters-Williams, J. and Li, Y. (2009). Estimation of mutual information: A survey. In *International Conference on Rough Sets and Knowledge Technology*, pages 389–396. Springer.

Wasserman, L. (2013). *All of statistics: a concise course in statistical inference*. Springer Science & Business Media.

Wolpert, D. H. and Wolf, D. R. (1995). Estimating functions of probability distributions from a finite set of samples. *Physical Review E*, 52(6):6841–6854.

Womelsdorf, T., Schoffelen, J.-M., Oostenveld, R., Singer, W., Desimone, R., Engel, A. K., and Fries, P. (2007). Modulation of neuronal interactions through neuronal synchronization. *science*, 316(5831):1609–1612.

Woolrich, M. W., Ripley, B. D., Brady, M., and Smith, S. M. (2001). Temporal autocorrelation in univariate linear modeling of fmri data. *Neuroimage*, 14(6):1370–1386.

Yang, Y. and Halliday, D. M. (2018). A unified framework of third order time and frequency domain analysis for neural spike trains. In *2018 IEEE Statistical Signal Processing Workshop (SSP)*, pages 707–711. IEEE.